Dynamical aspects of the regulation of bacterial proliferation

Letícia Galera Laporta

TESI DOCTORAL UPF / ANY 2018

DIRECTOR DE LA TESI
Jordi Garcia Ojalvo

Departament de Ciències Experimentals i de La Salut

Universitat Pompeu Fabra
Barcelona

‘I am among those who think that science has great beauty. A scientist in his laboratory is not only a technician: he is also a child placed before natural phenomena which impress him like a fairy tale.’

M. Skłodowska-Curie

Al (meu) Jordi

Acknowledgements

This Thesis represents the sum of the effort of many people that, at different levels, have helped me to get here. Now, I would like to use this opportunity to thank all of them.

Primer, m'agradaria començar pel meu tutor, el Prof. Jordi Garcia Ojalvo. Et vull donar les gràcies de tot cor per haver-me donat l'oportunitat de formar part del teu grup, per tota la paciència, alegria i energia que desprens i encomanes. Per fer-me veure el valor dels experiments i tot el que poden amagar. Amb tu he après una nova manera de fer i entendre la ciència. Per tot, moltes gràcies :)

Gràcies a tots els companys i companyes del laboratori, als que hi són i als que hi han passat. Especialment als companys dels últims anys de doctorat: el Carlos, el Pablo, la Rosa i el Marçal. Aquí també incloc a la Júlia. Gràcies a tots pel bon ambient que heu creat, per estar sempre disposats a donar un cop de mà i per tots els moments compartits. Em sento molt afortunada d'haver estat companya vostra i m'emporto un munt de bons records de tots vosaltres. També li voldria donar les gràcies a la Belén, per haver confiat en mi, ja que va ser ella qui em va presentar el grup del Jordi. I la Lorena, a la que li vull donar unes gràcies especials. Desde los primeros experimentos en el laboratorio tu has estado allí (la primera vez que tuve una imagen de microscopía de fluorescencia fue junto a ti. Brilla!). Todas las horas que nos hemos pasado hablando de protocolos y de la vida en general, todas y cada una de ellas forman parte de esta Tesis. Por eso, muchas gracias!

Gràcies als professionals que treballen en el PRBB i en la UPF per crear al voltant de la ciència un ambient tant motivador. Especialment a les noies de la "cuina" per sempre estar disposades a fer favors, al grup d'Intervals que sempre han proposat cursos interessant i que m'han servit de guia en molts moments de la Tesi. També a la gent que organitza les Jornades de portes obertes, on amb orgull hem pogut compartir un petit tros de la nostra feina.

I would also like to thank to Prof. Gürol Süel. Every time that I've been in your lab I felt that I was part of the group. In all the stays I've charged my batteries, and I've enjoyed the adventure of doing science, because as the Master said, "Do... or do not. There is no try." And in your lab, I found great people and I would like to thank them for making me feel at home: Joe, Arthur, San, Maja, Jintao, and Kaito. And of course, my friend Daisy. You have shared with me your knowledge and your hard work, and you have made me progress in my work. And, of course, thank you also for your friendship!

També m'agradaria donar-li les gràcies a la Laura, el Jofre i el Biel, els meus amics de tota la vida. Nois, què dir-vos? Moltes gràcies per sempre transmetre'm la vostra energia i confiança. Aquesta Tesi també porta un trosset vostre.

Finalment, agrair-li a la meva mare per ensenyar-me el valor de les petites coses i sempre recolzar-me en les meves decisions. I al meu pare perquè va ser amb ell amb qui jugant a fer experiments vaig descobrir la meva vocació. Gràcies als dos per tot el que meu ensenyat, i tot el que em queda per aprendre.

Aquesta Tesi representa tot un procés de creixement personal i professional que des del principi dels principis he viscut al costat del Jordi. Per això, et vull dedicar la meva Tesi. Moltes gràcies per tot.

Abstract

Bacterial proliferation has been studied for more than 100 years, but our knowledge of the mechanisms that control its dynamical aspects is still very limited. In this Thesis we have studied, at both single-cell and population levels, different aspects of the main regulators of bacterial proliferation, namely the cell cycle, biomass production and membrane stability. Our goal has been to shed light on how perturbation of these regulators affects their dynamical responses in a variety of situations. Specifically, we show that the periodic doubling of genes through the bacterial cell cycle partially entrains a genetic oscillator, but that significant coupling only arises when the oscillator is fed back to cell cycle. We have also studied perturbations in the ability of cells to produce biomass, for instance through antibiotics that affect ribosomal function. Our results suggest that survival in the presence of these antibiotics is determined by the ability of the cells to incorporate magnesium ions, which can be captured by membrane potential changes. Finally, we show that interplay between different bacterial species with diverse sensitivities to membrane-targeting antibiotics can have an unexpected outcome in co-culture, which can be explained in a simple manner by the sharing of the antibiotic between the two species.

Resum

La proliferació bacteriana ha estat estudiada durant més de 100 anys, però el nostre coneixement dels mecanismes que controlen els aspectes dinàmics d'aquesta encara són molt limitats. En aquesta Tesi hem estudiat, tant en cèl·lules individuals com a nivell poblacional, diferents aspectes dels principals reguladors de la proliferació cel·lular, concretament el cicle cel·lular, la producció de biomassa i la estabilitat de la membrana. El nostre objectiu ha estat ajudar a explicar com pertorbacions en aquests reguladors afecten la dinàmica de les seves respostes en una varietat de situacions. Específicament, mostrem que el doblament periòdic de gens a través del cicle cel·lular bacterià entrena parcialment un oscil·lador genètic, però aquest acoblament només és significatiu quan l'oscil·lador retorna la resposta al cicle cel·lular. També hem estudiat pertorbacions en l'habilitat de les cèl·lules de produir biomassa, per exemple a través d'antibiòtics que afecten la funció ribosomal. Els nostres resultats suggereixen que la supervivència sota l'efecte d'aquests antibiòtics ve determinada per l'habilitat de les cèl·lules d'incorporar ions de magnesi, la qual pot ser capturada a través de canvis en el potencial de membrana. Finalment, mostrem que les interaccions entre diferents espècies bacterianes amb diverses sensitivitats a antibiòtics que afecten la membrana cel·lular poden donar lloc a resultats inesperats quan es troben en co-cultiu, els quals poden ser explicats de forma senzilla a partir del compartiment de l'antibiòtic entre les dues espècies.

Preface

Bacteria represent one of the major components of Earth's biomass, and can be found in all kind of ecological niches, from oceans to the soil, including within all kind of organisms. In all their different ecosystems, bacteria play important roles, such as decomposition of nutrients and nitrogen fixation, among others. Bacteria help, for example, the digestive system to break down and assimilate nutrients, providing the host organism with different essential vitamins, such as cobalamin (vitamin B-12) and vitamin K. Despite all the benefits that bacteria have, an uncontrolled growth of these microorganisms is a threat for public health and industry. Some bacterial species can produce infections difficult to control with antibiotic treatments, due to the appearance of new antibiotic-resistant strains. Concerning industry, contaminations during fermentation processes and production, for example of vitamins and enzymes, have high costs, and the design of new strategies to control contaminations is needed.

Since the past century, when scientists as J. Monod and A. Hersey started to establish knowledge about bacterial growth, the understanding of bacterial physiology and the regulation of bacterial proliferation has hugely progressed. Nevertheless, there are still some essential aspects missing at the molecular level, such as for example in relation to the bacterial response to antibiotics. One possible reason for this lack of information is that the large majority of studies have been performed so far at the population level, while our knowledge of the dynamical aspects of bacterial proliferation at the single-cell level is still scarce. New data from single cells, in combination with mathematical models, provide an opportunity to build further understanding of how bacterial proliferation is regulated. This Thesis is devoted to the study of a variety of dynamical aspects of the regulation of bacterial proliferation. Specifically, we have studied different facets of how bacterial proliferation is regulated at both the single-cell and population levels, for two of the best known bacterial species, namely *Escherichia coli*, and *Bacillus subtilis.*

The Thesis is organized as follows. In Part I we give a general introduction of the basic aspects of the bacterial regulation, followed by an explanation of the methods that we have used in the different studies presented in this Thesis. In particular, in Chapter 1 we focus on the characteristics of the processes involved in cell cycle, biomass production and structural stability, as the main regulators for bacterial growth. Next, we present an overview of the dynamical aspects of bacterial stress. In Chapter 2 we introduce the different experimental methods, data acquisition techniques, and quantitative analysis. This introduction aims to provide the bases for the understanding of the biological aspects discussed in the Thesis, and the techniques that we use to obtain the following results.

In Part II we present three Chapters which include the results obtained in this Thesis. Each of the studies is linked to at least one of the fundamental pillars of cell proliferation mentioned above, with a focus on the dynamics of these processes as the overarching element. Specifically, in Chapter 3 we ask whether oscillatory processes that exist within a cell can affect the cell cycle rhythm. Next, in Chapter 4 we study the effect of ribosomal stress upon the modulation of ionic content in bacteria, which can be captured by membrane potential dynamics. This Chapter is the result of a teamwork with the laboratory of Prof. Gürol Süel at University of California San Diego. The last study is presented in Chapter 5, where we investigate the response in time of a minimal ecosystem of two species to one of the most used antibiotic families, beta-lactam antibiotics, which affect bacterial membrane stability.

Finally, in Part III of this Thesis we summarize the most relevant results, with their corresponding conclusions. We also comment on the limitations of each of the studies and propose future perspectives inspired by the different outcomes.

Our work aims to illustrate the importance of the study of bacterial proliferation dynamics, which can reveal new mechanisms that explain the bacterial behavior, such as the increase in their tolerance to antibiotic treatments.

Contents

List of Figures

Chapter 1: Regulation of cellular proliferation 5

Chapter 2: Methods 27

List of Tables

Part I

Introduction

"The most common circumstance in which repeated doublings, and therefore exponential growth, occurs is in biological reproduction. Consider first the simple case of a bacterium that reproduces by dividing itself in two. After a while, each of the two daughter bacteria divides as well. As long as there's enough food and no poisons in the environment, the bacterial colony will grow exponentially. Under very favorable circumstances, there can be a doubling every 15 minutes or so. That means 4 doublings an hour and 96 doublings a day. Although a bacterium weighs only about a trillionth of a gram, its descendants, after a day of wild asexual abandon, will collectively weigh as much as a mountain; in a little over a day and a half as much as the Earth; in two days more than the Sun... And before very long, everything in the Universe will be made of bacteria. This is not a very happy prospect, and fortunately it never happens. Why not? Because exponential growth of this sort always bumps into some natural obstacle."

C. Sagan, 1997

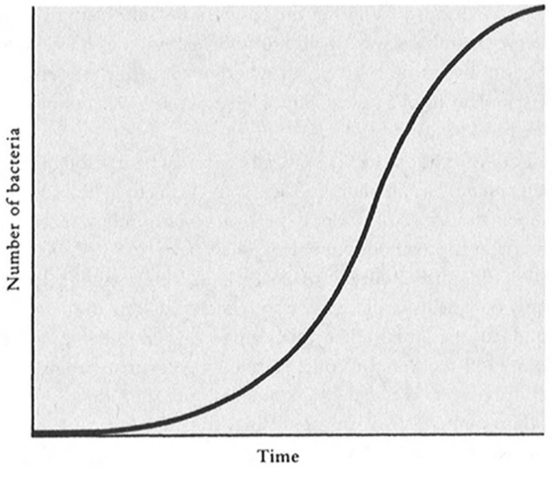

Chapter 1

Regulation of cellular proliferation

1.1 Bacterial proliferation

Bacterial proliferation is considered as the growth of a population, produced by the increase of the total number of individuals. In general, bacteria reproduce by binary fission and, under optimal conditions, the doubling time for the most common species used in lab studies is about one to three hours. Some species can duplicate even faster, with doubling times as shorter as 15 minutes. In any case, bacteria generally, live in varying environments, and they need to continually adapt their growth to the current conditions. Thus, bacterial growth, and consequently bacterial proliferation, is a dynamical process.

The bacterial growth dynamics can be quantified by spectrophotometry, which measures the light absorbance of a liquid culture at a wave length of 600 nm, known as optical density (OD). This OD is directly proportional to the bacterial cell density, for low concentration of cells. At the beginning of the past century, Lane-claypon described for the first time the four phases of the growth of a bacterial population, defined as the *bacterial growth curve*. Later, in 1928, Buchanan described a much more detailed growth curve, differentiating the transition between the different phases. Fig. 1.1 illustrates the standard population growth of an inoculum of bacteria in liquid culture with the distinct four phases introduced by Lane-Claypon. The first part of the curve is the *lag phase*, which corresponds to the period of time where there is no observable growth of the population. During this first phase, cells are metabolically active and can even increase in size, but there are no new rounds of DNA replication (Madar et al., 2013). Cells use this time to adapt their metabolism to the new conditions. For this reason, the timing of this phase depends on the previous and current conditions (Jõers and Tenson, 2016). For example, if we inoculate cells from a rich medium to a minimal medium the lag phase will be longer than if they are kept in the same kind of medium. Once cells are adapted, DNA replication starts and cells begin to grow and divide until they reach the maximum growth rate (maximum slope of the curve). This period is known as the *exponential phase* in which cells proliferate, as the name indicates, in a exponential fashion. During exponential growth, cells rapidly consume nutrients and accumulate toxic metabolites and inhibitory signals in the medium. Other environmental factors, such as pH and temperature, also change and generate a less favorable environment. At that point, the population starts to slow down its growth and enters into the *stationary phase*. Even when new duplications can be observed, these are compensated by the dying cells, keeping the population size constant. The bacterial population can remain in this phase for several hours, even days, and during this period of time, several strategies to cope with stress emerge, such as sporulation, biofilm formation, or antibiotic production. Eventually, cellular death exceeds the doublings due to the extreme conditions, leading to a decrease in the growth curve, which corresponds to the *death or decline phase*.

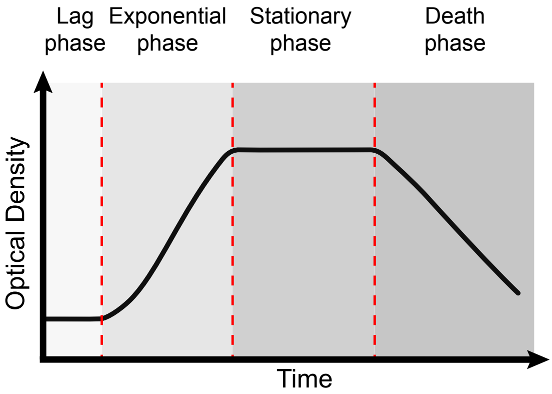

Figure 1.1: Standard bacterial growth curve. Scheme of a typical bacterial growth curve, where the optical density of a culture, proportional to the cell density, is represented as a function of time. Four phases are represented: lag, exponential, stationary, and death phase. The duration of each phase depends on the bacterial species and the growth conditions.

A complex regulatory network that depends on internal and external factors controls the doubling time for each type of bacterium, but the specific mechanisms can vary between different species, producing a different ecological adaptation to very diverse niches. In general, cells coordinate multiple cellular processes, such as DNA replication, chromosome segregation, and cell division, together with biomass production and energy balance. Moreover, they need to maintain a correct size and structure through modulation of the cell membrane. In the following sections, we present a general description of the fundamental cellular processes that control cell proliferation. We divide these processes into three categories: the cell cycle, biomass production and the maintenance of the cellular structure.

1.2 Bacterial cell cycle

The bacterial cell cycle has as objective the generation of a new cell. With this purpose, bacteria have to copy their DNA, segregate them into the new cells, and divide, in consecutive order. The cell cycle in bacteria can be divided into three periods: from cell division to the initiation of chromosome replication (B period), the chromosome replication period itself (C period), and from the termination of replication to the end of cell division (D period) (Fig. 1.2)(see review (Wang and Levin, 2009)).

The initiation of chromosome replication begins in the *oriC* region. Here, the replication machinery assembles (B period), and starts the duplication of the DNA bidirectionally through the circular chromosome. The replication machinery progresses until it reaches the *terC* region, where the finalization of the DNA duplication occurs (C period). At the end of the replication, the cell segregates each copy of the chromosome to separated poles, to ensure an equal distribution of the DNA copies in the two new cells. Finally, in the middle of the cell, the tubuline-like protein FtsZ forms a ring, *the Z-ring*, that serves as a scaffold for the recruitment of the cell division machinery. The cell cycle ends after septation, when one bacterium gives rise to two cells (D period), which undergo a new cell cycle (Xiao and Goley, 2016).

The different steps of the bacterial cell cycle are, in general, common to all prokaryotic and eukaryotic organisms. The eukaryotic cell cycle consists of four characteristic phases: gap 1 (G1), synthesis (S), gap 2 (G2), and mitosis (M). The DNA replication occurs in the *synthesis phase*, and the cell divides in the *mitosis phase*. A series of checkpoints performed by a group of specific genes and proteins (e.g., cyclins) control the transition through the different phases G1 and G2 (Elledge, 1996). While these

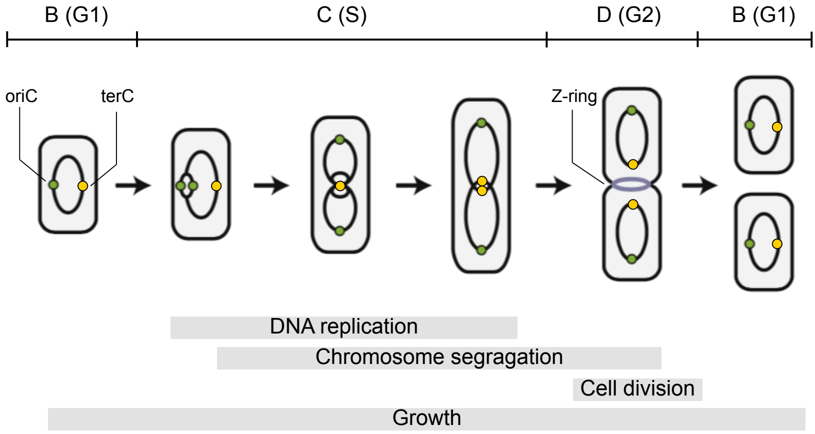

Figure 1.2: Scheme of the bacterial cell cycle phases. The circular bacterial chromosome presents two essential regions: *oriC* and *terC*, where DNA initiation and termination occurs, respectively. The first phase of the cell cycle, known as B period (analog to G1 phase, from the eukaryotic cell cycle), consists in the initiation of chromosome replication. Once the replication has started, it proceeds during the C period (S). The replication ends in the *terC* region, followed by cell division, during the D period (G2). Figure adapted from Heinrich et al. (2015).

checkpoints are not present in the bacterial cell cycle, the three phases of bacteria, B, C, and D, are analogous to the corresponding G1, S, and G2 from the eukaryotic cycle. Additionally, the bacterial stationary phase could be compared to the quiescent phase that can be reached from G1, known as G0, that most eukaryotic differentiate cells experiment (e.g., neurons).

In all organisms, the phases of the cell cycle are tightly regulated, and under constant conditions, this cycle has a constant period (Francis and Barlow, 1988). As we mentioned above, during the G1 and G2 phases of the eukaryotic cycle, cells undergo a series of controlled events, and the deregulation of the checkpoints causes dramatic consequences, such as genomic instability that can lead to development defects, and even cancer (Fisher, 2012). Due to this tight control, there is no overlap between the different phases of the eukaryotic cell cycle. Moreover, this regulatory mechanism ensures that just one round of replication occurs during each cell (Blow and Gillespie, 2008). This is an outstanding difference with the bacterial cell cycle, which can overlap replication rounds to increase the speed under favorable conditions. The period for each phase of the bacterial cell cycle is roughly constant, so it is independent of the growth rate. For example, the duration of the whole cell cycle for *Escherichia coli* is around 60 minutes (Cooper and Helmstetter, 1968). However, the doubling time can be modulated through external factors such as temperature and nutrients, which can lead to durations as fast as 15-20 minutes. In 1968, Cooper and Helmstetter solved this paradox by demonstrating that bacteria in rich conditions initiate multiple rounds of replication during one cell cycle, forming the named *multifork replication* (Fig. 1.3). With this strategy, bacteria overlap multiple rounds of replication (up to eight simultaneous replications), and each daughter cell receives a complete genome that has already started the process of replication. Thus, the multifork replication reduces the duration of the whole cycle and also explains why in fast-growing cells there is more DNA content. But this strategy is not present in the entire bacterial life: some species, such as *Caulobacter crescentus*, have temporal compartmentalization of the cellular phases, thus avoiding the overlap among them (Marczynski, 1999).

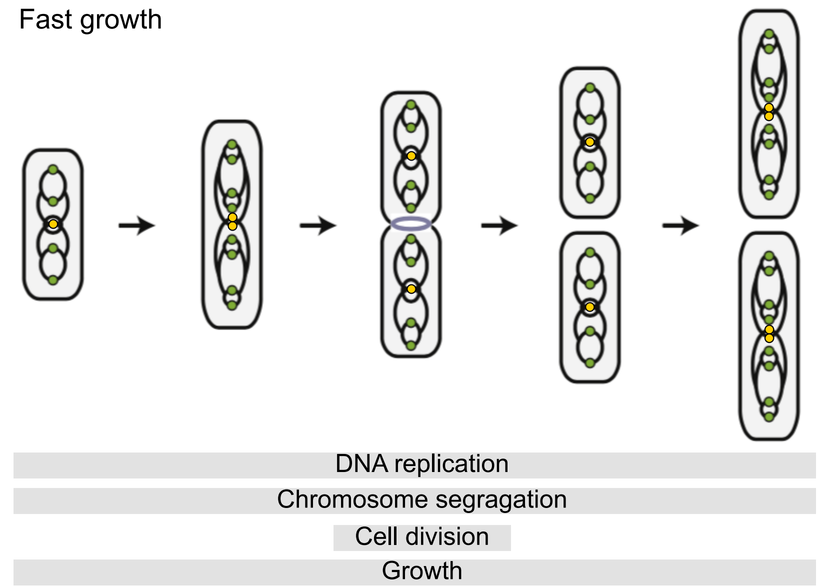

Figure 1.3: Scheme of the fast bacterial cell cycle phases. As in Fig. 1.2, the circular bacterial chromosome contains the *oriC* and the *terC* regions, marked in small green and yellow circles, respectively. Bacteria as *E. coli* and *B. subtilis*, under fast growing conditions, can start new rounds of replication during one cell cycle, forming multiforks of replication. In this situation, each bacterium can contain more than two origins of replication (maximum 16 origins). Figure adapted from Heinrich et al. (2015).

During the cell cycle, cells also need to increase their volume in a coordinated fashion. Donachie, also in 1968, was the first to observe the coupling between the replication and the cell growth. He showed that the ratio between cell mass and the number of origins of replication was constant, implying that cells needed an *initiation mass* to start new rounds of replication. This simple theory was generally accepted and explained why faster cells must be larger (Schaechter et al., 1958). However, recent studies have shown that this theory is not entirely correct since it has been proved that replication can start at different cell mass, breaking the relationship between cell mass and the initiation of replication (Bates and Kleckner, 2005; Wold et al., 1994; Wang and Levin, 2009; Hill et al., 2012). Hence, it seems that the length of the cell does not determine the timing for the DNA replication.

Despite the controversy about the correlation between chromosomal replication and cell length, it is generally accepted that the initiation of the chromosome replication is one of the main factors that control the timing of the cell cycle. The most important molecule responsible for the initiation is the DnaA protein (Løbner-Olesen et al., 1989). Before initiation, there is an accumulation of the active ATP-bound form of this protein, which above a threshold induces the separation of the two DNA strands, facilitating the assembly of the replication machinery. Apart from being a required factor for the replication, this molecule accumulates in a growth-rate-dependent manner, thus providing a link between the cell cycle and cell growth (Skarstad et al., 1986; Løbner-Olesen et al., 1989; Donachie and Blakely, 2003).

1.2.1 Coupling between cyclical processes

Cells, under constant conditions, go through the consecutive phases of the cell cycle with a certain periodicity Tyson and Novák (2008); Wang and Levin (2009). So, they duplicate their DNA content and after division recover the initial amount. This self-sustained periodic behavior makes it possible to consider the cell cycle as a cellular oscillator. From this observation, it is reasonable to think that the cell cycle should transmit its rhythmicity to other cellular processes through the oscillating modulation of the DNA content. Recent works demonstrate that even constitutive protein expression, and processes encoded in genetic circuits, can be affected by the cell cycle (Walker et al., 2016; Veliz-Cuba et al., 2016). Thus, it seems difficult to isolate other cellular processes that can affect cellular proliferation from the cell cycle. In the same way, cell cycle can be also altered by biochemical oscillations such as the circadian rhythm, as we discuss in what follows.

Circadian rhythm

The circadian rhythm, in Latin 'about' (*circa*) 'a day' (*diem*), was observed for the first time by J.J de Marian (1729), in *Mimosa pudica*, a plant that opens and closes its leaves in cycles of 24 hours, independently of the presence of light. However, it was not until 1959 that the chronobiologist Halberg named these periodic oscillations *circadian rhythms*. Almost a decade later, Ronald Konopka and Seymour Benzer established the genetic basis of the circadian activity of the fly *Drosophila melanogaster*, by mutating different parts of a single *locus*, termed as the *period* gene (*per*) (Konopka and Benzer, 1971). Nowadays, circadian rhythms have been found in all kind of organisms, from cyanobacteria to fungi, plants, and animals (Dunlap and Loros, 2017). These rhythms act as timekeepers and allow the organism to anticipate daily environmental changes related to the cycles of light due to the Earth rotation. The prediction of external changes gives the organism the opportunity for a better physiological and behavioral adaptations to the environment.

Surprisingly, the period of this natural oscillator is very robust, being able to maintain its cycle in the absence of any external cue, such as light or temperature. The molecular mechanisms that underlie circadian rhythmicity constitute what is known as the circadian clock, and are based on circuits that contain negative feedback loops at the post-transcriptional level or both transcriptional-translational levels. The cyanobacterium *Synechococcus elongatus* has one of the most studied circadian clocks: the KaiABC system (see review Cohen and Golden (2015) for details). In the 1980s, it was discovered that photosynthesis and nitrogen fixation of this organism were separated in time, depending on the periods of light or dark, respectively (Huang and Chow, 1990; Mitsui et al., 1986). In 1998, the three components of KaiABC were identified as the core clock that undergoes biochemical oscillations with an autonomous period of 24 hours, controlling the expression of genes involved in photosynthesis and nitrogen fixation (Fig. 1.4) (Ishiura, 1998). During the following years, many other circadian clocks have been identified, such as the one based in the CLOCK-BMAL1 complex in mammalian cells. This oscillator is contained in all the cells of the organism, but the central pacemaker that controls the phase resides in a group of neurons located in the hypothalamic suprachiasmatic nucleus (SNC), which receives information of the light-dark cycle through the retina (Saper et al., 2005). The circadian clock in animals can control, for example, changes in body temperature, hormone levels, and blood pressure, and disruption of the system has been associated with pathologies such as hormonal dysfunction, metabolic diseases, insomnia, and cancer, among others (Mohawk et al., 2012).

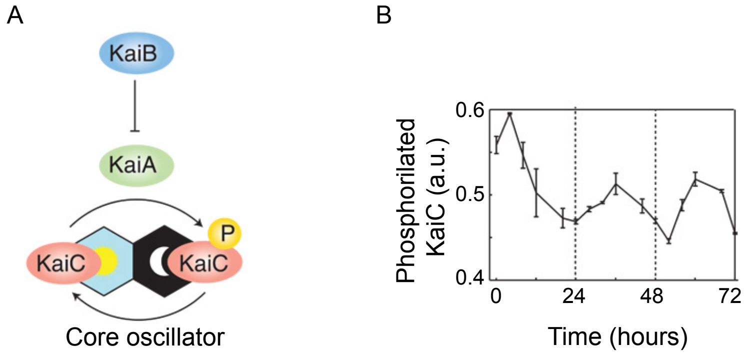

Figure 1.4: The core oscillator KaiABC system sustains biochemical oscillations of 24 hours. A) Scheme model for the phosphorylation changes that KaiC is subjected through the light-dark cycles. During the light period, the KaiA promotes the autophosphorylation of KaiC, and during the dark period KaiB antagonizes the activity of KaiA, by promoting the dephosphorylation of KaiC, through the auto-phosphatase activity that KaiC presents. B) KaiC phosphorylation as a function of time. The coordination of the activity of KaiA and KaiB produces oscillations of 24 hours in the phosphorylated state of KaiC. The KaiABC system is a robust oscillator that can maintain the oscillations *in vitro* (Nakajima, 2005) and can be transplanted to heterologous organisms, for example, *E. coli* (Chen et al., 2015). Figure adapted from (Chen et al., 2015).

At the cellular level, the circadian clock can modulate multiple processes, among them is the cell cycle. Two of the first examples in the literature that showed this relationship were studies performed in the dinoflagellate *Gonyaulax polyedra* and the alga *Euglena gracilis* (Sweeney and Hastings, 1958; Edmunds, 1966). Those studies showed that the circadian clock could gate the cell proliferation to time points. One clear example of the advantage of this synchronization is that the circadian rhythm forces DNA synthesis to avoid periods of light, so as to protect the genetic material from ultraviolet radiation (Burg et al., 1977; Johnson, 2010). Another example is the separation of different cellular processes, such as DNA replication and oxidative metabolic processes, to avoid an increase in the mutation rate due to the oxidative state of the cell (Mellor, 2016).

While many studies have examined the influence of the circadian clock upon the cell cycle, the full extent of that influence has been hard to unravel due to the impossibility of decoupling the two oscillators (at least in the direction in which we are interested, i.e. from the circadian clock to the cell cycle). This has led to the lack of a control situation to use as a baseline. In Chapter 3 we address this issue by using a synthetic oscillator in bacteria, which by design has no a priori effect on the cell cycle, but where such a coupling can be synthetically introduced.

1.3 Biomass production

In unicellular organisms, growth and proliferation are strongly connected, since to generate a new cell it is necessary to grow in volume before cellular division. More than half of the volume (biomass) in bacteria is comprised of proteins. Thus for bacterial growth, protein production plays a central role (Scott et al., 2010).

Ribosomes are the molecules responsible for the translation of the genetic information encoded in mRNA into proteins. In particular, the bacterial ribosome is formed by three ribosomal RNAs and 54 ribosomal proteins, bound in complex structures that are stabilized by cations (Melnikov et al., 2012). These molecular machines present two subunits, the large (50S) subunit, which contains two rRNA species (the 5S and the 23S rRNAs) and the small (30S) subunit, which contains the 16S rRNA. These two subunits together form the whole 70S ribosomal structure. Ribosome biogenesis consumes more than half of the total energy of the cell and uses most of its transcriptional and translational capacity. For this reason, bacteria need to continually control the number of ribosomes and their activity. This regulation allows them to adjust their growth to environmental changes.

In the 1960s, the ‘Copenhagen School,’ formed by M. Schaechter, O. Maaloe, and N. O. Kjeldgaard, among others, from the University of Copenhagen, were the pioneers in the quantification of empirical observations in bacterial physiology. Their main goal was to establish different correlations between various characteristics of the cell. One of the first observations was the connection between the number of ribosomes and the growth rate. They showed that these two cellular components follow a simple rule, known as ‘the linear growth law’ (Fig. 1.5A). In particular, the balance of the number of ribosomal proteins (r-proteins) follows a positive correlation with the growth rate (Schaechter et al., 1958). This property was proposed to be independent of environmental conditions, considering that ribosomes were always acting at their maximal elongation rate. In contrast, later studies showed that the composition of the media could affect the ribosomal activity (Young and Dennis, 1975; Scott et al., 2010). In fact, elongation rate follows a Michaelis-Menten relation with the bacterial growth rate (Fig. 1.5B) (Klumpp et al., 2013), depending on the conditions of the media. Additionally, a recent study from Terry Hwa’s group shows that elongation rate and ribosomal fraction also follows a Michaelis-Menten trend in relation to the growth media conditions (Fig. 1.5C). In that way, the elongation rate decreases as growth slows, in a Michaelis-Menten fashion, that depends on the abundance of ribosomes. However, a minimum elongation rate is maintained even in zero growth (e.g. stationary phase) (Gefen et al., 2014), suggesting a reduction in the fraction of active ribosomes, instead of a simply reduction of the elongation rate as it was previously thought (Dai et al., 2016).

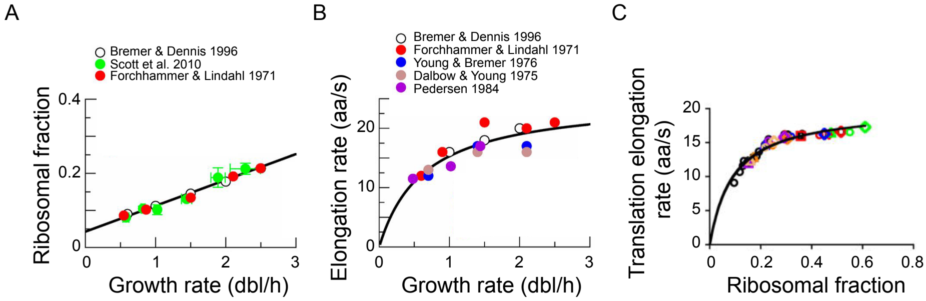

Figure 1.5: Ribosomal content and translational elongation rate determine bacterial growth rate. A) Growth rate (doubling time/hour) dependence of ribosomal content, measured as the fraction of ribosomal protein of the total protein in the cell (μg R-proteins/μg total protein). The results marked with different colors are from three independent studies. B) Growth rate (doubling time/hour) dependence on translational elongation rate of proteins (aa/s). Different colors correspond to data from independent studies. C) Elongation rate (aa/s) plotted as a function of ribosomal content (RNA/protein). Each color represents a different carbon source and each shape a different concentration of the antibiotic chloramphenicol, which targets the ribosomes. The line is a fit that serves as a guide for the eye to see the Michaelis-Menten fashion that this relation follows. Panels A and B adapted from Klumpp et al. (2013), panel C adapted from Dai et al. (2016).

Ribosomal synthesis, degradation and regulation of their activity have different levels of control. At the macroscopic level, there is a partitioning of the resources to produce the different kinds of proteins that the cell needs (Fig. 1.6A) (Klumpp et al., 2013). The set of proteins in a cell is called *proteome*, and in bacteria it contains two different classes of proteins: the growth-rate independent fraction, and the growth-rate dependent fraction. The first one, represented as Q in Fig. 1.6A, is a fixed fraction of proteins which includes the housekeeping genes. On the other side, the growth-rate dependent fraction contains two different modules. One corresponds to metabolism (P), with transporters and catabolic/anabolic enzymes. The other one includes ribosomes and other translation-related proteins (R). The growth-rate dependent fraction has certain plasticity in the proportion of both modules. To illustrate the partitioning with an example, bacteria in exponential phase have fast growth that corresponds to a higher amount of ribosomes, but cells also need to produce importers and enzymes to metabolize the nutrients. A good balance of the production of the different modules is necessary for an adequate level of bacterial proliferation. Several groups have developed mathematical models to describe the allocation of the resources in relation to the availability of nutrients, also considering the correlation between ribosomes and growth rate (Dekel and Alon, 2005; Klumpp et al., 2013; Bosdriesz et al., 2015).

At the microscopic level, the alarmone ppGpp controls directly the production and degradation of ribosomal proteins in relation to the abundance of amino acids (Fig. 1.6B) (Bosdriesz et al., 2015; Corrigan et al., 2016). Thus, this regulatory nucleotide creates a link between ribosomal concentration and the availability of nutrients in the media. Moreover, ppGpp also indirectly controls the partitioning of the proteome by changing the fraction of the ribosomal protein production.

The importance of ribosomal function and its connection with cellular proliferation has led to the development of a broad range of antibiotics that act upon this macromolecule. Chloramphenicol, kanamycin, spectinomycin, and streptomycin are some examples of antibiotics that target different parts of the ribosomes and inhibit different steps of protein production. Besides affecting protein accumulation (which will influence growth), the decrease in protein production also modifies the metabolic rates (Lobritz et al., 2015), generating a global effect on the physiological state of the cell. Some of these aspects will be discussed in more detail in Chapter 4.

In this summary, we have seen that the number and activity of ribosomes constitute a crucial factor in the adaptation of cell proliferation to the external conditions. However, very little is known about the dynamics of ribosomal activity under stress. For this reason, quantitative studies at the single-cell level under these conditions may provide new insights for a better understanding of how ribosomes affect proliferation and other cellular processes. In Chapter 4 we will study how ribosomal stress caused is affected by the regulation of cation content, and will show that the associated stress response, and its associated cell survival, are heterogeneous.

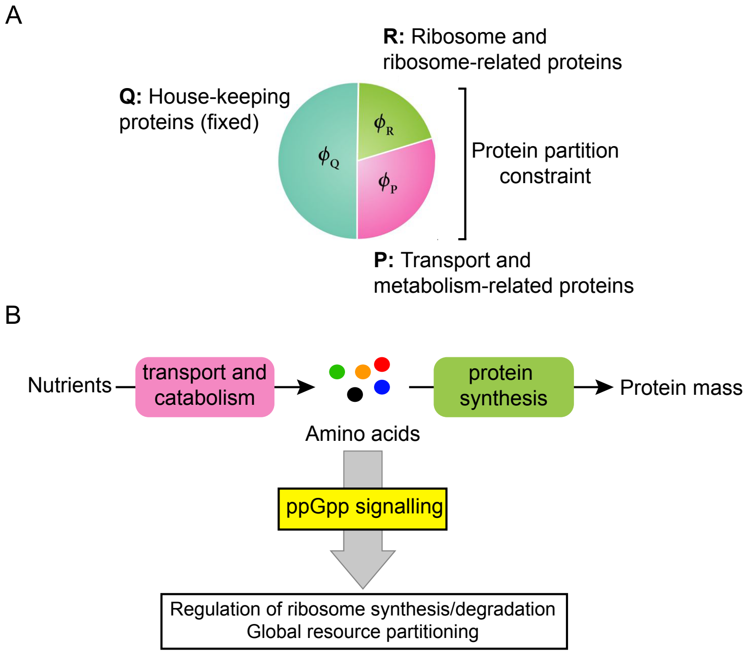

Figure 1.6: Regulation of ribosome production. A) Pie chart representing the partitioning of the proteome, at a coarse-grained level. A fixed section that corresponds to housekeeping proteins (Q), and two variable parts, the ribosome and ribosome-related proteins (R), and the transport and metabolism-related proteins (P). Cells need to find a balance between these two variable fractions in relation to the environment. B) Diagram representing the conversion of nutrients from the media to proteins. Nutrients are transported and catabolized to amino acids, which then are used to produce proteins through the activity of ribosomes. The abundance of amino acids links metabolism with protein synthesis through the alarmone ppGpp, which regulates ribosome content directly, and the allocation of resources in the proteome indirectly. Panel A adapted from Klumpp and Hwa (2014), and panel B based on Bosdriesz et al. (2015).

1.4 Cellular structural stability

All cells are enclosed by membranes that surround the cytoplasm and the genome. Phospholipid bilayer acts as a physical barrier separating the interior of the cell from the environment, and in eukaryotic cells, also defines the different organelles inside of the cytoplasm. Along with phospholipids, the cellular membrane also contains membrane-associated proteins, polysaccharides, and peptidoglycans, that form a complex structure.

There are two major groups of bacteria, depending on the structure of their membrane, which can be differentiated by the Gram staining technique, developed by Christian Gram in 1884. The Gram-negative bacteria (negative in the staining test), such as *Escherichia coli*, have three layers; the outer membrane, the peptidoglycan layer, also known as *cell wall*, and the inner membrane (Fig. 1.7A). In contrast, the Gram-positive bacteria, such as *Bacillus subtilis*, lack the outer membrane but present a thick layer of peptidoglycans (Fig. 1.7B) (see review Egan et al. (2017) for further details).

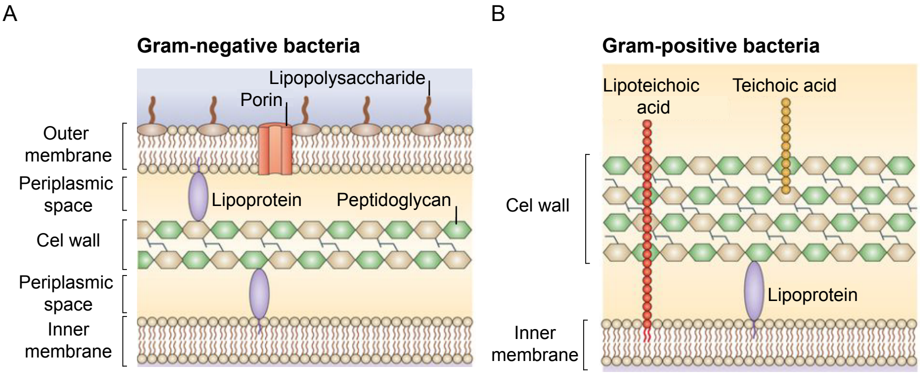

Figure 1.7: Scheme of the membrane structure in gram-negative and gram-positive bacteria. A) Gram-negative bacteria present three differentiated layers, which correspond to the outer membrane, cell wall, and inner membrane, and in between these layers, there is the periplasmic space. Some specific characteristics of this group are that the outer membrane contains lipopolysaccharides, porins, and other transporters and the cell wall is a thin layer of peptidoglycans (PG). B) Gram-positive bacteria present a thick cell wall formed by peptidoglycans and lipoteichoic acid, which is linked to the inner membrane by diacylglycerol. This kind of bacteria lacks the outer membrane. Figure adapted from Brown et al. (2015).

The cell wall is the major component of the cell envelope, and it mainly contains peptidoglycans (PG) that are polymers of sugars linked to a short peptide (three to five amino acids). In general, the cell wall also includes penicillin-binding proteins (PBP) that, as the name already suggests, are the main target for penicillin and other β-lactam antibiotics. This layer is unique in the bacterial kingdom and forms a sacculus that is responsible for the rigidity and shape of the cell, acting as an exoskeleton. It is present in almost all bacteria, with a few exceptions (e.g., *Mycoplasma*). Interestingly, some bacteria in specific conditions can switch to a structural form that lacks the cell wall, named L-form (Allan et al., 2009).

During the cell cycle, bacteria elongate and divide, thus expanding and modulating the structure of the membrane. During elongation, in turn, the action of peptidoglycan hydrolases, also known as autolysins, is critical. These enzymes hydrolize the links between peptidoglycans to allow modulations in the cell wall (Fig. 1.8). At the same time, it is also critical to resynthesize the membrane itself, to maintain the integrity of the cell and its morphology. Peptidoglycan synthases, PBPs, polymerize the glycan chains and cross-link the peptides. Hence, the structure of the bacterial membrane is very dynamic, and the coordination between hydrolysis and synthesis is vital. Some models support that PBPs, PG hydrolases and morphogenesis proteins form complexes that modulate the bacterial cell wall, but the composition of these complexes is still under study (see Typas et al. (2010) for further details).

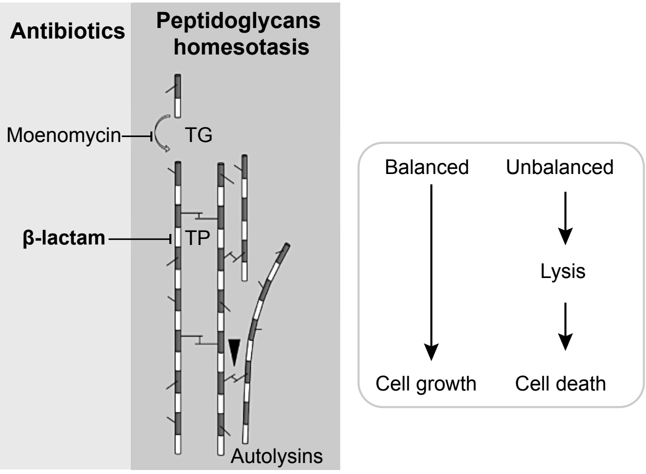

Figure 1.8: Effect of beta-lactams in the peptidoglycan homeostasis. The glycan chains are formed by alternating N-acetylmuramic acid and N-acetylglucosamine (grey and white, respectively). Different chains are connected through peptide cross-links. Autolysins (respresented with a black triangle) can break the links. The correct balance of synthesis and degradation of the cell wall makes cell growth possible. The antibiotics of the Moenomycin family inhibit the transpeptidase function of PBP, and β-lactams inhibits its transglycosylase function. The action of antibiotics creates an unbalance that produces cellular lysis, which eventually will cause the cellular death. Figure adapted from Luo and Helmann (2012).

Many genes are required to generate precursors for the cell wall synthesis, and the correct assembly of all these components is crucial for cell viability. This explains why there are important antibiotics, such as the β-lactams and glycopeptides, that target the bacterial membrane. β-lactams, for instance, inhibit the transpeptidase activity of the PBPs, which affects the peptidoglycan layer and eventually causes cell lysis due to the pressure of the cytoplasm (Fig. 1.8).

Among the complexes that modulate the cell wall, PBPs are the enzymes that have been studied in more detail. These PG synthases present two types: class A (aPBPs) and class B (bPBP). The first class has a transglycosylase domain that polymerizes the glycan strand, and a transpeptidase domain that links the peptide to the structure. This peptide connects to the adjacent glycans, generating the mesh-like layer that surrounds the cell. Class-B PBPs, only have the transpeptidase domain. The bacterial genome usually contains several PBPs, some of them with specific (and sometimes redundant) functionality, such as the creation of the division septum. The regulation of PBP activity remains surprisingly poorly described, despite the clinical importance of antibiotics that target these enzymes (see Sauvage et al. (2008) for further details).

Once the PBPs synthesize the peptidoglycans, the incorporation into the existing wall is regulated by cytoskeletal structures, connected to the cell wall through different proteins. The protein RodZ in *E. coli*, for instance, connects the PBPs to MreB (Mbl and MreBH in *B. subtilis*), which is essential for the elongation of rod-shaped bacteria and dictates the spatial pattern of the bacterial cell wall (Fig. 1.9A). Another example is the FtsZ protein that controls the formation of the ring-like structure, where the different proteins involved in the cell division assemble. This protein promotes the creation of the septum through the link to PBPs (Fig. 1.9B). This septum is formed by PGs and ultimately forms the poles of the two new cells. Hydrolases play a major role in the separation of the PG septum and thus in the division process. AmiC, for instance, is the most important hydrolase for the separation of the two new cells in *E. coli* (Priyadarshini et al., 2006). Despite the existing knowledge of how these different processes are coordinated, the regulation and activity of antibiotics during these vital processes are still unclear.

Besides its fundamental function as a receptacle, the membrane also transports, actively or passively, all kinds of molecules across itself. The difference between the concentration of molecules in the interior and the exterior of the cell creates an electrochemical gradient that cells use for energy production, nutrition, and communication, among other functions. Another role of the membrane is acting as a scaffold for diverse proteins, creating different domains for various cellular processes. For instance, ATP synthesis through the respiratory chain is carried out by membrane-associated proteins. Another example is the already mentioned protein FtsZ, which as discussed above, connects membrane-associated proteins and forms the septum during cell division (Typas et al., 2010). Finally, the membrane can also participate in communication among cells. This includes detecting changes by physical pressure (Blango and Mulvey, 2009),

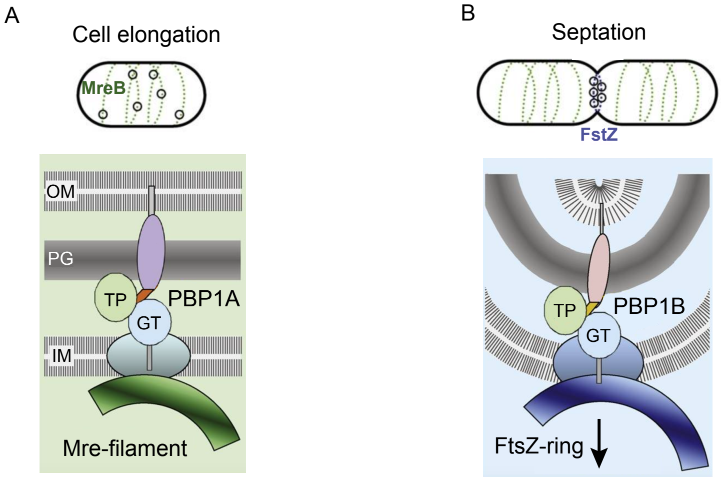

Figure 1.9: Scheme of the PBPs structure during elongation and cell division in *E.coli.* A) MreB and PBP1A are two of the main proteins responsible for side-wall formation during cell elongation. PBP1A contains two parts, the transpeptidase domain (TP), and the transglycosylase domain (GT). This protein contacts the outer membrane through the lipoprotein LpoA. In the inner membrane, cytoskeletal elements and the elongation complex, the *elongasome*, which contains the MreB protein, assemble around the PBP1A. B) MreB and PBP1B are the principal components of the septum. The PBP1B is linked to the outer membrane through the lipoprotein LpoB. On the inner membrane side, this PBP is connected to cytoskeletal elements, FtsZ, and *divisome*. Figure adapted from Typas et al. (2010). For clarity, some of the proteins have been omitted.

and ion transmission, which involves opening and closing ion channels (Prindle et al., 2015).

1.5 Dynamics of the bacterial stress response

The three fundamental regulators of cell proliferation discussed above (cell cycle, biomass production, and structural stability) are essential for cell viability and growth, and interfering with any of them can have a severe impact, generating cellular stress. In bacteria, stress is understood as any kind of perturbation, physical or chemical, that affects growth. For this reason, the first sign of bacterial stress is the reduction of cell proliferation (Hill et al., 2002).

Stress can be categorized into *lethal* or *sub-lethal*, depending on its general effect on cells. Sub-lethal stresses affect cellular function and impair growth, but do not cause cell death. Under this condition, cells can adapt to the harmful environment, and eventually, some cells can become resistant (Hill et al., 2002). According to these observations, it can be useful to study bacterial cells under sub-lethal stress because in these conditions we can observe the strategies that cells can use to become resistant, for example, to survive antibiotic exposure.

Cells have developed different strategies to cope with stress, which fall under the umbrella of what is known as *stress response*. These responses can be general or specialized to the specific stress. Some examples of stress responses are differentiation into a dormant state (e.g., sporulation and persistence), competence, biofilm formation, and DNA uptake, among many others. In all cases, when bacteria perceive the stress, they activate global regulatory circuits that unleash major changes in gene expression and lead to a new physiological state.

The response to stress should be fast enough, and consequently the factors that coordinate the initiation of the corresponding global changes that the cell undergoes have been shown to have interesting dynamics. A particularly interesting example is the expression of the *alternative sigma-factors* (σ-factors) that activate distinct regulatory programs under different cellular stresses. The σ-factors are subunits of the RNA polymerase (RNAP) core, which is responsible for the production of mRNA transcripts. Apart from the constitutive σ-factors, which promote the expression of housekeeping genes, different alternative σ-factors are expressed depending on internal and external conditions, and target the transcription of a subset of genes, reprogramming the bacterial state. For example, in many gram-negative bacteria, the regulation of the general stress response is controlled by the σ^S-factor, encoded by the *rpoS* gene (Lange and Hengge-Aronis, 1991; Lago et al., 2017). In gram-positive bacteria, the general stress response is controlled by the σ^B-factor (Lange and Hengge-Aronis, 1991; Boylan et al., 1993). The regulation of σ-factors consists in a negative feedback mediated by a protein known as *anti-σ-factor*, which is typically located in the same operon as its σ-factor. Thus, the σ-factor is expressed together with its repressor, which is degraded under specific conditions, activating the σ-factor. This kind of regulation generates a pulsatile response, with the pulse frequency depending on the intensity of the stress (Fig. 1.10) (Locke et al., 2011). Recently, a new study demonstrated that multiple alternative σ-factors present a pulsatile response, which allows the cell to minimize the competition for the RNAP pool by time-sharing (Park et al., 2018).

The stress response is a very dynamical process, since cells need to rapidly activate the different pathways to cope with stress, and deregulate them

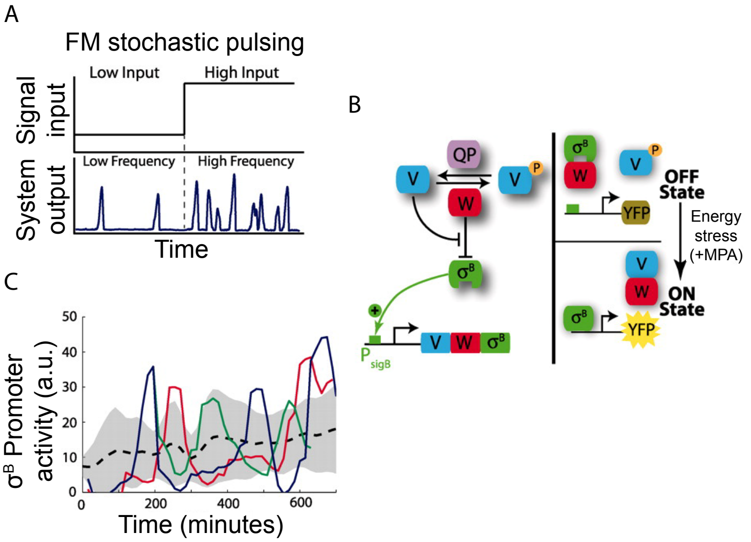

Figure 1.10: Frequency modulation of the pulsatile dynamics of the σ-factor under stress. A) Scheme of the frequency modulation (FM) of the stochastic pulses of the σ^B by the level of stress. A higher level of the signal (top row), produces an increase in the frequency of the system output. B) Diagram of the σ^B regulation. In the OFF state, RsbV (V) is phosphorylated, and the σ^B is inactivated by the binding of its anti-sigma factor RsbW (W). Under stress, such as the energy stress produced by the application of mycophenolic acid (MPA), the phosphatase complex RsbQP (QP) dephosphorylates RsbV, which binds with the anti-sigma factor, releasing the σ^B. In the ON state, free σ^B activates the target genes (including its own operon), and the *yfp* reporter gene (YFP). C) Three examples of time traces for the promoter activity of the P_{sigmaB}-yfp (colored solid lines), and its mean and standard deviation for all lineages (dashed line and shaded area, respectively). Figure adapted from Locke et al. (2011).

after the stress disappears. We next discuss two examples of cellular stress responses that follow very different dynamics.

Under nutritional stress, *Bacillus subtilis* cells have two different pathways that lead to two clearly distinct cellular states: *sporulation* and *competence* (Fig. 1.11A) (Süel et al., 2006; Schultz et al., 2009). Sporulation is a process that involves the activation of around 500 genes, and the first visible step is the formation of an endospore. At the end of the process, the "mother cell" that contains the endospore lyses and releases its DNA into the media. The resulting spore, a dormant cell state that is resistant to chemicals, radiation, and heat, can germinate and start growing again when the nutritional stress disappears. Competence is a *transient* cellular state that allows the uptake of exogenous DNA, to incorporate it into the genome or to use its components as nutrients. Eventually, after several hours in the competence form, cells return to vegetative growth. The majority of the cells under nutritional stress commit to sporulation, but approximately 10% of the population become competent. This small fraction is associated with the stochastic expression of the genes involved in this process. The competence response is triggered by ComK, which controls its transcription through a positive and a negative feedback loop (Fig. 1.11B). This circuit presents the form of an excitable system, and noise can generate the stochastic and transient response (Figs. 1.11C,D).

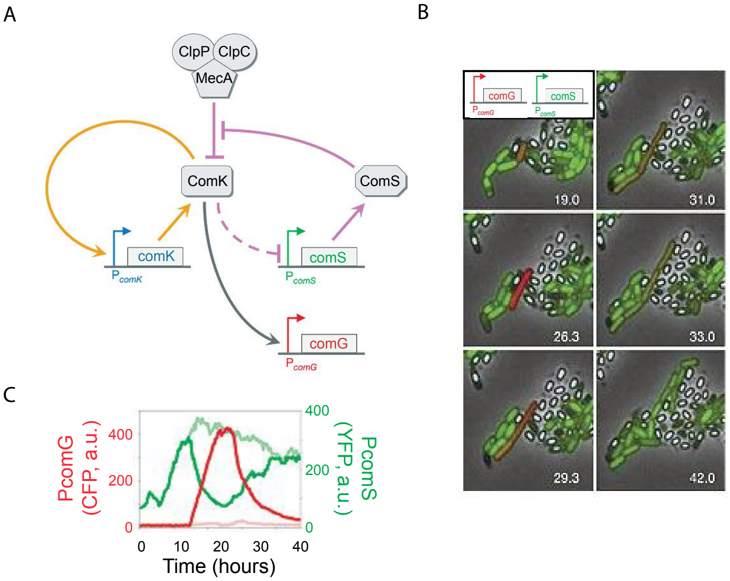

Figure 1.11: The transient state of competence is regulated by the core competence circuit. A) Diagram with the different interactions of the core competence circuit. ComK is subject to a positive feedback loop (orange arrows) and a negative feedback loop through the regulation of ComS (purple arrows). ComS and ComK compete for binding to the proteolytic complex MecA-ClpP-ClpC, and this competition makes ComK more stable in the presence of ComS (which is activated indirectly by nutritional stress). The expression of ComK indirectly inhibits the expression of ComS (dashed purple arrow), which drives the proteolytic complex back to ComK, reducing its concentration. ComK activates *comG*, which is used in the rest of panels of these figure as a marker of competence. B) Filmstrip of a *Bacillus subtilis* microcolony, under nutrient-limited stress conditions, showing a competence event. P$_{comG\text{-cfp}}$ promoter expresses CFP as a marker of competence (red), and P$_{comS\text{-yfp}}$ is marked in green. Spores can be observed as white ovals. The time in hours is represented in each frame. C) Time series of P$_{comG}$-*cfp* and P$_{comS}$-*yfp* for the competent cell shown in panel C. Notice the negative correlation between the expression of the two promoters. Figure adapted from Süel et al. (2006).

Another well-known example of the importance of the dynamics in the stress response is *bacterial persistence*. Persisters are tolerant to lethal concentrations of antibiotics (Balaban et al., 2004; Lewis, 2007) (Fig. 1.12), and consequently the appearance of persistence in clinical infections is one of the causes of the failure of antibiotic treatments, leading to recurrence of the infection. Notice that these cells are not strictly speaking resistant to the antibiotic, as their tolerance is not genetically defined. The percentage of these type of cells is very low (1%), but some studies showed that different types of stress could increase the presence of this response. Some examples are the stringent response (VandenBerg et al., 2016; Liu et al., 2017b), quorum sensing (Leung and Lévesque, 2012), diauxic shift (Amato et al., 2013), acid treatment (Helaine and Kugelberg, 2014), DNA damage (Dörr et al., 2009), and biofilm formation (Lewis, 2010). These cells were first identified in 1944 by Bigger, who hypothesized that cells of *Staphylococcus aureus* that survived after treatment with penicillin had a lack of growth, instead of a genetic alteration. Sixty years later, Balaban and colleagues corroborated Bigger's hypothesis by demonstrating that persister cells do not grow before antibiotic addition, showing that this lack of growth confers them tolerance (Balaban et al., 2004). It is now known that these cells have low or no growth (Wakamoto et al., 2013) and low metabolism (Amato et al., 2013). This response has been found not only in bacteria but also in archaea (Megaw and Gilmore, 2017). This dormant state is transitory, and cells can regain growth once the stress disappears (at the same time, the cells recover the sensitivity to the antibiotic). It seems that the presence of this cell variant could be explained by the formation of micro-environments that could contribute to the heterogeneity, but also by stochastic gene expression in the population. Recent studies have suggested, for instance, that toxin-antitoxin modules play a role in the formation of persister cells, where noise in the expression of the ppGpp molecule dictates the switch between the different cellular states (Tian et al., 2017). This heterogeneity in the toxin-antitoxin module has been identified, for example in the called high persistence mutant (*hip* mutant).

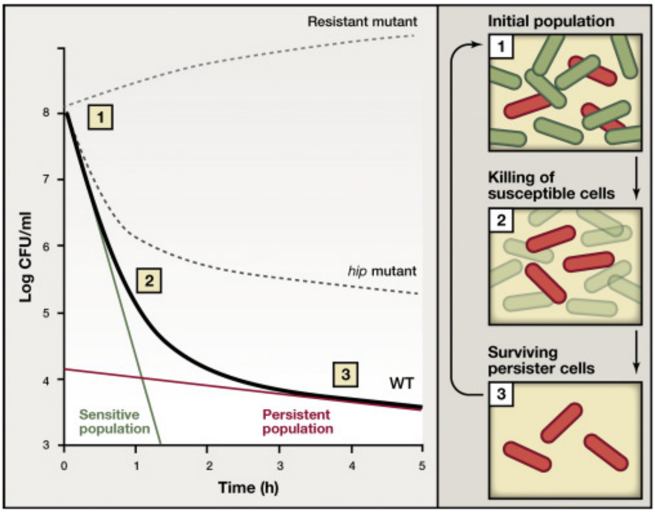

Figure 1.12: Example of a kinetic curve for a population with persisters in presence of an antibiotic. Colony-forming unit (CFU)/ml in logarithmic scale as a function of time for a bacterial population under antibiotic treatment. (1) A lethal dose of an antibiotic is applied at time zero to a growing clonal population of bacteria. This kind of experiment presents a biphasic killing curve. (2) The initial log-linear slope corresponds to the killing rate of the susceptible cells of the population (green line). (3) The remaining cells are tolerant to the antibiotic and are growth-arrested or slowly growing cells. This is captured by the killing curve that reduces the slope (red line). The upper dashed line represents the growth of a resistant strain that has incorporated a mutation that confers resistance. The lower dashed line is a high persister mutant, such as the *hip* mutant reported by the first time by Moyed and Bertrand (1983). Figure adapted from Dalebroux and Swanson (2012).

Besides the importance of the temporal character of these responses, their heterogeneity is also relevant. For instance, we have seen in the examples above that not all the population responds in the same way under stress (competence is restricted to around 10% of the population, and persisters to 1%). Studying the stress response over time at the single-cell level could provide new insights about the mechanisms underlying resistance emergence, for example, to antibiotics. Our work in this direction is discussed in Chapter 4, where we use the bacterial membrane potential as a marker of the response of *B. subtilis* to antibiotic stress.

Chapter 2

Methods

In this Chapter we discuss the different methods that we will use throughout this Thesis. We will cover all the tools, including the molecular cloning techniques, the data acquisition, and the data analysis, that enable the quantitative measurements that will allow us to construct a conceptual framework of the different processes that we are addressing.

2.1 Molecular cloning

The main goal of this Thesis is to understand the molecular mechanisms that underlie the regulation of bacterial proliferation and its response to different biological factors. To that end, we had to use tools that allow the manipulation gene expression, in what is known as molecular cloning. This Section presents an overview of the molecular cloning techniques used in this work.

2.1.1 Plasmids

Bacteria are used in the field of Molecular Biology mainly to clone and replicate DNA. The most used bacterium for these purposes is *Escherichia coli* [1], whose simple culture requirements and rapid growth makes it a clear candidate for those purposes. For example, *E. coli* can duplicate in less than one hour, while mammalian cells need tens of hours to complete one

---

[1] The strains used in research laboratories are derivated from two different strains, K-12 and MG1655. These two strains are non-pathogenic and are considered of Biological Safety Level 1 (BSL-1).

round of replication. For this reason, researchers use *E. coli* as a reservoir for all kind of exogenous DNA, even for other organisms.

The bacterial genome consists in a circular chromosome that contains all the necessary information for the complete bacterial life. Additionally to the chromosome, bacteria can also have extrachromosomal circular DNAs, known as *plasmids* or vectors (Fig. 2.1), which are commonly used for molecular cloning purposes. These plasmids contain, at least, one *origin of replication*, to be able to be copied during the bacterial cell cycle and not be diluted through cell divisions; and a selective marker, usually an *antibiotic resistance gene*. This marker allows us to select the bacteria that have incorporated the plasmid during the transformation process. Plasmids can also harbor a Multiple Cloning Site (MCS). This region of the plasmid contains several restriction sites recognized by different enzymes that cut and linearize the vector for cloning purposes.

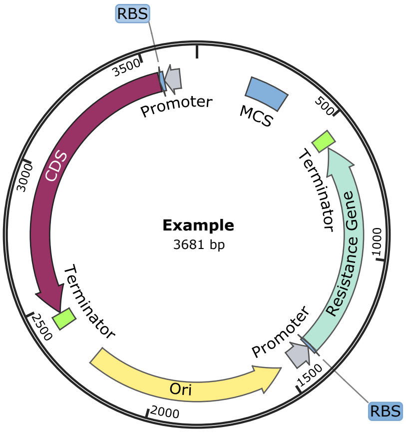

Figure 2.1: Example of a plasmid structure. This example of a plasmid contains an origin of replication (Ori, yellow), an antibiotic resistance gene (green) with the corresponding promoter (gray), the ribosome binding site (RBS, blue) and the terminator (bright green), a multiple cloning site (MCS, blue), and the gene that we would want to express (purple), also with the corresponding parts. The total length of this plasmid is 3681 bp. This image has been generated by using Snap Gene Viewer software.

Several methods of plasmid manipulation exist, including for example cloning based on restriction enzymes or Gibson assembly (which we will discuss in the next Section). Thanks to these techniques, we can introduce DNA constructs inside plasmids that contain all the necessary components to express one or several proteins of interest[2]. When cloned into

---

[2] To express one protein the construct needs to contain a promoter, a Ribosome

the plasmid, these constructs can remain in the structure, or they can be integrated into the genome of the bacteria or other organisms. The maximum DNA length that we can insert into a plasmid is around 10000 base pairs. For longer clonings we need to use alternative methods, such as BACs (Bacterial Artificial Chromosomes) or bacteriophages.

As we mentioned, any plasmid is prepared in *E. coli*, acting as a host, and this plasmid can be later transformed into the organism of interest. For example, this Thesis contains some studies done in *E. coli* but also in *B. subtilis*. The latter bacterium is more challenging to transform and to extract plasmids from, especially the undomesticated strain 3610 that we will use in Chapters 4 and 5. For this reason, even if we are working with bacteria, all plasmids are prepared in *E. coli* and are later transformed into *B. subtilis*. The plasmids that can grow in more than one organism are named *shuttle vectors*, and they need to have multiple origins of replication and various corresponding selectable markers that are recognized by each of the different organisms in which they are used.

2.1.2 Cloning

Molecular Biology provides different approaches to study the function of individual genes, as well as the activity and localization of their proteins. One clear example is the molecular cloning of fluorescent proteins. The discovery of the GFP (Green Fluorescent Protein) from the *Aequorea victoria* jellyfish in the early 1960s, and the posterior cloning of that protein in 1992, were a revolution in the field (Prasher et al., 1992).

The most common approach used in this area is the *promoter fusion*, which consists of cloning into a plasmid a promoter that controls the expression of a fluorescent protein. This promoter can be a natural promoter from the genome; hence, the expression of the fluorescent protein reports on the dynamics of the expression of the gene of interest. The promoter can also be inducible, allowing us to control the amount of expression. In this case, we can express a fluorescent protein or a gene whose level we want to modulate, to see the effect of different levels of activity. Some of the most common inducible promoters are $\mathrm{P}_{\mathrm{lac}}$, from the *lac operon*, controlled by lactose ($\mathrm{P}_{\mathrm{hyperspank}}$ in *B. subtilis*), and the $\mathrm{P}_{\mathrm{BAD}}$ promoter controlled by arabinose.

Besides the promoter fusion, we can also use *protein fusion*, where a

---

Binding Site (RBS), a gene with its corresponding start codon (usually ATG), the coding sequence (CDS) and the stop codon, and a terminator.

fluorescent protein tags the protein of interest, in the C-terminal or N-terminal, in such a way that the fluorescence reporter is physically linked to the protein of interest during the lifetime of the latter. In that case, the marker reports on not only the expression, but also the sub-cellular localization of the protein. This kind of cloning needs particular attention for two main reasons. The first one is that the presence of a tag in the structure of the protein can alter its functionality. Thus, it is necessary to study the possible effects that the tag can cause. The second reason is that the signal of the fluorescent protein depends on the levels of expression of the protein. If we want to increase the signal, we need to overexpress the protein, but this increases the risk of causing side effects. New techniques, such as SunTag for single molecule imaging, are trying to solve these problems (Tanenbaum et al., 2014).

In this Thesis, we use molecular cloning techniques to construct fluorescent reporters which inform about the dynamics of gene expression, as well as the dynamics of bacterial populations.

Isothermal cloning for DNA manipulation

Isothermal cloning, commonly known as Gibson assembly, was described by Gibson et al. and colleagues in 2009. This technique combines basic components of Molecular Biology, such as exonucleases, DNA polymerase, and DNA ligase. The advantages of this technique are multiple, and for this reason, this cloning method has been selected for all the experiments performed in this Thesis. Gibson assembly allows directional construction of multiple fragments in one step (up to 6 pieces), such as a promoter with a ribosome binding site, a coding region, and its terminator. In addition, this technique does not depend on the presence of restriction enzymes and produces a scar-free bound; other cloning methods, such as Gateway or Golden gate, leave unwanted sequences between assembled fragments. Gibson assembly also has a disadvantage, namely that the primers need to be designed specifically for each cloning. Due to the specific homology region that is required to assemble the different pieces, we need to design new primers for each experiment, and they can rarely be reused. This disadvantage can make this technique not attractive for Synthetic Biology, because of its reliance on part modularity.

Gibson assembly works in a single reaction tube that contains the three basic components (Fig. 2.2). The exonuclease hydrolyzes the 5' extreme of the double-stranded DNA and generates single-stranded 3' extremes that include the homologies between them. In the next step, the polymerase synthesizes the remaining regions of the DNA chain after the recombination, and finally, the DNA ligase binds the extremes, creating a complete double-stranded DNA.

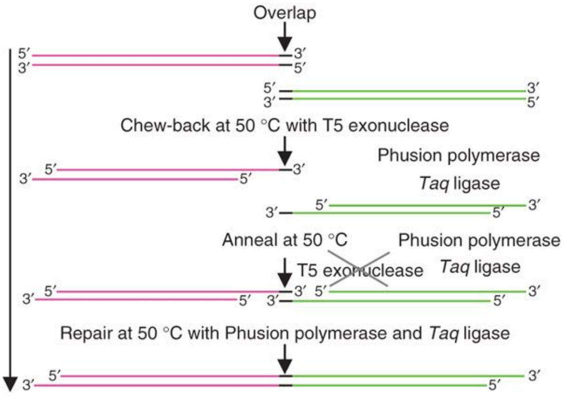

Figure 2.2: One-step Gibson assembly reaction. The two fragments (green and magenta) with homology regions and all the components of the Gibson reaction assembly is introduced in one tub at 50°C for 1 hour. The T5 exonuclease chews-back the 5' extremes of both fragments, generating a single-stranded 3' end in each fragment. The single-strand homology region of both pieces anneal. At that moment the *Phusion* polymerase and the *Taq* ligase repair the gap between the sequences. At the end of the procedure, we obtain a single scar-free DNA. Figure adapted from Gibson et al. (2009)

The specific steps of the process are the following:

1. *Design of the primers.* The fragments to be assembled should be longer than 200 bp and the homology regions should have an overlap of 15-40 bp, avoiding secondary structures such as hairpins. To introduce the overlapping sequence, we need to design primers that contain the homology region, with an optimal length of 25 nucleotides and ∼20 nucleotides for the PCR. A PCR with these primers will amplify the fragments with the regions of overlapping.

2. *Generation of DNA fragments by PCR and gel purification.* After the generation of the pieces by PCR, the product is checked by running it in an agarose gel. If there are unspecific products, it is necessary to perform a gel purification to eliminate components of the PCR and the unwanted fragments. Otherwise, it is possible to purify the product by PCR for a better recovery of the DNA.

3. *DpnI digestion* (optional). If there is a high amount of plasmid used as a template for the PCR, it is recommended to add an extra step of digestion with DpnI enzyme. DpnI degrades methylated DNA;

thus, it eliminates the DNA used as a template, leaving only the one produced by the PCR.

4. *Fragment combination with the Gibson cloning master mix.* In one tube, we add the Gibson Assembly reaction and all the fragments in equimolar concentrations (see Annex 7.1.1 for the reaction mix preparation). The mix is then incubated for 1 hour at 50°C on a thermocycler. In some cases, an extended period of incubation, up to 3 hours, can increase the efficiency.
5. *Desalination or dilution of the product (optional).* Before using the product of Gibson assembly for other procedures, such as transformation or PCR, it is recommended to reduce the concentration of salts of the reaction. 3-fold dilution with purified water or desalination of the sample can be applied for this procedure. This step is mandatory for electroporation protocols.
6. The product can be stored on ice or at -20°C for future use.

Transformation and selection

The generated plasmid can be transformed into different *E. coli* strains used for storage[3], by using a chemical solution of calcium chloride or by electroporation (see Annex 7.2 for details of the transformation protocol). The process of transformation makes cells able to uptake plasmids from the environment. At this moment, the cells can be plated in solid media containing the selection antibiotic, and grown overnight (16 hours) at 37°C. Cells that have incorporated the vector with the marker resistance will grow and generate independent colonies. One can then isolate individual colonies and check by colony PCR if the plasmid that harbors each colony is correct. After this first confirmation, cells from the positive colonies are placed in separate tubes with LB media conditioned with the antibiotic of selection. After overnight incubation at 37°C with shaking, we can take a sample of the culture and freeze it for later utilization. We can also extract the plasmid and send it for sequencing to further validate the construct. Once the construct is validated, the plasmid can be transformed into the organism of interest, such as for instance the *E. coli* strain

---

[3] DH5α or DH10b (commonly known as TOP10) are two strains that can be used for molecular cloning and storage of DNA because of the modifications in their genomes. These modifications make them increase plasmid stability and improve plasmid yield, among others. One can consider using other strains for more complicated cloning. For example, JM110, which cannot methylate DNA, can be used for clonings with restriction enzymes sensible to methylations.

MG1655 or *B. subtilis* strain 3610. As mentioned above, the construct can remain in the vector or can be integrated into the genome (see Annex 7.3.1 for integration protocols).

2.2 Data acquisition

In bacterial cultures, cells divide asynchronously due to intrinsic stochasticity in all the processes involved (e.g. the timing of the initiation of chromosome replication, the velocity of chromosome replication, and so forth). In those conditions, measurements at the population level provide an average of all cells that is missing information about the variability in the population. Depending on what we would like to study, this measurement may not represent the majority of the cells. For example, if a response has a bimodal distribution, the average would not describe any of the two groups. For this reason, in this Thesis we combine single-cell and population measurements to approach different questions. For the single-cell studies we have chosen time-lapse fluorescence microscopy to measure the dynamics of the different molecular processes studied. For the population measurements, we use plate-based assays monitored with a microplate reader, in order to perform multiple studies in one experiment.

2.2.1 Time-lapse fluorescence microscopy

Time-lapse fluorescence microscopy allows monitoring of live cells at regular intervals during long periods of time. The application of molecular methods in the cloning of a fluorescent protein allows researchers to monitor, in real-time, the dynamics of cellular processes, protein localization, and protein activity, among others, at the single-cell level in high temporal resolution (Shimomura et al., 1961; Prasher et al., 1992). Nowadays, a wide range of fluorescent protein variants makes it possible to study multiple processes within cells simultaneously.

The use of fluorescence microscopes has enabled the study of individual cells, giving information about the heterogeneity of a population even with isogenic cells, which has been proved to be important to take into account, and cannot be measured at the bulk. Microscopy automatization makes it possible to monitor multiple replicates, and to compare between different strains and conditions in one experiment. Other quantification techniques present a higher resolution for protein detection but lack temporal resolution, or require the lysis of the cells, eliminating the possibility of studying the same cell over time. The possibility to quantitatively study the dynamics of cellular processes at the single-cell level makes time-lapse fluorescent microscopy the most used technique in Systems Biology.

The general method starts with the introduction of a fluorescent protein or the use of a fluorescent dye to monitor the process of interest (see Section 2.1.2). Cells are placed in agarose pads or in a microfluidic chip whereby cell movements are restricted and allow the tracking of individual cells. Thanks to the automatization of image acquisition, snapshots of the cells are taken at regular times during a period. Before the experiments, it is recommended to perform calibrations to set the timing of exposure for each fluorescent protein to avoid phototoxicity[4] and photobleaching[5]. Once the data from the microscope is obtained, it is necessary to perform an analysis to quantify the different processes. Image analysis techniques have helped to developed algorithms of segmentation and tracking that allow the quantification of thousands of cells in one or a few number of experiments (see Annex 7.4.1 for the detailed protocol for time-lapse movies).

2.2.2 Plate-based assay

The *microplate reader* is an instrument used in plate-based assays for high-throughput quantification of the dynamics of cellular process in liquid culture. This instrument performes multiple measurements at regular intervals for extended periods of time, hence allowing real-time systematic analysis of bacterial growth based on the light absorbance, and the average fluorescence signal of a population. Other measurements, such as luminescence and fluorescence polarization, can also be performed. The assays are carried out in microplates. The most common plate in this technique is the 96-well plate, that allows scanning of that number of conditions and strains in one experiment. This method has cast aside previous techniques, such as colony-forming unit (CFU) quantifications, which count the number of cells in liquid culture by placing them in agar plates and counting the number of colonies that the plates contain. The use of the

---

[4] The repeated exposure of cells to intense light over long periods of time produces radicals that can damage cellular structures and cause cellular death. It is recommended to use fluorophores with long excitation wavelengths, to reduce the damage by shorter wavelength illumination.

[5] Alteration of the fluorophore due to interactions with oxygen molecules during the exposure to high light intensities.

plate reader in Systems Biology provides information on the growth rate dynamics, that can be used in theoretical models to describe the growth curves of the populations (see Annex 7.5 for the detailed protocol for plate-based assays).

In Chapter 5, we will show results obtained in plate-based assays, where we measure absorbance and YFP and CFP (Yellow and Cyan Fluorescent Proteins) fluorescence signals in a population of *E. coli* and *B. subtilis* under the presence of a β-lactam antibiotic.

2.3 Data analysis

From snapshots obtained from time-lapse fluorescence microscopy, we can quantify different characteristics of single cells over time, such as their length, fluorescence intensity, and motility, among others. To perform this quantitative image analysis, we have developed different custom MATLAB (Mathworks) and FIJI (ImageJ) codes that allow us to perform segmentation of the cells and track them in an automatic or semi-automatic way. Thanks to these codes, we can obtain information from hundreds of individual cells, from different strains and under different conditions.

2.3.1 Single-cell tracking

The first example that we would like to show is the obtention of information on cell length and fluorescence. Fig. 2.3A shows consecutive snapshots of phase images overlapped with their corresponding fluorescence image. Through the filmstrip we can observe the growth of a microcolony of the bacterium *E. coli*, as well as the dynamics of a fluorescence reporter. With custom codes which process single-cell information, we can segment and track cells in time, to obtain the whole history of the lineage. In this example, we select one cell from the first snapshot (marked with an arrow), and we can follow the whole lineage of the cell, during hours. From the analysis in the phase-contrast image, we obtain the position and create a mask that covers the whole area of the cell. This ROI (Region Of Interest, yellow outline in Fig. 2.3A) is applied in the fluorescence image, giving us the information of the fluorescence intensity of this specific cell.

From this kind of analysis we obtain information about the length of the cell and the fluorescence intensity over time. Fig. 2.3B shows an example of the time evolution of the length of the cell highlighted in panel A. We can observe that the bacterium grows exponentially, reaches a maximum,

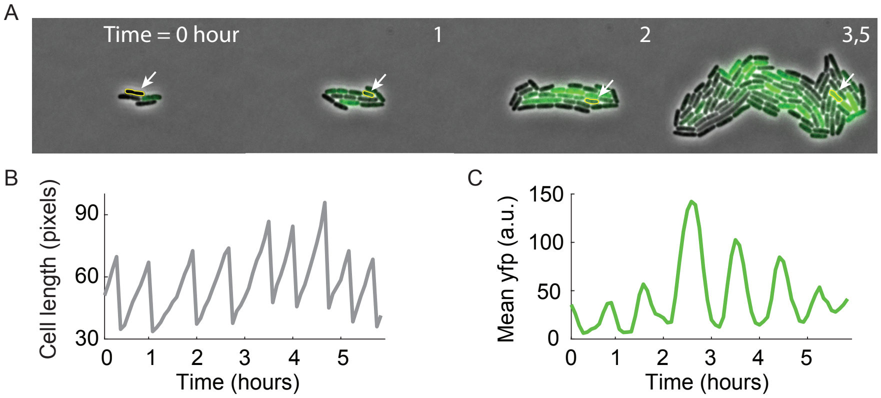

Figure 2.3: Obtention of single-cell elongation and fluorescent signal dynamics from time-lapse microscopy imaging. A) Filmstrip of a microcolony of *E. coli* in phase and overlapped fluorescence. One cell of the microcolony is selected as an example (marked with an arrow). The segmentation creates a mask (yellow outline) that is applied in the fluorescence image. B) Time trace of the cellular length of the selected bacterium in (A). C) Time trace of the mean of the fluorescent protein YPF signal obtained from the mask. Note that this fluorescent protein presents an oscillatory expression.

and the length drops sharply, due to a cell division. After the cell division, the bacterium starts to grow again, beginning a new round of growth and cell division. Fig. 2.3C shows the time trace of the fluorescence signal for the same lineage. This kind of plot gives us, for example, information about the dynamics of the expression of a certain gene or a fluorescent dye under specific conditions. This method will have special relevance in Chapters 3 and 4, which study bacterial dynamics at the single-cell level.

Another quantification that we can obtain from single-cell data tracking is the *elongation rate* for each cell. We can fit an exponential line between consecutive divisions for each cell length time-trace, by using the function $f(x) = ae^{bx}$, where b is the elongation rate of a cell (Fig. 2.4). With this data, we obtain the elongation rate for each cell, as well as the mean elongation rate for the whole lineage.

2.3.2 Segmentation

Phase images with thousands of cells can be automatically segmented using the Trainable Weka segmentation plugin from FIJI (distribution of ImageJ software). This machine-learning plugin creates a classifier that, after training, can segment cells automatically, creating a ROI for each cell

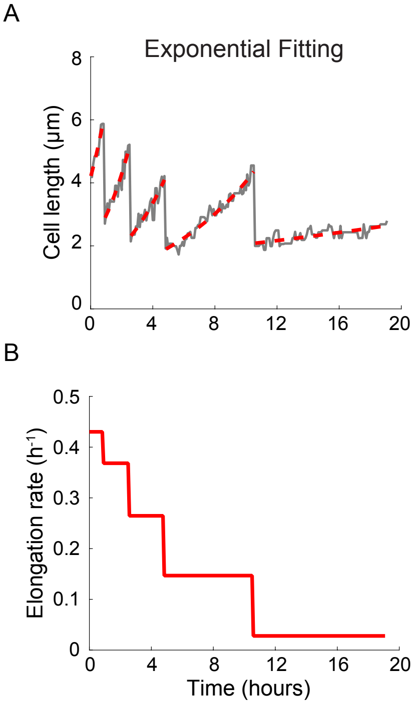

Figure 2.4: Exponential fitting to extract the elongation rate for each cell. A) A gray line marks the cell length (μm) as a function of time (hours), and a red dashed line shows the exponential fitting for each cell cycle. Each cell is considered to cover one cell cycle, and a cell cycle is defined by the cell length, as the period between consecutive divisions. In this example, the lineage undergoes four divisions giving rise to five individual cells. B) Elongation rate (h^{-1}) as a function of time. We can observe that this lineage decreases its elongation rate in each cell division.

(Fig. 2.5). We eliminated non-segmented groups of cells and background noise by the application of a size filter. Furthermore, the Trainable Weka segmentation plugin allows us to classify cells with different characteristics, such as spores and vegetative cells in *B. subtilis*. For the utilization of these ROIs, we have programmed a FIJI code that automatically applies the different ROIs created in each frame to extract the fluorescence signal value for each cell. With this information, we can generate histograms for the fluorescent signal.

2.3.3 Cell motility

Motility is an ability that the majority of bacteria have, to find nutrients and avoid toxic components by means of chemotaxis. This ability is known to depend on different cellular components, such as the membrane potential. We have used Trackmate, a FIJI's plugin that performs single particle tracking (Fig. 2.6). This plugin does an automatic segmentation of multiple frames and finds the trajectories of similar particles over the different frames. This kind of data gives us information about the velocity of the movement of one cell, as well as its tumbling frequency (number of times that a bacterium changes its direction in a given time interval).

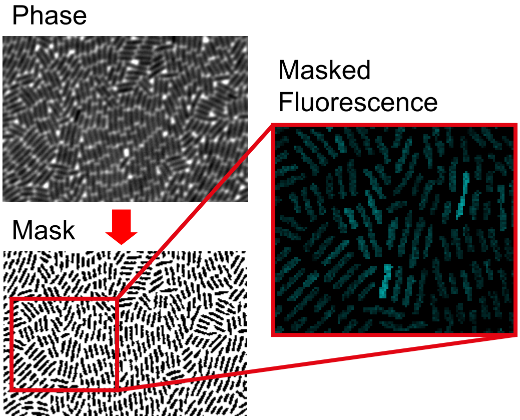

Figure 2.5: Automatic segmentation by using Trainable Weka from FIJI. Example of the image processing for the segmentation. On the top, an image in phase of a microcolony of bacteria, and on the bottom, an image with the masks created through segmentation by the Trainable Weka plugin from FIJI. Later, the generated masks can be applied to the fluorescence image to extract the fluorescence signal of every single cell (right middle plot shows fluorescence in turquoise color).

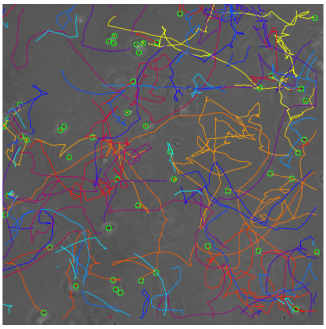

Figure 2.6: Tracking of cells to estimate cell motility. A snapshot of a phase image with overlapped motility traces. Each green circle marks the current position of each bacterium. The colored lines are the trajectory of the individual bacteria.

2.4 Modeling biological systems

All biological systems, from cells and organisms, to populations, have many components that are interconnected, whose behavior changes over time in response to internal and external stimulus. To understand how the whole system operates, we need to study the dynamics that emerge from the different interactions. Most of these dynamics are nonlinear due to the complexity of the interactions, which makes necessary the use of theoretical and computational methods coming from physics and engineering.

Thanks to the recent improvements in Molecular Biology and imaging techniques, it has been possible to study quantitative data in real-time and to obtain valuable information by using the methods that we have seen in previous sections. The data obtained at the single-cell and population levels give us the idea of the fundamental interactions of the system and allow us to develop mathematical models to explain physical phenomena and to make predictions.

Mathematical models are based on a set of interactions and a minimal number of assumptions, constrained by the observations coming from the experimental data. To verify the model and the connections that it establishes, we can generate simulations that should reproduce the observed behavior of the system. Once the model has been confirmed, it is necessary to validate it. The predictions from the model should anticipate the system's response to different scenarios. Once we have tested our model, we can rely on it and use it to explain the mechanisms of the process.

During the process of model building it is necessary to simplify the system as much as possible, highlighting only the minimal relevant interactions. This approach leads to new insights into the results, but makes it necessary to look in detail at the experimental results. Finally, the use of modeling in Biology can propose new kinds of experiments and provide general rules that can be applied to general processes.

In this Thesis, we will use simple mathematical models, presented in the form of Ordinary Differential Equations (ODE), which try to answer specific questions, avoiding very detailed mechanisms. The experimental data that we use to construct the theoretical framework comes from our experiments, using the techniques of time-lapse fluorescent microscopy and plate-based assays. This kind of data is very valuable because it allows us to obtain information in real time at both the single-cell and population levels. The application of our mathematical models gives us a deeper understanding of the experimental data and helps us to consider mechanisms that can explain our results. In Chapter 3, we develop a new model to describe a synthetic oscillator, and use this model to test if the cell cycle is affected by a synthetic gene oscillator design to interact with the former. In Chapter 4, we develop a conductance-based model of ion flux through the bacterial membrane to describe the behavior of the membrane potential under ribosomal stress. Finally, in Chapter 5, a chemical kinetics model of the interaction between a beta-lactam antibiotic and its target within the cell allows us to understand the effects of inter-species interaction in the response of a mixed-species community to the antibiotic.

Part II

Results

Chapter 3

Cell cycle modulation by an intracellular oscillator

A large number of cellular processes with very different dynamics coexist within a cell and interact in an organized way to ensure the correct functioning of the organism. While some of these cellular processes, such as the cell cycle and the circadian rhythm, have been studied over years and our knowledge about them keeps increasing, it is still not well understood how these processes are coordinated with each other, especially if the processes are time-dependent.

In this Chapter we study the effect of the interaction of oscillatory cellular processes upon the cell cycle, and how this connection affects to it. With this purpose, we employ synthetic biology approaches, particularly through the use of a synthetic oscillator as a proxy of non-cell-cycle related oscillatory processes that commonly exist in cells, such as the circadian rhythm. This strategy allows us to study the effect of the oscillator on the cell cycle with a situation in which this coupling is not present, which cannot be done in the case of a natural oscillator, where the coupling is always present. For a better understanding of the experimental results, we also present a mathematical model, developed by Dr. Marta Dies, that helps us to understand the underlying mechanisms of the interaction between the oscillators.

3.1 Coupling between the bacterial cell cycle and the circadian rhythm

Multiple cellular processes coexist within cells, and, interestingly, some of these dynamics take the form of oscillations with a wide variety of periods, ranging from seconds to days (Novák and Tyson, 2008). These oscillators are not isolated from the rest of cellular processes, and they interact between them adapting their responses (Kruse and Jülicher, 2005). In the 17th century, Huygens showed that two oscillators could be synchronized when their ticking is transmitted through a physical connection, an effect called *mutual synchronization* Huygens (1669). The coexistence of more than one oscillator within a cell thus leads to the possibility of phase locking between them. Here we study the effect produced by a cyclical process, mimicking the circadian rhythm, upon the cell cycle.

Several works have established that the circadian clock acts as a pacemaker, to the cell cycle, entraining it such that it adapts its frequency to that of the circadian clock, resulting in the synchronization between the two oscillators (Mori et al., 1996; Yang et al., 2010; Dekens et al., 2003; Salter et al., 2003; Nagoshi et al., 2004). The mechanism of interaction has been proposed to be via transcriptional regulation of components involved in the replication and cell division, such as the CLOCK-BMAL1 complex in mammalian cells (Matsuo, 2003). Apart from mammalian cells, entrainment of the cell cycle by the circadian clock has been observed in many different organisms, including prokaryotes, and the alteration of the interaction between these two oscillators can have dramatical consequences, for instance, causing metabolic impairment and cancer (Sahar and Sassone-Corsi, 2009; Ferrell and Chiang, 2015). In turn, we can also expect that the cell cycle should entrain the circadian clock through discrete variations in the gene-copy number, as an effect of the DNA replication and cell division (Kaasik and Lee, 2004; Feillet et al., 2014). The existence of mutual co-entrainment is however still under debate, with some authors pointing directly to purely unidirectional coupling from the circadian clock to the cell cycle (Matsuo, 2003). These studies, however, lack a clear control situation with which to compare the effects of the coupling, due to the impossibility of eliminating the effect of the circadian rhythm upon the cell cycle.

To address this issue, here we use a synthetic oscillator in *Escherichia coli* as a proxy of a natural oscillator (Stricker et al., 2008). The synthetic nature of this oscillator implies that it is in principle not coupled to the rest of the cellular process, in particular the cell cycle. We can then introduce an ectopic coupling from the synthetic oscillator to the cell cycle by placing one of the central cell cycle regulators under the transcriptional control of the proteins involved in the synthetic oscillator. This allows us to compare the coupled situation with the baseline one in which there is no effect of the synthetic oscillator to the cell cycle. In that baseline case the coupling is unidirectional, going only from the cell cycle to the synthetic clock (through the periodic modulation of the gene copy number of the synthetic circuit). Thus a comparison between unidirectional and bidirectional coupling gives us a clean view of the effect of a periodic cellular process on the cell cycle.

3.2 Bacterial cell cycle

As described the Introduction1.2 the bacterial cell cycle proceeds through its consecutive phases with a certain periodicity, under constant conditions. For this reason, this fundamental cellular process can be considered an autonomous oscillator. From a general point of view, the initiation of the cell cycle can be ascribed to the initiation of chromosome replication.

3.2.1 Initiation of chromosomal replication

The initiation of chromosome replication is considered as a checkpoint of the bacterial cell cycle that depends on the balance between the activators and inhibitors of the process (Skarstad and Katayama, 2013). One of the key molecules that determines the initiation is the highly conserved ATPase DnaA (Donachie and Blakely, 2003; Katayama et al., 2010). At the time of the initiation of replication, this molecule is attached to the *oriC* site, specifically to DnaA-boxes, where there are AT-rich sequences that facilitate the opening of the two DNA chains (Fuller et al., 1984; Duderstadt et al., 2011). The binding of DnaA to the *oriC* promotes the union of the DnaB helicase that expands the unbinding of the two chains (Kaguni, 2006). The separation of the DNA chains enables the loading of the replisome, which once assembled replicates the circular chromosome bidirectionally.

There are different controls of the initiation of chromosome replication to ensure the coordination between the cell cycle and the DNA duplication, especially on the amount of active DnaA and its activity. One of the main controls requires the RIDA system (Regulatory Inactivation of

DnaA), constituted by Hda protein and the β-clamp subunit of the DNA polymerase III, DnaN (Katayama et al., 1998; Kato, 2001; Collier and Shapiro, 2009). The RIDA system inactivates DnaA by the hydrolysis of DnaA-ATP to DnaA-ADP, reducing the amount of the active form of the protein (Katayama et al., 2010; Camara et al., 2005; Kaguni, 2006). Another control occurs immediately after the initiation of the replication. The inhibitor SeqA follows the replisome, binding to newly replicated GATC sequences in the whole genome, which are hemymethylated (Brendler et al., 1995; Brendler, 1999; Marczynski et al., 2015) (Fig. 3.1). Some of the GATC sites are located in the *oriC*, where the *dnaA* promoter is located (Ulrik von Freiesleben et al., 1994; Slater et al., 1995; Lu et al., 1994; Waldminghaus and Skarstad, 2009). During the period that SeqA blocks the sites located in the origin of replication, known as *eclipse period*, the production of new DnaA is inhibited, and the replication machinery cannot start new rounds of replication (Lu et al., 1994; Skarstad et al., 2000; von Freiesleben, 2000). Finally, there is a titration of the DnaA proteins in the *datA* locus (Ogawa et al., 2002). This sequence in the chromosome has several DnaA-boxes, and it promotes the binding of the DnaA proteins reducing the total amount available in the cell. Apart from the inhibitors that act upon DnaA, DnaA itself produces an autoregulation acting as a transcription factor, inhibiting its expression and the expression of other genes.

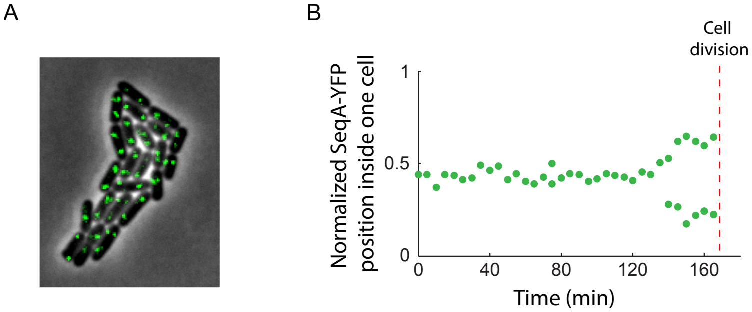

Figure 3.1: Bacterial cells go through one round of DNA replication under slow growth conditions. A) The filmstrip contains a merging of phase and fluorescence microscopy images, where the protein SeqA-YFP is colored in green. To monitor the chromosomal replication dynamics in living cells, SeqA is tagged with the fluorescent protein YFP. This protein follows the replisome as it progresses along the chromosome. B) Position of SeqA-YFP protein inside one cell over time. In the y-axis, 0 and 1 mark the two poles, being 0.5 the middle of the cell. Replication initiates near the middle of the cell and after a period of time it is duplicated, meaning than the duplication of the chromosome progresses. The protein SeqA-YFP moves to the poles before cell division.

External factors such as temperature and nutrients can also control the timing and the number of initiations of the chromosome replication (Yoshikawa et al., 1964; Skarstad et al., 1986). Under slow growth conditions, *E.coli* has one chromosome per cell, which is replicated only once during the cell cycle (Fig. 3.1). Hence, the gene copy number goes from one to two copies, per cell cycle. Under fast growing conditions, the timing for the chromosome replication (C period) is shorter than the complete cell cycle. In this situation, the bacteria start new rounds of replication before division, generating multiple replication forks. Thus, under fast growing conditions, the number of gene copies would be larger than two.

3.3 The synthetic oscillator

The complexity of the natural oscillators and their embedding within the normal physiological processes of the cell makes it difficult to study the interactions between the different oscillatory processes. Synthetic Biology provides new tools for the development of synthetic gene circuits that can be easily controlled and are isolated by design from the natural physiology of the cell (Elowitz et al., 2002; Prindle et al., 2014).

Here, as a proxy of the circadian clock, we use a synthetic oscillator designed in *E. coli* by Stricker et al. in 2008, which is highly robust and tunable. This synthetic biological clock is controlled by an inducible combinatorial promoter known as $P_{lac/ara}$ (Fig. 3.2). This hybrid promoter contains an inhibition site, the *lacZYA* promoter, and an activator site, the *araBAD* promoter. With the combination of the two sites, the expression is inactivated by the tetramer LacI protein in the absence of β-D-1-thiogalactopyranoside (IPTG, an analog of lactose) and activated by the dimer AraC protein in the presence of arabinose. The same promoter is located in different modules controlling the expression of three genes: *araC*, *lacI*, and *yemGPF* (Yeast-Enhanced Monomeric Green Fluorescent Protein), all of them tagged with the *ssrA* degradation sequence. The presence of arabinose and IPTG in the media produces the transcription of the different components of the system (*gfp*, *araC*, and *lacI*), where GFP expression acts as a reporter of the state of the oscillator.

The circuit works in such a way that high AraC concentration results in activation of the transcription of all three components of the system, producing a positive feedback loop. Once the level of LacI reaches a threshold, transcription of the $P_{lac/ara}$ promoter is inhibited and the expression is reduced, generating a negative feedback. The combination of the positive and negative feedback loops gives rise to sustained oscillations of protein expression, giving a pattern of “off-on-off-on” at the single-cell level that is reported by GFP expression (Fig. 3.3). Note that as in previous synthetic oscillators, there is a loss of synchronization in each generation which could be caused by noise in the system, resulting from a variety of factors such as variations of the number of plasmids and the amount of resource molecules (RNA polymerase, ribosomes) in each bacterium.

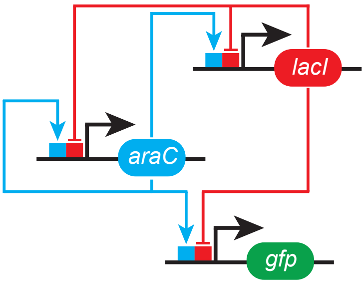

Figure 3.2: Scheme of the synthetic oscillator. The hybrid promoter formed by $P_{lac/ara}$ controls the expression of *lacI* and *araC* genes, as well as *gfp* gene. The activating and inhibiting interactions of the system form a positive and a negative feedback loops. The expression of the *gfp* gene acts as a reporter of the state of the circuit.

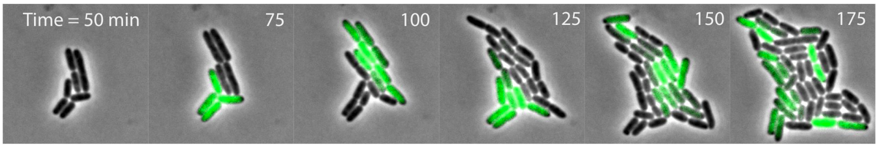

Figure 3.3: Filmstrip of a microcolony containing the synthetic oscillator. The filmstrip contains a merging of phase and fluorescence microscopy images, where the GFP is colored in green. The state of the genetic circuit, captured by GFP, follows a heterogeneous ‘off-on-off-on” oscillating pattern in single cells.

3.4 Effect of the cell cycle on the synthetic oscillator

To characterize both oscillators, we first determine the natural period of the cell cycle and the synthetic oscillator in the ‘unidirectional strain’ (strain that contains the original synthetic circuit, in which the cell cycle affects the synthetic clock, but not vice versa). With this purpose, we quantify the dynamics of the two oscillators in real-time and at the single-cell level by filming microcolonies in agarose pads with time-lapse fluorescence microscopy, growing in a minimal medium containing 0.7% arabinose (w/v), 2mM IPTG and 0.4% glucose (w/v). The cell cycle was determined by tracking over time the cell length of single cells, as a proxy of the state of the cell cycle (Fig. 3.4). Each cycle is bounded by two successive cellular divisions where the bacterium is "born" after a division, elongates exponentially and finishes its cell cycle on the next division. For the synthetic oscillator, the fluorescent signal was obtained from the time traces, and it was used to quantitatively determine the state of the synthetic circuit, since the $P_{lac/ara}$ controls the GFP protein expression, like the other components of the synthetic circuit. Under these experimental conditions, the intrinsic periods for the cell cycle and the synthetic oscillator have a mean period of 47 ± 12 min and 54 ± 12 min, respectively (Figs. 3.4C,D). From these results, we can observe that the two oscillators have similar periods.

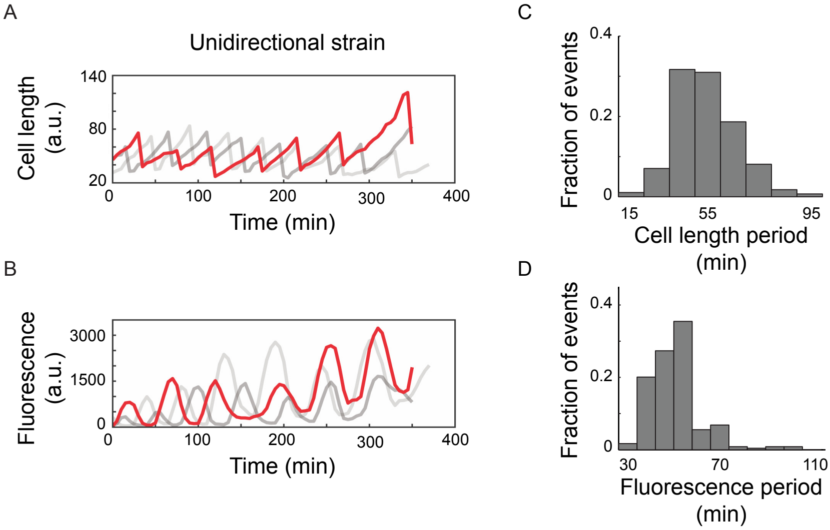

Figure 3.4: Representative time traces and characterization of cell length and fluorescence signal in the unidirectional strain. A) Cell length as a function of time for three independent lineages. An example is highlighted in red. B) From the same lineages as in cell length, the fluorescence signal from the synthetic oscillator is represented as a function of time. An example is highlighted in red. C) Distribution of the cell length period for the unidirectional strain ($n = 284$). D) Distribution of the fluorescence period from the synthetic oscillator in the unidirectional strain ($n = 234$).

To determine the degree of coupling between the two oscillatory processes (Pikovsky et al., 2002), we proceed with the study of the phase shift (Rosenblum et al., 1996) by performing a pulse-triggered average (PTA).

From the time series, we define a phase that corresponds to the progress of the system through a cycle, and we assign a value to each point of the phase. The cell cycle is defined as the period from the minimum to the maximum of the cell length, and each data point of the segment was assigned from 0 to 1 (Fig. 3.5A). Fluorescent data were also segmented according to the cell cycle phases, and again, data points were assigned from 0 to 1. We determined where the location of the maximum of the fluorescence within its assigned cell cycle (Fig. 3.5B). To help with the interpretation of the data, we redefine the cell cycle phases in such a way that 0.6 indicates the initiation of the cell cycle (minimum cell length) and 0.5 indicates the end, just before the cell division (maximum cell length). With this redefinition, it is more evident to appreciate a unimodal distribution of the timing where the maxima of the synthetic oscillator occurs, located near the beginning of the cell cycle. The non-uniform character of the phase distribution indicates that the relation of the phases of the two oscillators is not entirely random, exhibiting a partial entrainment of the synthetic oscillator through the cell cycle.

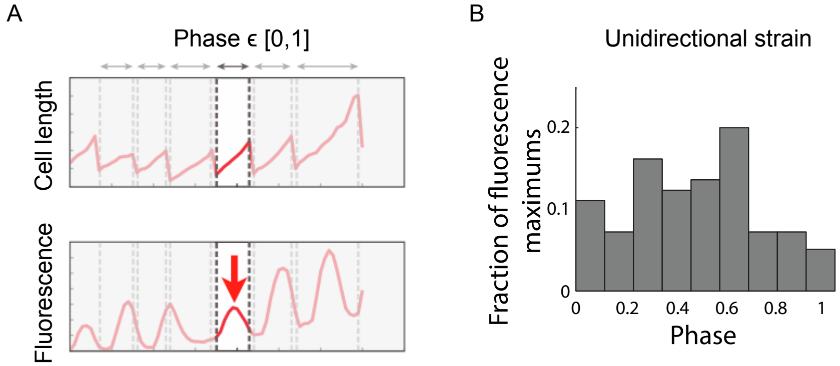

Figure 3.5: Phase shift between the two oscillators for the unidirectional strain. A) Representation of the phase difference assignment between the cell cycle and the synthetic oscillator. For each cell cycle that goes from one cell division to the next (0 to 1), a maximum of fluorescence is assigned. B) Experimental distributions of the timing of fluorescence maxima within the cell length cycle for the unidirectional strain ($n = 140$). Note that the x-axis covers a whole cell cycle of every single cell. For a better visualization of the data, the phase has been redefined so that the initiation of the cell cycle starts at 0.6 and finishes at 0.5.

3.5 Back-coupling from the synthetic oscillator to the cell cycle

To generate a back-coupling between the synthetic oscillator and the cell cycle, a new synthetic interaction was designed and constructed to enable the control the of chromosome replication. Specifically, we chose the RIDA system (Hda and DnaN) as a negative regulator of the initiation of the chromosome replication by the synthetic clock described above. In Section 3.2 we have seen that this system inhibits replication initiation by decreasing the amount of DnaA available in the cell. To avoid modifying the original synthetic oscillator, we designed a separate plasmid that contains another copy of the hybrid promoter $P_{lac/ara}$, controlling the transcription of the *hda* and *dnaN* genes (Fig. 3.6). The expression of inhibitory components of the chromosome replication produces a back-coupling from the synthetic oscillator to the cell cycle, in such a way that if there is an expression of the components of the synthetic oscillator (active state), the RIDA system is also expressed and produces a delay in the initiation of chromosomal replication. The strain that contains the original synthetic oscillator and the new plasmid with the RIDA system is called the ‘bidirectional strain’[1] below. To avoid differences on the number of plasmids and possible overloading between the unidirectional and bidirectional strains because of the presence of a third plasmid, we introduced in the unidirectional strain a plasmid that only contains the origin of replication and the antibiotic resistance.

---

[1] To avoid incompatibility with the plasmids of the synthetic oscillator, we placed the RIDA system in a plasmid with a stringent origin of replication (pSC101). This origin of replication is regulated in the same manner as the chromosome (specifically, it depends on DnaA).

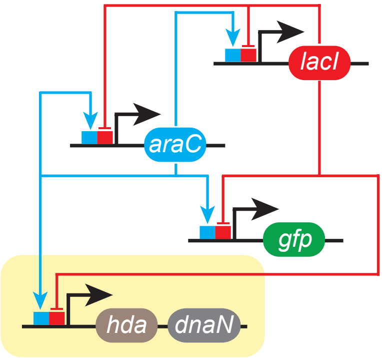

Figure 3.6: Scheme of the synthetic oscillator and its coupling to chromosomal replication. The hybrid promoter $P_{lac/ara}$ controls the expression of *lacI* and *araC* genes, as well as *gfp* gene. The same promoter drives now the expression of the RIDA system (*hda* and *dnaN* genes) that inhibits chromosome replication, producing a back-coupling from the synthetic oscillator to the cell cycle.

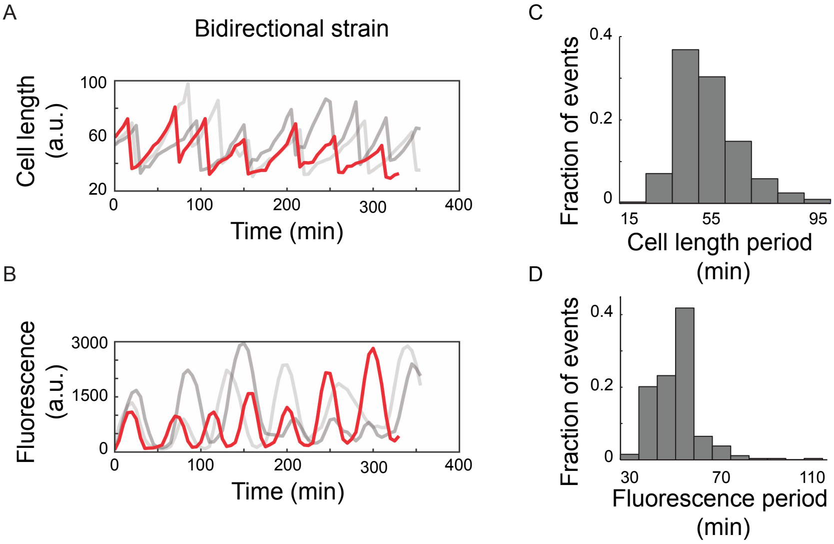

Figure 3.7: Representative time traces and characterization of the periods for the cell cycle and the synthetic oscillator in the bidirectional strain. A) Cell length as a function of time for independent lineages. An example is highlighted in red. B) Fluorescence as a function of time for the synthetic oscillator coupled to the cell cycle. An example is highlighted in red. C) Distribution of the cell length period for the bidirectional strain ($n = 323$). D) Distribution of the fluorescence period from the synthetic oscillator for the bidirectional strain ($n = 263$).

As we did for the case of the unidirectional strain, we quantify the intrinsic periods of the cell cycle and the synthetic oscillator obtained from the time traces (Fig. 3.7). The mean of the distribution of the cell cycle and the synthetic oscillator periods are 47±12 min and 54±10 min, respectively, in the same experimental conditions as the unidirectional strain. The results indicate that the introduction of the back-coupling does not noticeably affect the period of the oscillators.

For the quantification of the phase shift, we use the PTA method. The distribution of the fluorescence maxima within the corresponding cell cycles is represented in Fig. 3.8B. The results show phase locking with a clear unimodal distribution. Comparing the unidirectional and the bidirectional strains, we can observe that the synchronization between the two oscillators increases by introducing a back-coupling from the synthetic oscillator to the cell cycle.

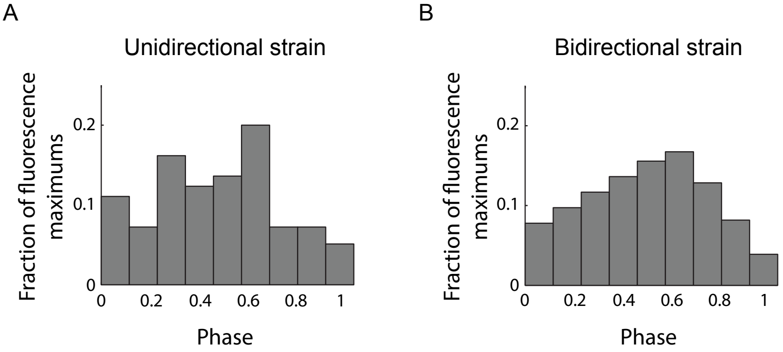

Figure 3.8: Comparison of phase shift between the unidirectional and bidirectional strain. A) Experimental distributions of the timing of fluorescence maxima within the cell length cycle for the unidirectional strain ($n = 140$). Same data as in Fig. 3.5. B) Experimental distributions of the timing of fluorescence maxima within the cell length cycle for the bidirectional strain ($n = 171$). Note that the distribution of the bidirectional strain is clearly unimodal.

3.6 Modeling the coupling between oscillators

For a better understanding of the experimental results, we propose a minimal-mechanism model to describe the synthetic oscillator in the unidirectional strain, which is inspired by the two-component activator-repressor system from Rué and Garcia-Ojalvo in 2011. In the model, an activator (A) and a repressor (R) are controlled by the same promoter (Fig. 3.9), creating a positive and a negative feedback loops (see *Unidirectional model* 3.9.2

for the equations of the system).

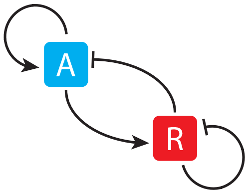

Figure 3.9: Scheme of the interaction between the components of the synthetic oscillator. The activator (A) promotes the expression of the repressor (R) and itself. In turn, R inhibits the expression of A and its own.

Fig. 3.10A shows that this minimal model produces oscillations in the levels of the components of the circuit (A and R), which would correspond to the oscillations in the fluorescent protein GFP obtained in the experimental results (Fig. 3.10B). Since the model does not consider a fluorescent reporter, in the simulations we will consider the levels of the activator (A) as the state of the synthetic oscillator. To validate the model, we study the effect of reducing the degradation rate of the components of the system in accordance to structural differences between them (dimer, $\delta \sim 0.7$ and tetramer, $\delta \sim 0.4$, see Eqs. 3.1 and 3.2).

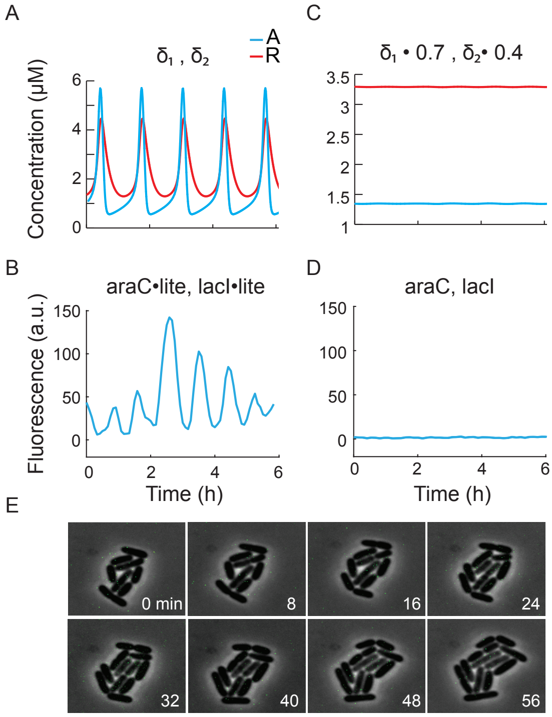

Figure 3.10: Simulated and experimental time series of the minimal model. A) Numerical integration of the synthetic oscillator model. The concentrations of the activator (A) is marked in blue, and the inhibitor (R) is in red. Because both components have the same promoter, the expression of the two proteins behaves in a similar way over time. B) Experimental time series for GFP fluorescence (blue line) from one independent lineage containing the synthetic oscillator. C) Prediction of the concentrations for A and R, reducing the degradation rates by 0.7 and 0.4, respectively. D) Experimental time trace of GFP fluorescence in a strain that contains the synthetic oscillator without the degradation tags. E) Filmstrip with phase and fluorescence overlapped, for the strain that contains the modified synthetic oscillator without the degradation tags. Every frame is taken every 8 min, and the time-lapse series spans one hour. For this specific figure, we did not used the same parameters than in previous figures.

Experimentally, this modification can be interpreted as the elimination of the degradation tag that the proteins contain. The removal of the degradation tags increases the half-life of the proteins and, counterintuitively, the model predicts that it eliminates the oscillations of the system and the state is kept in an 'off' state (Fig. 3.10B). As we can see, the experimental results are consistent with the prediction (Figs. 3.10B,C).

In order to avoid having to make too many mechanistic assumptions, we have used simplified version of the cell cycle in the form of an *integrate and fire mechanism*. This type of model integrates past steps, in combination with a mechanism that triggers an new event after reaching an established threshold. In this phenomenological model of the cell cycle, the length of the cell increases exponentially and encounters a first critical threshold for chromosomal replication (R_{thr}) (Fig. 3.11A). At threshold, the number of genes is doubled, which leads to a doubling of the production rates of all the species. The cell length continues its progression reaching an established second threshold for cell division (D_{thr}) that returns the cell length and production rates to their original values. Note that for these experiments, bacteria were grown in minimal medium. For this reason, we consider that *E.coli* undergoes just one round of replication, producing one doubling of the number of genes. It is also important to notice that we consider that the doubling of all the species is produced at the same time, without taking into account the possible differences of timing due to the different locations of the genes in the plasmids.

For the bidirectional strain (Fig. 3.11B), the RIDA system (variable B in the model) is also controlled by the same promoter. In this situation, B mediates the back-coupling of the synthetic oscillator to the chromosomal replication by increasing the threshold R_{thr}. As can be seen in Eq. 3.8, η establishes the level of back-coupling, going from $0 < \eta \leq 1$, where 0 is a situation without back-coupling and 1 represents the maximum. By increasing η, the back-coupling increases the threshold of replication that creates a delay in the replication of the chromosome. This delay mimics the inhibition of the initiation of the chromosomal replication that the RIDA system produces.

Fig. 3.12 shows the simulated traces for the synthetic oscillator that is driven by the cell cycle ($\eta = 0$, left) and back-coupled to the chromosomal replication ($\eta > 0$, right). The corresponding time traces for independent lineages from the unidirectional and bidirectional strains are also represented in the figure. The periods obtained for the cell cycle and the synthetic oscillator for the unidirectional strain ($\eta = 0$) are 44 ± 14 min and 45 ± 13 min. For the bidirectional strain ($\eta = 0.4$), the values obtained are 45 ± 17 min and 46 ± 12 min (Fig. 3.13). Hence, the values obtained from the model are in agreement with those observed experimentally.

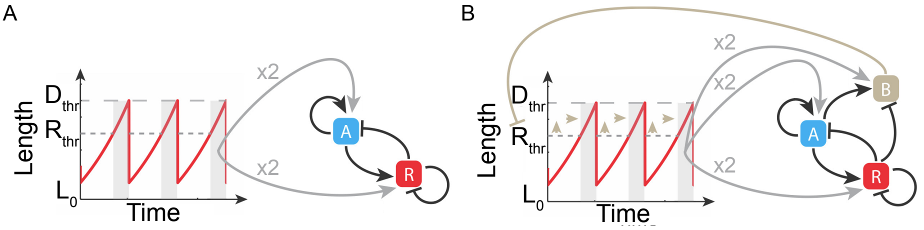

Figure 3.11: Diagrams of model interactions. In these diagrams A is the activator (AraC), R the repressor (LacI) and B the inhibitor of the initiation of chromosome replication (RIDA system). Cell length increases exponentially between division events. When it reaches the replication threshold (R_{thr}) all the productions from the synthetic oscillator are doubled (gray areas). Once cell length reaches the division threshold (D_{thr}), it returns to its initial value (L_0), and the synthetic oscillator productions are reset to their original rates. This sequence of events is applied to both the unidirectional (A) and bidirectional (B) cases. In (B), the oscillator inhibits replication initiation by increasing R_{thr} so that it narrows the time intervals where the oscillator production rates are doubled (gray areas are pushed towards the right).

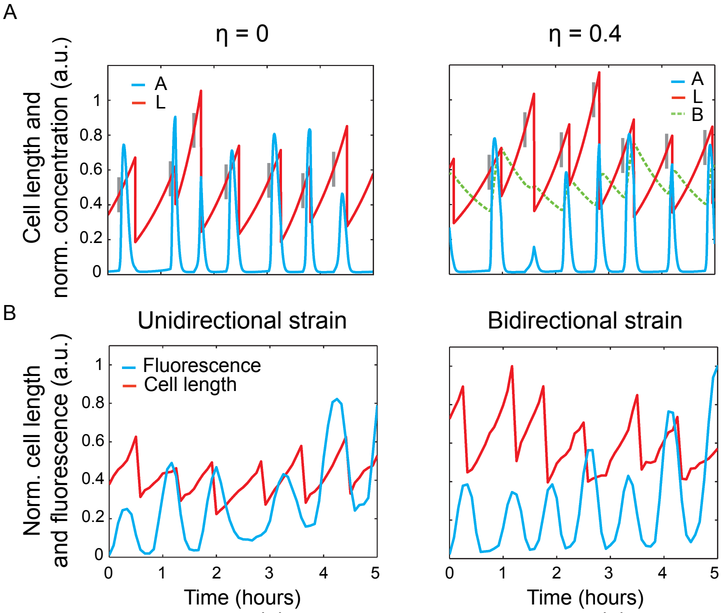

Figure 3.12: Simulated and experimental time series of the coupled oscillators for the unidirectional (left) and bidirectional (right) cases. A) Numerical integration of the coupled oscillator model. Cell length (L) is shown in red and the normalized concentration of the activator (A) in blue. In every cell cycle, the replication threshold (R_{thr}), for each cycle, is indicated as a vertical gray bar. In the bidirectional case (right) the time series for B are also plotted (green dashed line). B) Experimental time traces of the cell length (red line) and GFP fluorescence (blue line) in one independent lineage for the unidirectional and the bidirectional strains.

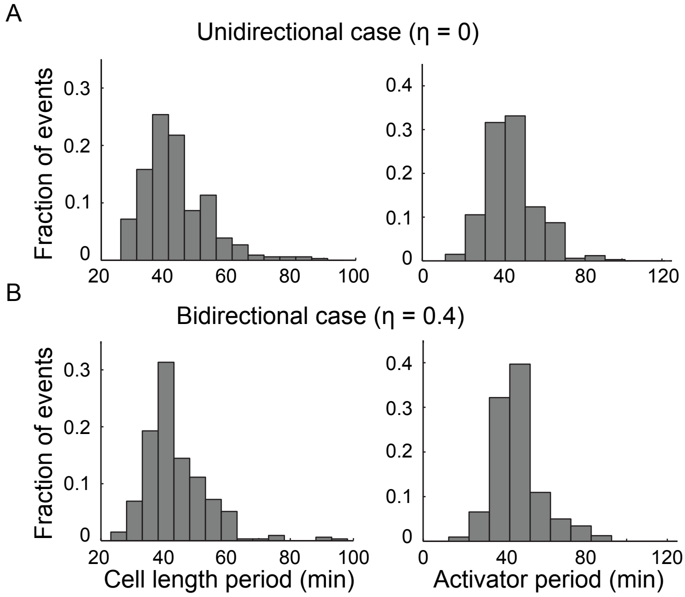

Figure 3.13: Distributions of the periods of the cell cycle and synthetic oscillator obtained from the computational model. A) Unidirectional case ($\eta = 0$), for which a period of 44 ± 14 min was obtained for the cell cycle ($n = 335$), and 45 ± 13 min for the synthetic oscillator ($n = 332$). B) Bidirectional case ($\eta = 0.4$), the period for the cell cycle ($n = 332$) and the synthetic oscillator (N = 320) were 45 ± 17min and 46 ± 12min, respectively.

As we did for the experimental data, the phases of the cell cycle were assigned to the activator traces (see Section 3.5). The results for the unidirectional and bidirectional strains are represented in Fig. 3.14, which shows that the distributions of the timing for the activator concentration maxima within the cell cycle are in good qualitative agreement with the experimental ones (Fig. 3.8).

As a control for the model, we also considered the theoretical scenario where there is no coupling between two oscillators ($\zeta = 0$, $\eta = 0$ in Eqs. 3.6, 3.7 and 3.8). In this situation, the distribution of the histogram for the phase shift between the activator and the cell length shows an erratic behavior, due to the free-running character of the synthetic oscillator rhythm. Comparing the phase distributions between the unidirectional strain (Fig. 3.8A) and an ideal case in which there is no coupling whatsoever between the two oscillators (something that cannot be accomplished experimentally), we can easily appreciate the existence of synchronization between the synthetic oscillator and the cell cycle phase. In the condition with back-coupling from the synthetic oscillator to the cell cycle (Fig. 3.8B), the phase shift has a clear unimodal distribution, indicating an increase of the synchronization through the inhibition of the chromosomal initiation. Hence, the mutual regulation causes an increase in the co-entrainment of the cell cycle and the synthetic oscillator (Fig. 3.15A).

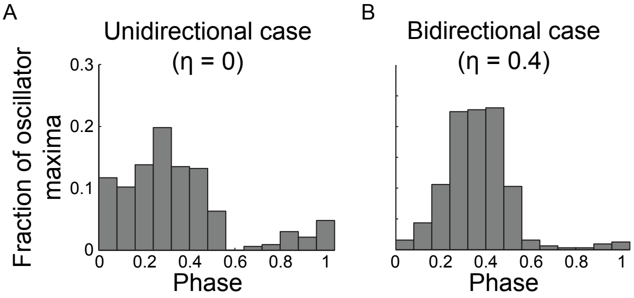

Figure 3.14: Simulated phase shift for the unidirectional and bidirectional strains. Histograms of the activator concentration maxima within the cell cycle phase. As in the other phase shift histograms, the x-axis has been redefined so that the initiation of the cell cycle starts at 0.6 and finishes at 0.5. A) The unidirectional strain is considered without coupling from the synthetic oscillator to the chromosome replication. In the model this is translated as an $\eta = 0$ ($n = 333$). B) The bidirectional strain contains a back-coupling from the synthetic oscillator to the chromosome replication ($\eta = 0.4$, $n = 321$).

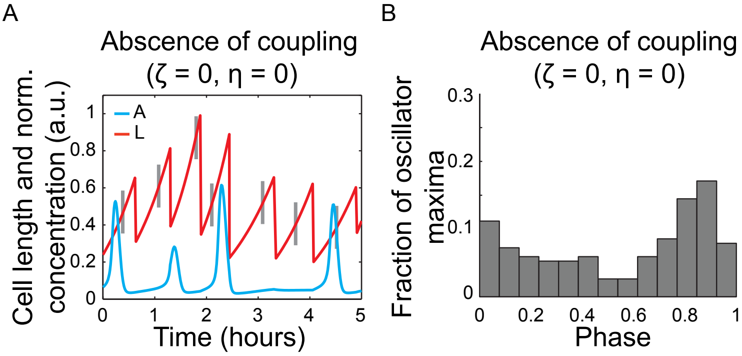

Figure 3.15: Simulated time series and the phase shift between the synthetic and cell-cycle oscillators in absence of coupling. We have considered the hypothetical case in which the synthetic oscillator is not driven by the bacterial cell cycle, nor back-coupled to replication. A) Time series for cell length (L), in red, and the normalized concentration of the activator (A), in blue, are plotted. In every cell cycle, the replication threshold R_{thr} is indicated as a vertical gray bar, between consecutive divisions. The periods for the cell length and synthetic oscillators are 43 ± 13 min and 100 ± 50 min, respectively. B) Histogram of the timing of activator concentration maxima within a cell length cycle ($n = 152$). As in Section 3.4, the phase has been redefined so that 0.5 corresponds to the cell division (maximal length of the cell cycle).

3.7 Deletion of *hda* from the bacterial genome

In order to eliminate the basal production of the RIDA system from the bacterial genome, we constructed a new strain, lacking the natural *hda* gene (Δhda) from the chromosome. In this mutant, the inhibitory control of the initiation of chromosomal replication through the Hda production exclusively depends on the synthetic oscillator. Fig. 3.16 shows preliminary results of the phase shift between the oscillator maxima and the cell cycle in the Δhda strain, which compared to Fig. 3.8B seems to have a higher co-entrainment between the two oscillators. Additional experiments and computational analysis are required to understand the increase in the back-coupling for this strain.

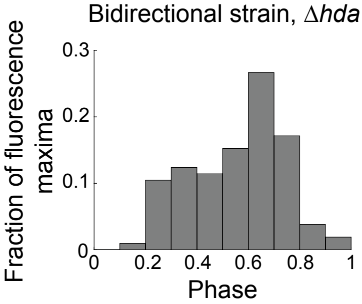

Figure 3.16: Phase shift between the oscillator maxima and the cell cycle in the Δ*hda* strain. Distribution of the oscillator maxima within the cell cycle in the case of the bidirectional strain in the context of the Δhda strain.

3.8 Discussion

The results shown in this Chapter show that the unidirectional coupling from the cell cycle to the synthetic oscillator leads at best to partial coordination of the two cellular rhythms, as measured by the level of phase synchronization between the oscillators (Fig. 3.8A). These results are not necessarily straightforward, especially given the different nature of our two oscillators. When coupling two different oscillators, the efficiency of the unidirectional driving depends, in principle, on which oscillator is the driver and which one is the receiver. When the natural frequencies of the two oscillators are not close to each other, the unidirectional driving may not be necessarily worse than the mutual coupling. We show, however, that this is indeed the case: bidirectional coupling is needed in our case to cause a significant level of co-entrainment.

There are different explanations for results of the weak entrainment from the cell cycle to the synthetic oscillator. The first one is that the synthetic oscillator resides in two plasmids, instead of in the chromosome. In this situation, the copy number of the genes of the synthetic oscillator does not change following directly the chromosome replication cycle. Furthermore, the plasmids that contain the oscillator have *relaxed* origins of replication (colE1 and p15A), which means that the doubling of the genes contained in these plasmids are independent on the regulation of the replication. For this reason, we expect that the cell cycle and this gene-based circuit are coupled through an intrinsic, passive mode, since the expression levels of the circuit components oscillate periodically following the chromosome replication cycle of the cell. By any means, it would be expected to find a stronger coupling by the integration of the synthetic oscillator into the bacterial chromosome.

Another possible explanation for the weak entrainment could be related to the observation that even under minimal growth conditions, bacterial cells can start more than one round of replication per cycle. In this case, instead of having a discrete change on the gene-number and recuperation after cell division, cells are gradually changing their amount of DNA, so it reduces the possible effect due to smaller relative changes in gene expression. As it was observed in Mori et al., cells undergoing several replications of the chromosome can buffer the effect of the cell cycle upon other oscillators in the cell. In contrast, in eukaryotic cells, such a buffering does not occur, because the timing and number of replications are restricted to mitosis. In addition, in eukaryotes there is a period of transcription silencing during mitosis that can produce a more significant effect on the expression of components of the circadian clock (Gottesfeld and Forbes, 1997). These observations suggest that the driving from the cell cycle to the circadian rhythm could be larger in eukaryotic cells.

Additionally, our results are potentially relevant for the design of robust synthetic oscillators, by showing that the inclusion of components that couple oscillators with the chromosome replication machinery alters their rhythm and tightens the phase distribution, through synchronization to the cell cycle.

3.9 Appendix

3.9.1 Experimental methods

Strains and plasmids construction

Standard protocols of Molecular Biology were used for the construction of the different plasmids (for details see Methods 2 and Annex 7). Plasmids were replicated in DH5α *Escherichia coli*. The strain used in all experiments is JS001, which has *araC* and *lacI* genes deleted, to avoid interactions with the synthetic circuit. All transformations were performed with standard chemical or electrical protocols. The resulting constructs were confirmed by PCR and sequencing.

The original strain JS011 (A kind gift from Prof. J. Hasty, University of California San Diego) was obtained by the transformation of the plasmids pJS167 and pJS169 into JS001. The first plasmid harbors the $\mathrm{P}_{lac/ara}$-araC-ssr-T1 and $\mathrm{P}_{lac/ara}$-gfp-ssr-T1, and the second one contains $\mathrm{P}_{lac/ara}$-lacI-ssr-T1.

The plasmid pMiL_{001} was then constructed *de novo* by assembling the origin of replication pSC101 from plasmid pZS2-123 and the gene for spectinomycin resistance, amplified from the commercial plasmid pCDFDuet1 (Fig. 3.17). The constructed plasmid was transformed into the original strain JS011 to generate the unidirectional strain. Plasmid pMiL_{101} was constructed cloning the promoter from $P_{lac/ara}$ in the PJS169, *hda*, and *dnaN* from the genome of *E. coli* MG1655, and the transcriptional terminator T1 from the plasmid pCDFDuet1. The plasmid was then transformed into JS011 to create the bidirectional strain.

Primers with 5'-phosphates were used to amplify the original plasmids and religate them, so as to eliminate the *araC* and *lacI* degradation tags. All primers are listed in table 3.1.

Media and growth conditions

For overnight liquid cultures, cells were grown at 37°C in Luria Broth (LB, Miller's modification) in an incubator with shaking. When it was necessary, antibiotics for selection were added in their corresponding final concentrations (100 μg ml^{-1} ampicillin, 50 μg ml^{-1} kanamycin, and 50 μg ml^{-1} spectinomycin). The next day, the culture was diluted to a final OD_{600} of 0.02 in 5ml of LB with the necessary antibiotics and inductors:

Table 3.1: Primers for the pMiL001 and pMiL101 construction.

Porpuse	Name primer	Sequence
Gibson Assemb.	MD158	AGTACTGCATGCAGCGTAGCGTGTGTGGAAGTGAGCGGATAACAATT
	MD159	AAACAAATAGCTAGCTCACTCGGTGTCTAGCGGCGGATTTGTCCTACTC
Ampl. plasmid	MD156	TTTGCCGACTACCTTGGTGATCTCG
	MD157	GGTACCCCATGGAGTACTGCATGCAGCGTAGACCGAGTGAGCTAG
Ampl. plasmid	MD94	CCCGGGATTAAAGAGGAGAAAAGGCCTCTACACACCGGCACAGCTCTCTTTG
	MD95	CTTCTGAGCTCAGTTACTACAACTTCAGAATCTTTCACAAACGGAATGGTC
Gibson assemb.	MD96	CTGATGAGCTCTACCCGGGATTAAAGAGGAGAAAAGGCCTATGAAATTTACCGTAGAACGTGAGCATTTATTAAAACCGCTAC
	MD97	CTCTAGATTAATTAATTAAGCGGCCGCGAATTAACAACACTATTACAGTCTCATTGGCATCAACATAAGCCGCGCTC
Gibson assemb.	MD129	CTGATGAGCTCTAGAACTAGTACACAATCGGCATGCTGTTGTTAAGCTTCGCGGCCGCTTTTAATTAATC
	MD99	CTTCTCTGCAGTAGTCTAGGGCGGCGGATTTCCTACTC
Δ degr. tags	MD168	5’Pho-TAATGAAAGCTTAATTAGCTGATCTAGCGTG
	MD169	5’Pho-TGACAACTTGACGGCTACATCATTCA
	MD170	5’Pho-CTGCCCGCTTTCCAGTCGGGAAAC

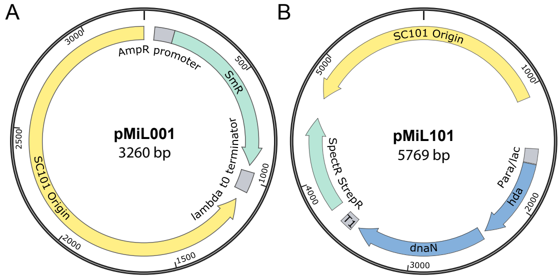

Figure 3.17: Diagrams for the plasmids pMiL001 and pMiL1001. A) The plasmid pMiL001 contains an origin of replication (pSC$_{101}$) and an antibiotic resistance gene (spectinomycin). This plasmid was transformed into the JS011 strain, which contains the original synthetic oscillator, to create the unidirectional strain. B) The plasmid pMiL101 contains the same replication origin and resistance gene than pMiL001, and the construct $P_{lac/ara}$-*hda*-*dnaN*-T1 (responsible for the back-coupling between the synthetic oscillator and the chromosome replication). This plasmid was transformed into the JS011 strain to form the bidirectional strain. The diagram of both plasmids have been generated by SnapGene.

0.7% (w/v) arabinose and 2mM IPTG. The culture was grown at 37°C to a final OD$_{600}$ = 0.2 (approximately 2 hours at 37º and 225 rpm). Cells were then diluted 1:5 in a minimal medium A (see Annex 7.4.1) with inductors. 50 μl of the diluted liquid culture was placed in a 2% (w/v) low-melt agarose pad of minimal media A with inductors and 0.4% (w/v) glucose[2] (See Annex 7.4.1 for more details). The pads with the cells were placed in an incubator at 37°C for 2 hours. Afterwards, the pads were vortexed in 10 ml minimal medium A, and 2.25 μl of the liquid was spotted in a new agarose pad with inductors and glucose. Finally, the pads were placed in a coverslip-bottom Willco dish for imaging.

Time-lapse microscopy

Movies were acquired from single-cells growing in agarose pads by time-lapse fluorescent microscopy in an incubator at 37°C. All experiments were performed on a Nikon TE2000 inverted microscope with a 100x objective. The pictures were taken every 5 min (see Annex 7 for more details).

---

[2] We observed that one part of the population was not presenting oscillations in the GFP signal, maintaining and constant 'on' or 'off' state. We hypothesize that this could be related to a metabolic overload of the cells, due to the presence of three different kind of plasmids inside each cell. To increase the fraction of oscillatory cells we conducted a screening with different concentrations of glucose and we found that at the concentration of 0.4% (w/v) of glucose there was a higher number of oscillatory cells, as well as a more constant period in the oscillations of the system.

3.9.2 Computational methods

Unidirectional model

Stricker et al. proposed a detailed molecular model for their synthetic oscillator consisting of 73 reactions, 27 species, and 27 parameters. The authors explicitly considered intermediate processes such as dimerization of AraC and tetramerization of LacI (Stricker et al., 2008). Due to the difficulty to work with such a complex model, we implemented a low-dimensional model based on minimal mechanisms, inspired by the model from Rué and Garcia-Ojalvo:

$$\frac{dA}{dt} = \alpha_1 + \frac{\beta_1 An}{Kn + A^n + (\gamma R)^p} - \delta_1 A \tag{3.1}$$

$$\frac{dB}{dt} = \alpha_2 + \frac{\beta_2 A^n}{Kn + A^n + (\gamma R)^p} - \delta_2 R \tag{3.2}$$

Here A is the activator (AraC dimers), and R is the repressor (LacI tetramers). Given that the same promoter controls all the synthetic oscillator elements, ($P_{lac/ara}$), K, n, p, and γ are the same for both species. A scheme depicting the model interactions is shown in Fig. 3.9. These ODEs are used later in the coupled oscillator model (see Eqs. 3.6 and 3.7).

This system presents a limit cycle for the parameter values shown in Table 3.2. Note that we assume a non-zero basal production rate because the limit cycle disappears when $\alpha_1 = 0$. In this regard, experiments show that when the synthetic oscillator is not induced, part of the population turns the reporter's expression on, thus demonstrating that the hybrid promoter $P_{lac/ara}$ is leaky.

The degradation rate of R (δ_2) is assumed to be one order of magnitude smaller than the one of A (δ_1) which can be explained as follows. In the experimental implementation of the oscillator, AraC and LacI are marked with a *ssrA* degradation tag. This tag is recognized by ClpXP, a proteolytic complex composed of ClpX (responsible for unfolding the protein to be degraded) and ClpP (a peptidase) (Baker and Sauer, 2012). This tag is also recognized by ClpAP, which analogously to ClpPX is composed of a chaperone (ClpA) and also by the ClpP peptidase (Sharma et al., 2005). When ClpAP finds a homodimer (which happens when the two promoters – the subunits that constitute an oligomeric protein – have the *ssrA* degradation tag, as it is our case) the most probable scenario is that ClpAP degrades the two subunits at the same time (Sharma et al., 2005).

Table 3.2: Parameter values for the computational model.

Par	Value	Units	Description
α_1	5.1	nM s^{-1}	A basal production rate
α_2	0.75	nM s^{-1}	R basal production rate
α_3	0.5	nM s^{-1}	B basal production rate
β_1	225	nM s^{-1}	A maximum activated production
β_2	30	nM s^{-1}	R maximum activated production
β_3	10	nM s^{-1}	B maximum activated production
δ_1	0.01158	s^{-1}	A degradation rate
δ_2	0.001158	s^{-1}	R degradation rate
δ_3	0.00025	s^{-1}	B degradation rate
γ	2	–	Ratio of activation to inhibition threshold
K	5000		Concentration of A for half-maximum activation
n	2	–	Activation cooperativity (Hill coefficient)
P	2	–	Inhibition cooperativity
L_0	0.5	a.u.	Initial cell length (when the cell is born)
τ	30	min	Characteristic time of the cell growth, integrate & fire model
K_1	100	nM	Concentration of B for half-maximal back--coupling
ε	0.75	–	Replication threshold
D_{thr}	$2L_0$	a.u.	Division threshold

It is also probable that ClpXP behaves in the same way. However, there is no evidence in the literature that ClpAP, ClpXP, or both may degrade a whole tetrameric complex at once. Studies measuring the size of the pore that allows the substrate to reach the active site of ClpP show that this pore would be large enough to accommodate between two and three polypeptidic chains simultaneously (Burton et al., 2001). Besides, kinetic experiments with the ClpXP machinery indicate that the denaturalization process determines the degradation rate (Kim et al., 2000). Hence, it seems reasonable that LacI tetramers (R) degrade more slowly than AraC dimers (A). Then, we consider to have a pool of a protein that assembles in homotetramers, and assuming that degradation only occurs enzymatically, we have:

$$\frac{dD}{dt} = -k_+D^2 + \delta_T CT - \delta_D CD \tag{3.3}$$

$$\frac{dT}{dt} = k_+D^2 - \delta_T CT \tag{3.4}$$

where D denotes the dimeric conformation, T denotes the tetrameric form and C corresponds to the protease concentration. If we assume that D is in the quasi-steady state, we obtain:

$$\frac{dT}{dt} = \frac{(\delta_D C)^2}{2k_+} - \frac{\delta_D C}{2k_+}\sqrt{(\delta_D C)^2 + 4k_+ CT} \tag{3.5}$$

Given the assumption in k_+, from the previous expression, we have that T degrades as $\sim T^{1/2}$. Since in the model Eqs. 3.1 and 3.2 we consider only linear degradations, we take this fact into account by assuming a smaller degradation rate for R (LacI tetramers) compared to A degradation rate (AraC dimers). The Hill coefficients in the synthetic oscillator model, defined by parameters n and p are both equal to 2 and account for changes in DNA conformation. Regarding n, the regulation of P_{ara} by AraC is implemented in a positive form (in the presence of arabinose) and a negative one (in the absence of arabinose) involving DNA looping (Lobell and Schleif, 1990). Regarding p, the repression of P_{lac} also relies on a DNA looping conformation effect (Lewis et al., 1996).

Bidirectional model

As we mentioned in the Section 3.6, we developed a reduced model based on an activator-repressor system (Eq. 3.6, for the activator and Eq. 3.7 for the inhibitor) where the RIDA system (B), which is also controlled by the hybrid promoter, $P_{lac/ara}$, is given by Eq. (3.8). This model allows us to produce a back-coupling between the synthetic oscillator and the cell cycle through the inhibition of the initiation of the chromosome replication. We have seen that the cell cycle can be modeled as an integrate and fire mechanism, in which the cell length grows exponentially (Eq. 3.9) and two thresholds trigger chromosomal replication and cell division events. In this way, when the cell length reaches the first threshold (replication, R_{thr}), the productions of all the synthetic oscillator elements are doubled (as 2-fold increases the copy number of genes) (Eq. 3.10). B is assumed to increase the threshold R_{thr}, in a way that mimics its inhibitory effect on replication (Eq. 3.11). Once the cell length arrives at the second threshold (division, D_{thr}), it returns to its initial value L_0, and the production rates are reset to their original values. The full model is:

$$\frac{dA}{dt} = \alpha_1\zeta + \frac{\beta_1\zeta A^n}{K^n + A^n + (\gamma R)^p} - \delta_1 A \tag{3.6}$$

$$\frac{dR}{dt} = \alpha_2\zeta + \frac{\beta_2\zeta A^n}{K^n + A^n + (\gamma R)^p} - \delta_2 A \tag{3.7}$$

$$\frac{dB}{dt} = \alpha_3\zeta + \frac{\beta_3\zeta A^n}{K^n + A^n + (\gamma R)^p} - \delta_3 A \tag{3.8}$$

$$\frac{dL}{dt} = \alpha_0 L \tag{3.9}$$

where $\alpha_0 = L_0/\tau$ (with τ being the characteristic time of the cell cycle). ζ is a parameter that reflects the driving of the synthetic oscillator by chromosomal replication:

$$\zeta = \begin{cases} 1 & \text{for } L_0 \leq L < R_{thr} \\ 2 & \text{for } R_{thr} \leq L < D_{thr} \end{cases} \tag{3.10}$$

As mentioned above, B mediates the coupling of the synthetic oscillator to the chromosomal replication, by increasing the replication threshold:

$$R_{thr} = D_{thr}.(\varepsilon + \frac{\eta\kappa B}{B + K_1}) \tag{3.11}$$

Here $\varepsilon \ \epsilon$ (0,1) is the fraction of the division threshold at which replication occurs when the synthetic oscillator is not back-coupled to replication ($\eta = 0$). We can observe that when back-coupling is introduced ($0 < \eta \leq 1$), R_{thr} increases and approaches to D_{thr} (Fig. 3.11). As the term $B/(B+K_1)$ saturates to 1, the maximum limit where replication can occur (considering the strongest back-coupling, $\eta = 1$) is $R_{thr} = D_{thr}(\varepsilon + \kappa)$. We chose $\kappa = 0.9(1 - \varepsilon)$ because it is not biologically realistic that replication coincides with cell division. Note that since all our exogenous genes are controlled by the same promoter ($P_{lac/ara}$), we consider the parameters K, n, p, and γ to be the same for species A, R, and B.

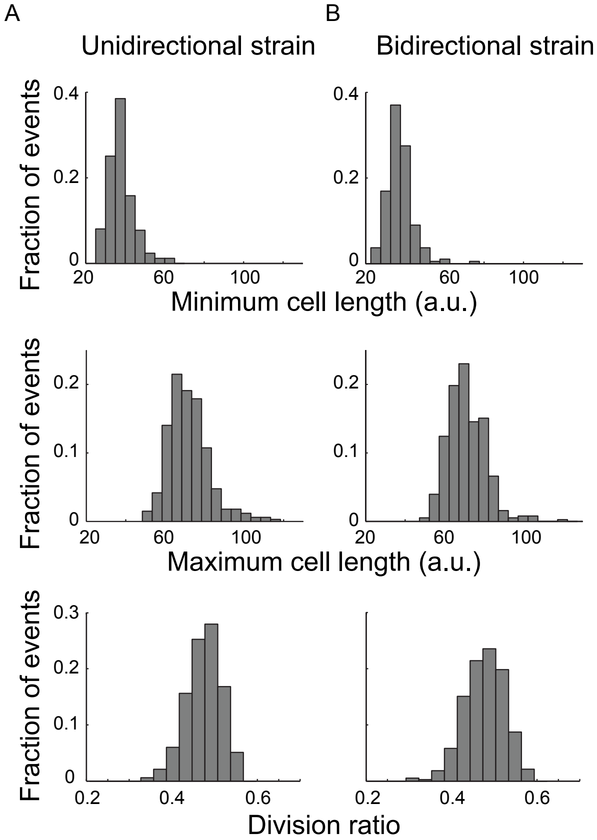

Figure 3.18: Experimental distributions for minimal and maximal cell length, and the division ratio between. A) Unidirectional strain: Top panel - Cell length at the initiation of the cell cycle (newborn cell), $\langle L_{min} \rangle = 38 \pm 7$ a.u., Medium panel - cell length at the end of the cell cycle (before cell division), $\langle L_{max} \rangle = 72 \pm 11$ a.u., Bottom panel - cell division ratio distribution (defined as $\rho = (L_{max} - L_{min})/L_{max}$), $\langle \rho \rangle = 0.47 \pm 0.05$ a.u. B) The same distributions are plotted for the bidirectional strain: $\langle L_{min} \rangle = 37 \pm 7$ a.u., $\langle L_{max} \rangle = 71 \pm 10$ a.u. and $\langle \rho \rangle = 0.47 \pm 0.06$ a.u.

We introduced variability in the deterministic model described above by allowing random variation in the reaction rates among the different cell cycles. To that end, for each cell cycle we drew parameter values randomly from a Gaussian distribution with mean values shown in Table 3.2 and standard deviations ranging from 2% of the mean value in the case of the synthetic oscillator parameters (Eqs. 3.6 and 3.7) up to 18% in the case of initial cell length L_0. These ranges were adjusted such that the statistical distributions of different oscillator features were in agreement with experimental results. In particular, Fig. 3.18 shows that experimental distributions of the lengths of newborn cells (top row) have a width of ~18% for both the unidirectional and the bidirectional strains. In turn, the division ratio (bottom row) has a width of 11%. Also, given that the maximum cell length distributions do not change (middle row), we assumed that back-coupling only affected the replication threshold (by incrementing its value and approaching it to the division threshold, as explained above) and we left the division threshold unchanged.

Chapter 4

Regulation of biomass production by ion flux modulation

The proliferation of a bacterial population under stress depends on the different strategies that cells can adapt to cope with the unfavorable conditions. Commonly, bacterial survival upon antibiotic treatments is associated with mutations that confer resistance, or to non-growing cellular states that allow cells to tolerate the stress (Lewis, 2007; Wood et al., 2013; Maisonneuve and Gerdes, 2014). A well-studied example is the phenomenon of persister cells, a phenotype with a transient dormant state (Balaban et al., 2004; Gefen et al., 2008; Wood et al., 2013; Maisonneuve and Gerdes, 2014). The low metabolism of this cellular state makes cells tolerant to the antibiotic due to the low activity of the target molecule. Indeed, studies in persister cells have shown that one way in which a bacterial population can tolerate antibiotic treatments is by down-regulating the antibiotic target. On the other hand, there are no clear examples of how rapidly growing cells could increase their tolerance to antibiotics. In this Chapter, we use analysis of single-cell dynamics and proteomics to present a new mechanism whereby growing *Bacillus subtilis* cells increase their tolerance to ribosome-targeting antibiotics, on ion flux modulation.

This Chapter has been done in collaboration with the laboratory of Dr. Gürol Süel (University of California San Diego, UCSD). The proteomics data was obtained in the laboratory of Dr. Steven P. Briggs (UCSD). The mathematical model has been developed by Dr. Jordi Garcia Ojalvo.

4.1 Heterogeneity in the tolerance to antibiotic stress

As explained in the Introduction 1.5, bacterial cells present different strategies to cope with stress (Eldar and Elowitz, 2010; Balázsi et al., 2011; Geiler-Samerotte et al., 2013; Stecchini et al., 2013; Reyes and Lahav, 2018). Nowadays, it is known that even in isogenic bacterial populations there is cell-to-cell variability in the stress response, which can be associated for example to the sensitivity to antibiotics. This variability in the stress response is well captured in the classical picture provided by the antibiotic dose-response curve, shown in Fig. 4.1. This well-known behavior shows that at high antibiotic concentrations the drug eliminates all bacterial cells, while in subinhibitory concentrations there is a reduction of the population, but there are still some cells that survive. In that sense, the gradual progression of the curve indicates that cell-to-cell variability in the stress response can lead to the appearance of certain cells capable of tolerating the unfavorable conditions. The growth of the adapted cells will increase the probability of the populations to explore new stress responses and eventually gain resistance (Levin-Reisman et al., 2017). It is essential then to study the response of single-cells to antibiotic exposure in order to comprehend the mechanisms that allow cells to increase their tolerance to antibiotics.

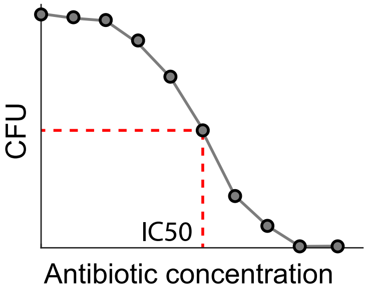

Figure 4.1: Cartoon of a standard antibiotic dose-response curve. Example of the typical sigmoidal dose-response curve where the number of Colony Forming Units (CFU) is plotted as a function of the antibiotic concentration. IC50 indicates the point where half of the population survive, with its corresponding antibiotic concentration. Notice that for the highest antibiotic concentrations, all the population is killed, indicating that this strain is not resistant to the antibiotic.

In this Chapter, we investigate whether individual cells for the undomesticated *Bacillus subtilis* differ in their modulation of ion flux, and how the resulting variability in ion content plays a role in the puzzling tolerance of bacteria against stress conditions, in particular, induced by ribosome-targeting antibiotics.

4.2 Role of ions in the bacterial stress response

Inorganic ions play several essential roles in all kinds of cells, such as macromolecule stabilization, electrical communication, enzymatic activity (by acting as cofactors), and signaling (Petukh and Alexov, 2014). The types of ions used by cells is very diverse, and their concentrations are regulated according to the cellular function that the specific ion does (Harold, 1977). This regulation is important because ions can also be toxic at high intracellular concentrations (Banks et al., 2010; Hohle and O'Brian, 2014). For example, bacteria keep a tight control of calcium ions (whose intracellular concentration is on the order of 0.1 μM) despite being used for important processes, such as cell division, motility, and sporulation, bacteria keep tight control of calcium (on the order of 0.1 μM) because of its toxicity in higher concentrations (Gangola and Rosen, 1987). In contrast, magnesium is the most abundant divalent ion inside bacteria (around 20 mM) (Romani, 2011), where it is bound to a variety of macromolecules, including ribosomes (Klein, 2004), to which it provides stability. There is thus a strong regulation of the different ion concentrations, which can be modulated by cells depending on the different requirements. In spite of its importance, studying the modulation of the ionic content in cells requires measuring the ion flux across the membrane. Due to the challenges of measuring the dynamics of specific ions in single-cell bacteria, other approaches should be used for this kind of studies.

A new approach is suggested by the fact that inorganic ions are a key determinant of the overall membrane potential of the cell. Thus, membrane potential can be used as a proxy of the total ion flux in the cell. Indeed, some bacterial stress responses have been recently identified through measurement of the cellular membrane potential. For example, monitoring membrane potential dynamics in *Escherichia coli* cells has shown that application of mechanical stress (in the form of pressure) increases intracellular calcium levels (Bruni et al., 2017). Furthermore, *B. subtilis* cells within biofilms collectively increase their fitness through potassium ion channel-mediated electrical signaling that enables long-range coordination of metabolic states among cells (Liu et al., 2015; Prindle et al., 2015; Humphries et al., 2017; Larkin et al., 2018; Martinez-Corral et al., 2018). These studies indicate that bacteria modulate the ion flux in response to stress, resulting in changes in the membrane potential.

4.3 Ions as part of the ribosomal structure

Ribosomes are the responsible for protein (and thus biomass) production in the cell. Due to their relevance, several antibiotics target this macromolecule to prevent cellular proliferation and induce cellular death. Bacteria contain in between 5000 to 100000 ribosomes per cell, and, for example, the mass of ribosomes for rapidly-growing cells can represent up to 40%-50% of the cell mass (Milo et al., 2010; Chen et al., 2012; Bosdriesz et al., 2015). The number of ribosomes, as we saw in the Introduction 1.3, varies in relation to the growth rate.

The bacterial ribosome contains ∼170 ions which neutralize the negative charges from the RNA and proteins that constitute the backbone of the macromolecule (Fig. 4.2A) (Schuwirth, 2005). So, ions are essential for the stability and the compaction of the structure. Given that ribosomes are essential for cell proliferation, and that their stability (and thus their functionality), depends on the ion content, we investigate in this Chapter whether bacteria may modulate their ion flux to cope with ribosomal stress(Fig. 4.2B).

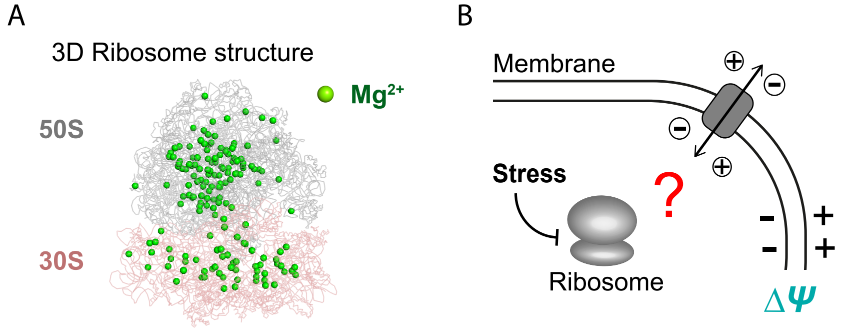

Figure 4.2: Ion modulation as a ribosomal stress response. A) Scheme of the 3D structure of the ribosome specifying the locations of magnesium ions. The sequence is from Protein Data Bank (PDB, ID: 4v4q), and the 3D structure was generated using Pymol. B) Cartoon illustrating the question of whether cells, under ribosomal stress, modulate ion content as a stress response. The circles represent ions.

4.4 Membrane potential under ribosomal stress

All cells are enclosed by a membrane, which acts as an insulator creating a difference of ions and charged molecules between the interior and the exterior of the cell. This difference of charges creates an electric potential, known as *membrane potential*, which in mathematical terms is defined as:

$$V_m = V_{in} - V_{out}, \tag{4.1}$$

where V_{in} and V_{out} are the potentials inside and outside of the cell, respectively. If the cell is at rest, the value of the membrane potential is known as *resting potential*, and in bacteria is around −150 mV. If this value goes closer to zero, it is said that the cell *depolarizes.* On the contrary, if the cell becomes more negative *hyperpolarizes.*

To investigate ion flux in bacteria under ribosomal stress, we quantitatively measured the membrane potential of individual *Bacillus subtilis* cells. Specifically, bacteria were grown in minimal defined media (MSgg) inside a microfluidic device (Fig. 4.3A) that provides control over growth media conditions and enables imaging of individual cells (Fig. 4.3B, left). We measured membrane potential using a previously characterized fluorescent membrane potential indicator dye, Thioflavin-T (ThT) (Fig. 4.3B, right) (Prindle et al., 2015). The addition of Carbonyl cyanide m-chlorophenyl hydrazone (CCCP) (Figs. 4.3C and 4.23), a protonophore that dissipates membrane potential, shows that cells with more positive membrane potential exhibit a lower fluorescence signal.

We used first this experimental approach to determine the distribution of membrane potential of our bacteria in the absence of stress. We find that even when no stress is applied, a small percentage ($3 \pm 0.03\%$, mean±95% CI, $n = 1.4x10^6$) of cells exhibit hyperpolarized membrane potential (Figs. 4.4A,B, top panels). Given that the membrane potential directly depends on ion flux, we confirmed that the fraction of hyperpolarized cells increases by removing extracellular cations in the growth media, which promotes their efflux. As expected, the fraction of bacteria with a higher membrane potential increases (by fifteen-fold) when multi-valent cations are removed from the growth media (Figs. 4.4A,B, middle panels). Therefore, perturbing the flux of ions across the cell membrane changes the electrochemical membrane potential and can be quantified by imaging the ThT dye.

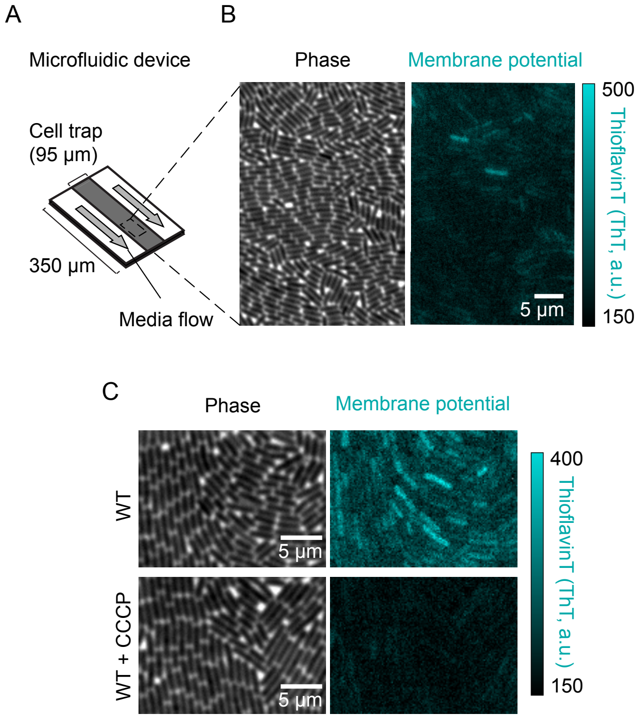

Figure 4.3: Setup of the experimental approach for the measurement of single-cell membrane potential. A) Schematic of the microfluidic device used in this study. B) Snapshots of bacterial cells in phase contrast (left panel) and the corresponding fluorescence image (right panel). The fluorescent dye Thioflavin-T (ThT, in cyan) reports on the membrane potential. C) Snapshots of wild-type cells (top row) in phase (left) and fluorescence (right). The bottom row shows snapshots for WT with CCCP. Notice the low ThT signal, showing the dissipation of the membrane potential.

We then focused on the question of whether membrane potential, and thus ion flux, are modulated during stress. To address this question, we measured the membrane potential in the presence of the antibiotic spectinomycin, which targets the 30S subunit of ribosomes (Davis, 1987; Carter et al., 2000). We used sub-lethal concentrations of this antibiotic (2 mg/L) since our goal is not to kill the cells, but just perturb their ribosomal function. We find that spectinomycin addition increases the fraction of cells that exhibit hyperpolarization by approximately thirteen-fold, compared to the antibiotic-free case (Figs. 4.4A,B, bottom panels). Hence, exposing bacteria to sub-lethal concentrations of spectinomycin increases the likelihood that they exhibit a more negative membrane potential.

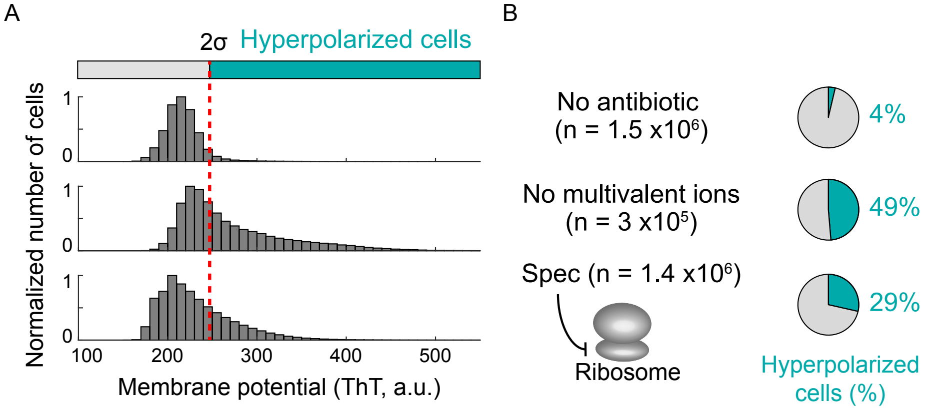

Figure 4.4: The distribution of ThT intensities shows a fraction of hyperpolarized cells in basal conditions. A) Distribution of ThT signal in a population of cells (top row), in the absence of ions in the media (middle row), and in the presence of spectinomycin (a ribosome-targeting antibiotic). The red-dashed line indicates two standard deviations from the mode of WT cells in minimal media (top row), which we used as a cutoff to determine the fraction of hyperpolarized cells. B) Pie charts showing the statistics from (A), with the percentage of cells exhibiting hyperpolarization in all conditions. The hyperpolarized cell fraction is shown in cyan color.

4.5 Modeling of the ion flux and the membrane potential dynamics

The lipid bilayer that surrounds the cell has a low permeability to charged molecules, including ions. For the maintenance of the correct content for each ion and the conservation of the membrane potential, it is necessary for the cells to exchange ions between the inside and outside. Bacteria use different proteins in the membrane to modulate ion flux. Besides the transporters that pump ions in and out at the expense of energy consumption, there are also ion channels that are usually highly specific for a given type of ion, and allow free flow of those ions through the membrane when the system is not in electrochemical equilibrium.

In general, the flux of ions across the channels is determined by the concentration of the ion itself, as well as by the electric potential across the membrane. Let us assume that the membrane has channels only for a given ion, for example, K^+. The concentration of this ion is higher in the interior of the cell, compared to the exterior. If the corresponding ion channel is open, the ion will leave the cell, hyperpolarizing the cell. As a consequence, the increase of negative charge in the cell's interior will prevent the continuing efflux of K$^+$, reaching an equilibrium where the electrical and the chemical forces are compensated. The value of the membrane potential at which the ion is in equilibrium is known as the *Nernst* or *reversal potential*, and it is defined as:

$$E_K = -\frac{RT}{zF} ln \frac{K^+_{in}}{K^+_{out}}, \tag{4.2}$$

where E_K is the Nernst potential of K$^+$, R is the gas constant (8.314 J.mol^{-1}.K^{-1}), T the temperature in Kelvin, z is the valence of K$^+$, F is Faraday's constant (96.485.10^3 C.mol^{-1}), and K^+_{in} and K^+_{out} are the concentrations of K$^+$ inside and outside the cell, respectively.

Given that the membrane is impermeable to ions, we can interpret the cellular membrane as a capacitor, which stores electrical charges in the interior of the cell producing a difference of potential. Thanks to this approach, we can describe the membrane potential by basic equivalences with electrical circuits (Fig. 4.5). Then, the description for the current across the lipid bilayer (I_c) is the following:

$$I_c = C_m \frac{dV}{dt}, \tag{4.3}$$

which contains the membrane capacitance (C_m) and the rate of change of membrane potential (V_m) with respect to time. In Fig. 4.5, apart from the membrane capacitance, we have also a voltage-gated channel for a given ion, represented by a resistor. This channel allows the flux of an electrical current, and this one, following Ohm's law, is modeled as:

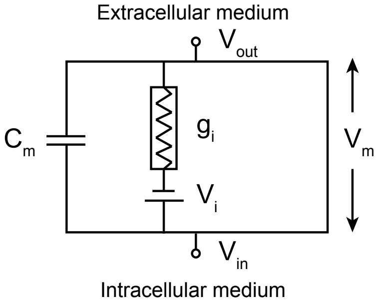

Figure 4.5: Scheme of a simplified electrical equivalent circuit. The membrane potential, here represented as a capacitor, presents the membrane capacitance (Cm) and one ion channel as an example of a resistor. Notice that this example corresponds for an ion that is accumulated in the interior of the cell.

$$I_i = g_i(V_m - V_i) \tag{4.4}$$

Then, the electrical current depends on the channel conductance for the given ion (g_i), and difference between the membrane potential (V_m) and the Nernst potential of the ion (V_i). If V_m is equal to V_i, then the current passing through the ion channel is zero. If we want to consider other ion channels we can add them as other resistors in parallel.

In 1952, Hodgkin and Huxley developed a mathematical model to describe the movement of ions across the membrane of a squid giant axon during an action potential (Hodgkin and Huxley, 1952). This model provides a basic understanding of how voltage-gated ion channels can propagate action potentials and ion channel kinetics. The model incorporates the capacitance (described before) and three currents: sodium, potassium, and leakage. As we saw before, each ion current can be determined by a driving force, represented by a voltage difference and a permeability coefficient, related to the conductance of the specific ion channel.

$$I_{Na} = g_{Na}(V_m - V_{Na}) \tag{4.5}$$

$$I_K = g_K(V_m - V_K) \tag{4.6}$$

$$I_L = g_L(V_m - V_L) \tag{4.7}$$

The leakage term I_L accounts for other ions and molecules that affect the membrane potential, usually associated with chloride or calcium. In general, this channel is considered to allow some *ion leakage* through non-gated channels. Because this term is independent on the membrane potential, the leak conductance (g_L) is constant. On the other side, the channels for K^+ and Na^+ are gated-channels, so their conductances change in response to membrane potential that determines the opened or closed position of the channel.

Altogether, we obtain the equation:

$$C_m \frac{dV}{dt} = -g_K(V_m - V_K) - g_{Na}(V_m - E_{Na}) - g_L(V_m - E_L) \tag{4.8}$$

4.5.1 Cation flux modulation as the mechanism for the hyperpolarization

Here, we develop a mathematical model to describe the relationship between ion flux modulation and the membrane potential dynamics inspired on the Hodgkin-Huxley framework (Fig. 4.6A). The model considers the movement of cations, since the majority of ions in the cell are positively charged (e.g., K^+ and Mg^{2+}), and experimentally we observed an increase in the hyperpolarized cell fraction by the elimination of cations from the media (Fig. 4.4A, bottom).

The model contains two equations, one for the membrane potential and another one for the intracellular concentration of one particular cation (Fig. 4.6A).

$$\frac{dV}{dt} = -g_L(V - V_L) - g_C(V - V_C) + \alpha_{in}C_e - \alpha_{out}C \tag{4.9}$$

$$\frac{dC}{dt} = F\ [-g_C(V - V_C) + \alpha_{in}C_e - \alpha_{out}C] \tag{4.10}$$

The membrane potential equation (Eq. 4.9) takes into account currents from three different elements: a *non-gated channel* (marked in red in Fig. 4.6A) through which cations diffuse between the cytoplasm and the extracellular medium, an *active importer* (in green), whose activity depends on an import rate (α_{in}) and on the external cation concentration (C_e), and an *active exporter* (in purple), whose activity is determined by an export rate (α_{out}) and the cation concentration inside the cell (C). We also consider a leakage current with its corresponding voltage difference ($V - V_L$) and conductance (g_L). This last term accounts for all the other ion species, and their transporters and channels, that determine the membrane potential. On the other side, the equation that describes the intracellular concentration of the cation (Eq. 4.10) also takes into account the three of ion fluxes.

As expected, the model shows that a reduction of cation uptake through the channel reduces the intracellular cation concentration, which corresponds to a hyperpolarization of the cell. But additionally, the model predicts that this hyperpolarization should be transient, rather than permanent (Fig. 4.6B). The transient nature of the hyperpolarization is essentially due to the change in the Nernst potential caused by the modulation of intracellular cation concentration, which over time eliminates the ion flux imbalance that caused the hyperpolarization in the first place. This response takes the form of a *perfect adaptation* (Ferrell, 2016) to changes in the ion flux.

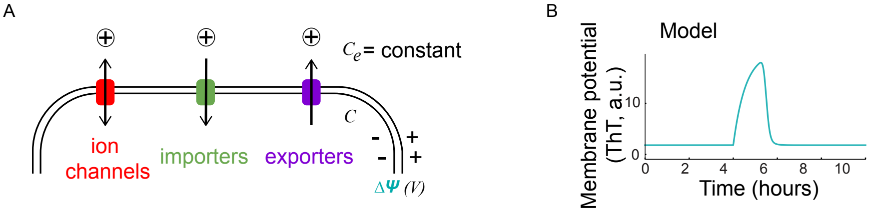

Figure 4.6: Predicted transient hyperpolarization due to a reduction in cation influx. A) Proposed model for relationship between ion flux modulation and membrane potential. Three processes affect the membrane potential through flux of cations (top equation): passive flow through a ion channel (red), active import (green), and active export (purple). These three processes also control the flux of a cation (bottom equation). B) The decrease of the activity of the ion channel produces a drop in the cation influx that produces a transient hyperpolarization.

To test whether the prediction that the hyperpolarization should be transient, we tracked experimentally the membrane potential of single cells over time (Figs. 4.7 and 4.8). We observed that hyperpolarization events were indeed transient, with an average duration of the hyperpolarization of 2.18 ±1.15 hours (Figs. 4.8B,C). Therefore, the experimentally observed dynamic change in the bacterial membrane potential confirms the model prediction, implicating modulation of cation flux as a probable mechanism for cellular hyperpolarization.

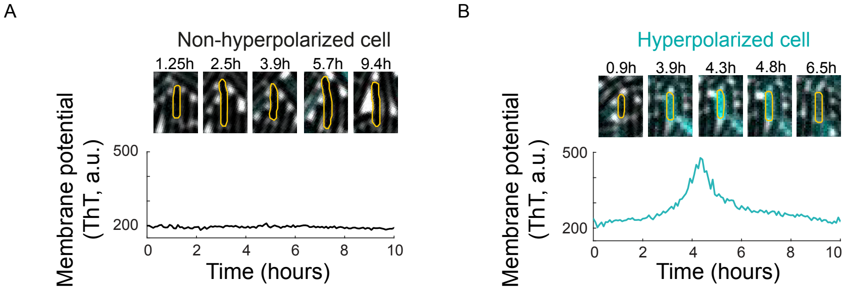

Figure 4.7: Time traces for hyperpolarized cells confirm the model prediction. A) Filmstrip for a representative non-hyperpolarized cell (top), and its corresponding membrane potential (ThT, a.u.) signal as a function of time (bottom). B) Filmstrip for a representative hyperpolarized cell (top), and its corresponding membrane potential as a function of time (bottom).

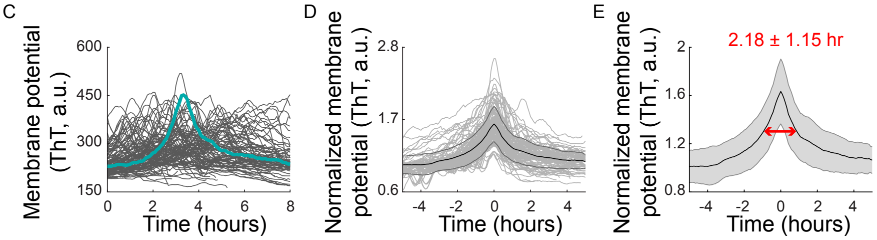

Figure 4.8: Characteristics of the hyperpolarized time traces. A) Time traces of membrane potential (ThT) from hyperpolarized cells ($n = 119$) exposed to sub-lethal concentrations (2 mg/L) of spectinomycin. One single trace is highlighted in cyan. B) Each time trace is normalized by initial ThT value before antibiotic addition, and then, aligned by the peak ThT at time point 0 hr. Mean, and standard deviation are overlaid on top in black lines. C) Mean, and standard deviation from panel B. A red arrow indicate the half-peak duration (mean ± SD, hours).

4.6 Ribosomes and membrane potential dynamics

As we saw before, there is a correlation between the number and the activity of ribosomes with the growth rate of the cell. Then, by measuring the elongation (growth) rate of single cells, we can infer the ribosomal state. By using this approach, we wanted to see if there was a correlation between these two essential components of the cell.

To this purpose, we tracked cells in the presence of spectinomycin as ribosomal stress, and we differentiated two groups: cells with transient hyperpolarization, termed 'Hyperpolarized cells,' and a group without large fluctuations in the membrane potential, termed 'Non-hyperpolarized cells.' Figs. 4.9A,B, show the membrane potential dynamics and the cell length of representative examples for the two groups. The time traces, show already by eye that the non-hyperpolarized cell presents a faster elongation (growth) rate, compared with the hyperpolarized-cell. Indeed, if we calculate the mean elongation rate for the different lineages and determine the maximum membrane potential for each of them, we can observe a negative correlation between the membrane potential and the bacterial growth rate (Fig. 4.9C) (Schaechter et al., 1958; Bosdriesz et al., 2015). Since bacterial growth is directly determined by ribosome activity, our results also indicate that hyperpolarization is negatively correlated with ribosome activity.

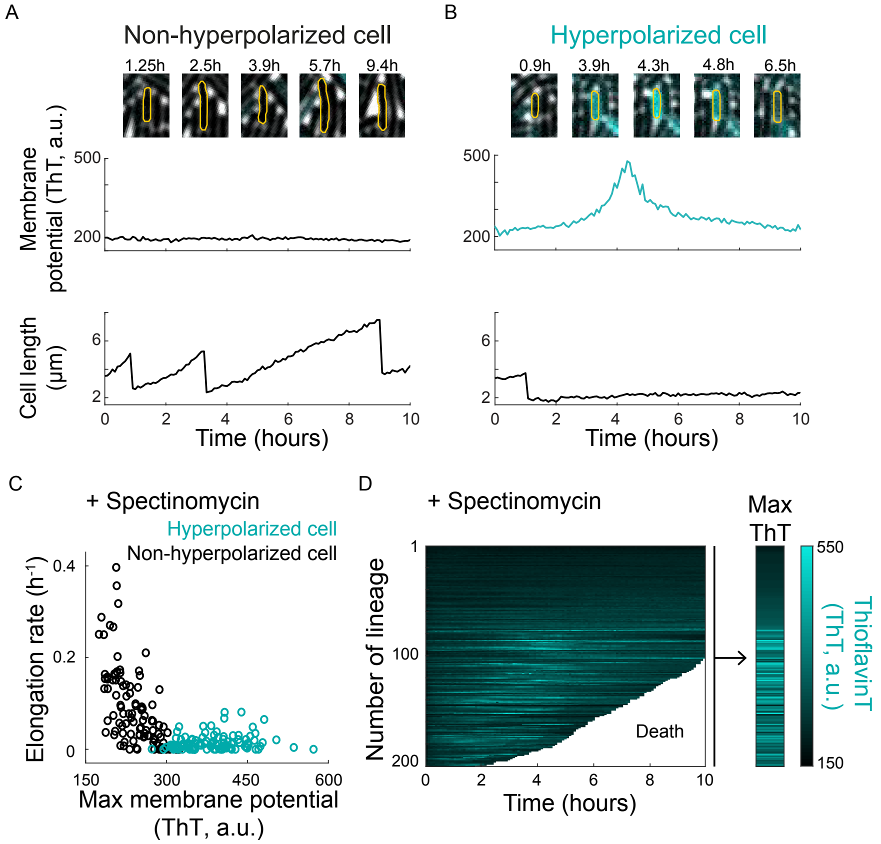

Figure 4.9: Hyperpolarized cells exhibit low elongation rate and high death probability. A) Filmstrip (top) and its corresponding membrane potential as a function of time (bottom) for a representative non-hyperpolarized cell (same as in Fig. 4.6C). B) Filmstrip (top) and its corresponding membrane potential as a function of time (bottom) for a representative hyperpolarized cell (same as in Fig. 4.6D). C) Maximum membrane potential (ThT, a.u.) as a function of elongation rate (h^{-1}) in presence of spectinomycin. Each circle represents one lineage for hyperpolarized cell (cyan, n = 100), or non-hyperpolarized cell (gray, n = 100). Notice the negative correlation between membrane potential and elongation rate. D) Kymograph containing the membrane potential values (ThT, a.u.) for each lineage as a function of time. On the right, projection of the maximum membrane potential (ThT, a.u.) for each lineage. The color bar on the right marks the intensity range of the ThT signal.

Furthermore, we find that hyperpolarized cells have a higher likelihood of dying compared to cells that do not exhibit transient hyperpolarization events (Fig. 4.9D). We find that only 29% of cells that undergo transient hyperpolarization survive, while 84% of cells that do not exhibit hyperpolarization continue to grow (Fig. 4.10). Cells under stress thus display a heterogeneous behavior where one fraction of cells hyperpolarizes and is very likely to die, while the other fraction of cells lacks large fluctuations in membrane potential and continues to grow and survive under antibiotic-induced ribosomal stress.

We also wanted to see if this response was specific for spectinomycin or if other kinds of antibiotics that also target the ribosome would present the same response. Accordingly, we did the same analysis for sub-lethal concentrations of kanamycin (0.5 mg/L), another antibiotic that targets the 30S subunit of ribosomes. Similarly, the fraction of hyperpolarized cells also increases with sub-lethal concentrations of this antibiotic (see Fig. 4.23). Moreover, we observed the same trends in the elongations rate (Fig. 4.11A) and death probability (Figs. 4.10, and 4.11B), in reference to membrane potential dynamics. Hence, in general, chemical stress upon ribosomes produces an increase in the hyperpolarized cell fraction which correlates with the ribosomal activity, and affects the survival of the cell.

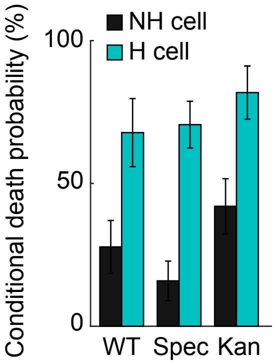

Figure 4.10: Conditional death probabilities. Bar plot for conditional death probabilities for non-hyperpolarized (NH cell, black) and hyperpolarized cells (H cell, cyan) during 10 hours of observation ($n = 90$, $n = 59$, $n = 107$, $n = 119$, $n = 100$, and $n = 66$ from left to right). Error bars represent 95% CI.

4.6.1 Structural perturbations of the ribosomal complex

We have seen that antibiotics that specifically target the ribosome cause changes in the membrane potential that correlates with the cell survival. To determine more directly whether ribosomal stress is the cause of the observed hyperpolarizations, we perturbed the ribosome by genetic modifications that affect the stability of the complex. Specifically, we deleted the ribosomal protein L34 ($\Delta rpmH$, ΔL34), as this deletion was previously

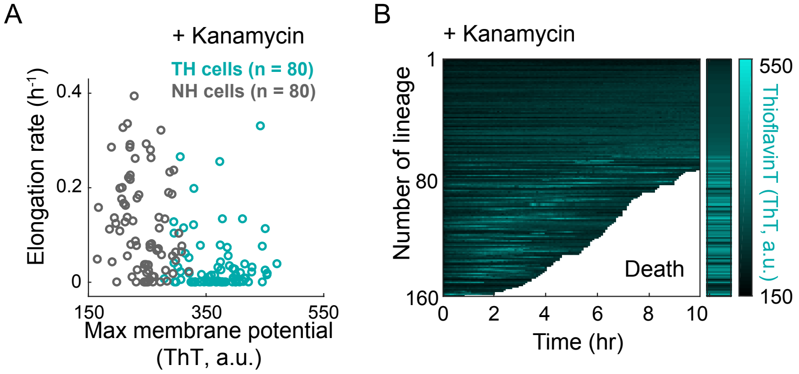

Figure 4.11: Kanamycin presents the same trends than spectinomycin addition. A) Maximum membrane potential (ThT, a.u.) as a function of elongation rate (h^{-1}) in presence of kanamycin (hyperpolarized cells, cyan, $n = 80$; non-hyperpolarized cells, gray, $n = 80$). B) Kymograph for lineages in presence of kanamycin. On the right, projection of the maximum membrane potential (ThT, a.u.) for each lineage.

reported to cause instability of the ribosome (Figs. 4.12A, and 4.22A) (Akanuma et al., 2014). We find that this mutant increases the fraction of hyperpolarized cells (nearly ten-fold), similarly to the increase observed with antibiotic additions (Fig. 4.12B)[1].

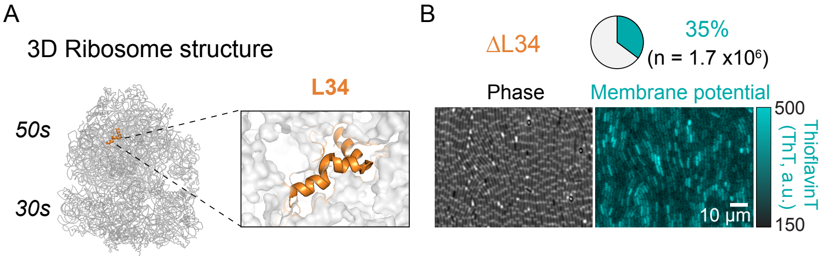

Figure 4.12: ΔL34 mutant increases the fraction of hyperpolarized cells. A) Scheme of the 3D structure of the ribosome showing the location of the ribosomal protein L34. The right panel shows a magnified view of L34 region (in orange). The sequence for the ribosome structure is from Protein Data Bank (PDB, ID: 3j9w), and the 3D ribosomal structure has been generated using Pymol. B) Phase (left) and fluorescence (right) images from the ΔL34 mutant strain. The size and color scale are set at the same scale as in Fig. 4.3B. The pie chart shows the fraction of cells experiencing transient hyperpolarization in a population of 1.7 x 10^6 cells for ΔL34 mutant.

As it was reported before, we also observe a reduction in the growth rate

---

[1] Notice that the experiments performed with L34 deletion mutant are in the absence of antibiotics.

of this mutant compared to wild-type (Fig. 4.13A). These results indicate that ribosomal perturbations that destabilize the structure of the complex increase the hyperpolarized cell fraction, even in the absence of ribosomal-targeting antibiotics. Furthermore, the hyperpolarized cells also present low probability of survival upon ribosomal stress, as we saw in antibiotic addition (Fig. 4.13B).

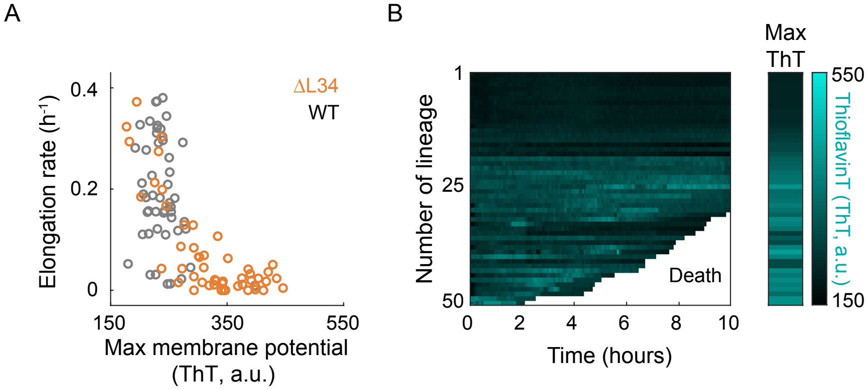

Figure 4.13: ΔL34 mutant presents similar membrane potential dynamics and cellular death than WT in presence of antibiotics. A) Maximum membrane potential (ThT, a.u.) as a function of elongation rate (h^{-1}) for wild-type (gray, $n = 50$) and ΔL34 mutant (orange, $n = 50$). B) Kymograph containing the membrane potential values (ThT, a.u.) for each lineage as a function of time, for ΔL34 mutant. On the right, projection of the maximum membrane potential (ThT, a.u.) for each lineage. The color bar indicates the intensity range of the ThT signal.

Together these results indicate that not only chemical perturbations of the ribosome, but direct structural perturbations of the ribosomal stability result in a transient hyperpolarization and a repercussion in the cell viability.

Next, we asked whether a genetic perturbation that increases the ribosomal stability would have the opposite effect. With this purpose, we selected the L22 protein subunit of the ribosomal complex (L17 in eukaryotes), which is important for the proper folding and stabilization of the 23S rRNA (Ban et al., 2000; Akanuma et al., 2012) (Figs. 4.14A,B). Specifically, we generated a duplication of a region in the L22's loop which has been reported to crowd out the space within the ribosome, conferring resistance against macrolide antibiotics, such as streptomycin (Sohmen et al., 2015) (Figs. 4.14B and 4.22B).

Consistent with our expectation, we observe that the L22 mutant (*rpmE* mutant, L22*) presents a very low fraction of hyperpolarized cells (Fig. 4.15A), even in presence of spectinomycin (Fig. 4.15B). Moreover, the elongation rate of the L22* mutant is slightly shifted towards higher values (Figs. 4.16A,B). Consequently, we observe less death in the L22* mutant (Figs. 4.16C,D). These results indicate that an increase in the stability of the ribosomal structure prevents membrane hyperpolarization and increases survival in front of ribosomal stress.

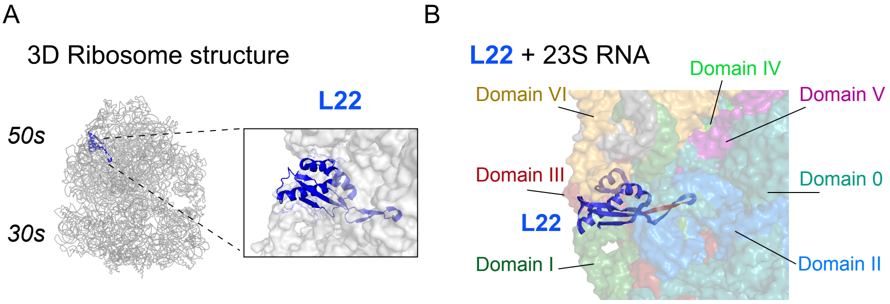

Figure 4.14: Location of the ribosomal protein L22. A) Scheme of the 3D structure of the ribosome showing the location of the ribosomal protein L22. The right panel shows a magnified view of the L22 region (in blue). The ribosome structure was obtained from Protein Data Bank (PDB, ID: 3j9w) and is represented using Pymol. B) Lateral view of L22 and 23S RNA interface generated using data from Protein Data Bank (PDB, ID: 3j92) and represented using Pymol. Different domains of 23S RNA are presented in different colors. The region that is duplicated in the L22* mutant is marked in red. Notice that the ribosomal protein L22 interacts with all the domains of 23S.

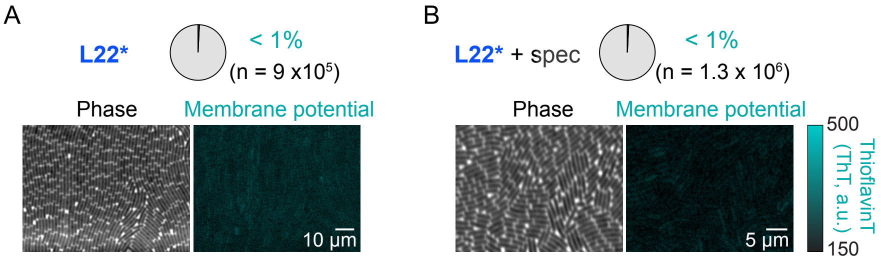

Figure 4.15: The L22* mutant presents lower membrane potential hyperpolarization. A) Phase (left) and fluorescence (right) images of the L22* mutant strain. The pie chart shows the fraction of cells experiencing transient hyperpolarization in a population of 9 x 10^5 cells for the L22* mutant. B) Phase (left) and fluorescence (right) images of the L22* mutant strain in presence of spectinomycin. The size and color scale in panels A and B are set the same scale as in Fig. 4.3C. The pie chart shows the fraction of cells experiencing transient hyperpolarization in a population of 1.3 x 10^6 cells in the L22* mutant upon addition of spectinomycin.

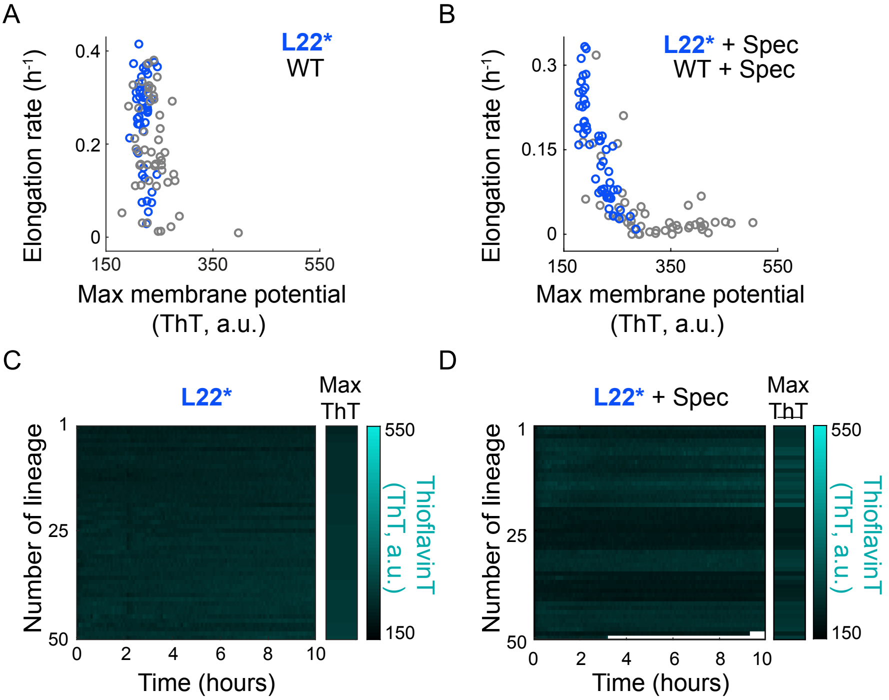

Figure 4.16: The L22* mutant presents higher elongation rate, and reduced cell death. A) Maximum membrane potential (ThT, a.u.) as a function of the elongation rate (h^{-1}) for wild-type (gray, $n = 50$) and the L22* mutant (blue, $n = 50$). B) Maximum membrane potential (ThT, a.u.) as a function of the elongation rate (h^{-1}) for wild-type (gray, $n = 50$) and the L22* mutant (blue, $n = 50$), both in the presence of spectinomycin. C) Kymograph containing the membrane potential values (ThT, a.u.) for each lineage as a function of time, for the L22* mutant. On the right, projection of the maximum membrane potential (ThT, a.u.) for each lineage. The color bar on the right marks the intensity range of the ThT signal. D) Kymograph containing the membrane potential values (ThT, a.u.) for each lineage as a function of time, for the L22* mutant in the presence of spectinomycin. On the right, projection of the maximum membrane potential (ThT, a.u.) for each lineage.

To identify the mechanism in the L22* mutant strain that reduces the hyperpolarization events we turned to mass spectrometry proteomics (Dost et al., 2012) We performed a comparative analysis of the protein expression levels in the L22* mutant strain compared to the other conditions that increase the hyperpolarized cell fraction, using wild-type strain as a reference. The results, shown in Fig. 4.17, reveal that while ion transporters represent 3,1% of the total measured proteome (86 ion transporters / 2798 total proteins) (Fig. 4.17A, right), they make up 28.6% of all the proteins up-regulated in the L22* mutant strain (6 ion transporters / 21 proteins) (Fig. 4.17A, left, and table 4.3). In particular, we found that the only known magnesium transporters, YhdP (Akanuma et al., 2014) and MgtE (Wakeman et al., 2014), are up-regulated in the L22* mutant strain (Fig. 4.17B).

Thus, these data reveal a clear up-regulation of ion transporters in the L22* mutant strain, suggesting that this mutant has a higher flux of magnesium ions, which will increase ribosome stability. This idea is supported by the fact that the L22* mutant strain presents a higher growth rate, which would indicate a higher number of ribosomes. Then, modulation of magnesium content seems to provide tolerance to ribosomal stress.

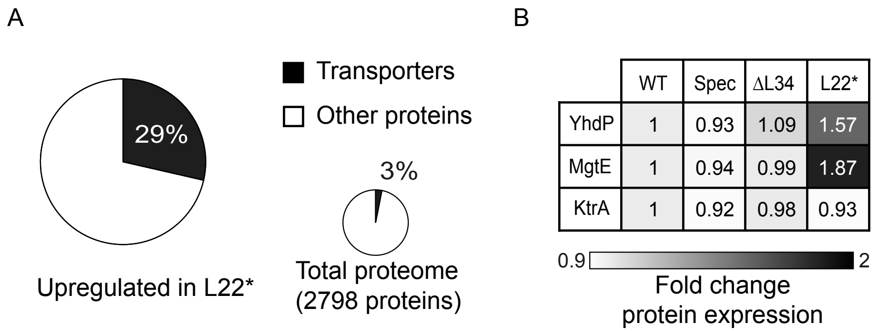

	WT	Spec	ΔL34	L22*
YhdP	1	0.93	1.09	1.57
MgtE	1	0.94	0.99	1.87
KtrA	1	0.92	0.98	0.93

Figure 4.17: Up-regulation of magnesium transporters in the L22* mutant strain. A) Pie chart representing the total amount of ion transporters up-regulated in the L22* mutant (left, $n = 21$). Pie chart (right) representing the percentage of ion transporters among the total proteome ($n = 2798$). B) Table representing the values of the fold change protein expression for the magnesium transporters (YhdP and MgtE), and a potassium transporter (KtrA) in WT, spectinomycin addition, ΔL34 mutant, and L22* mutant. The grayscale shadowing represents the fold change in protein expression.

4.7 Ribosomal stabilization by increase in the magnesium content

To test further the idea that the flux of magnesium ions could prevent hyperpolarization events, and not other ions, we performed an experiment where wild-type cells were under antibiotic stress, and during a period of time an excess of a specific ion was applied, to increase the influx. As Fig. 4.18 shows, an increase of extracellular magnesium in the medium from 2 mM to 20 mM quenches transient hyperpolarization events. In contrast, other cations such as potassium, sodium or calcium are less effective. The quantification of the hyperpolarization events in the presence or absence of the ion excess is represented in Fig. 4.18, where we can appreciate the higher effect of magnesium compared to the other ions. These results are consistent with our proteomics data and prior publications that showed potassium, sodium or calcium to be less effective in stabilizing ribosomes when compared to magnesium (Weiss et al., 1973).

From these results, we can also observe that the effect of the magnesium influx is reversed, since when the excess ions are removed the hyperpolarization events occur again (Fig. 4.18A). These results are consistent with the idea that magnesium influx prevents hyperpolarization events in bacteria that are subjected to ribosomal stress, such as the one induced by ribosomal-targeting antibiotics, and this increase in the ion content promotes bacterial survival.

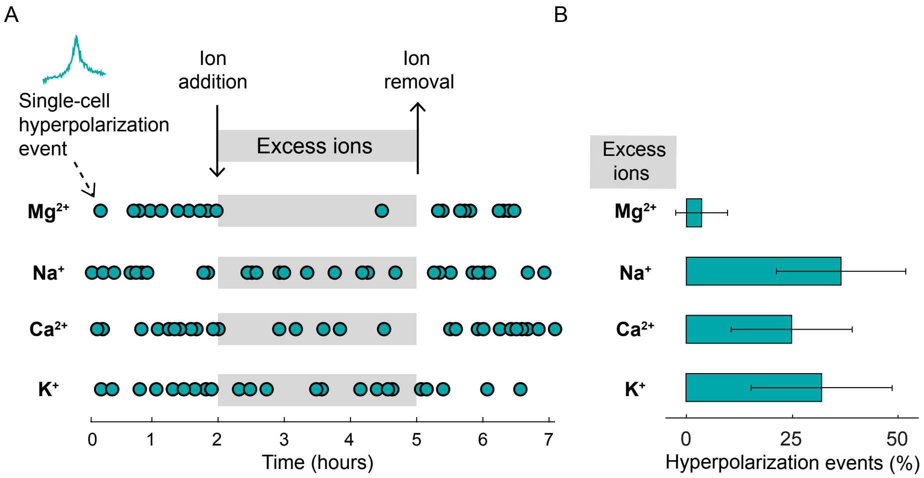

Figure 4.18: An increase in magnesium ions prevents hyperpolarization events under antibiotic stress. A) Temporary excess of ion concentration in the presence of spectinomycin. Each circle represents a single-cell hyperpolarization event, and each row is for the excess of one specific ion: magnesium, sodium, calcium, or potassium. B) Bar plot for the quantification of hyperpolarization events that occur during the excess of the specific ion.

4.7.1 Recovery of the ΔL34 phenotype by increasing the magnesium ion content

On account of the results of the magnesium addition experiment described in Section 4.7 above, we asked whether an excess of magnesium ions in the medium can rescue the phenotype of the ΔL34 mutant, reducing the number of hyperpolarized cells and recovering the ribosomal state. Accordingly, we measured the percentage of hyperpolarized cells for different concentrations of the ion (Figs. 4.19A,B). Our results show that indeed the fraction of hyperpolarized ΔL34 cells is reduced in response to the addition of magnesium.

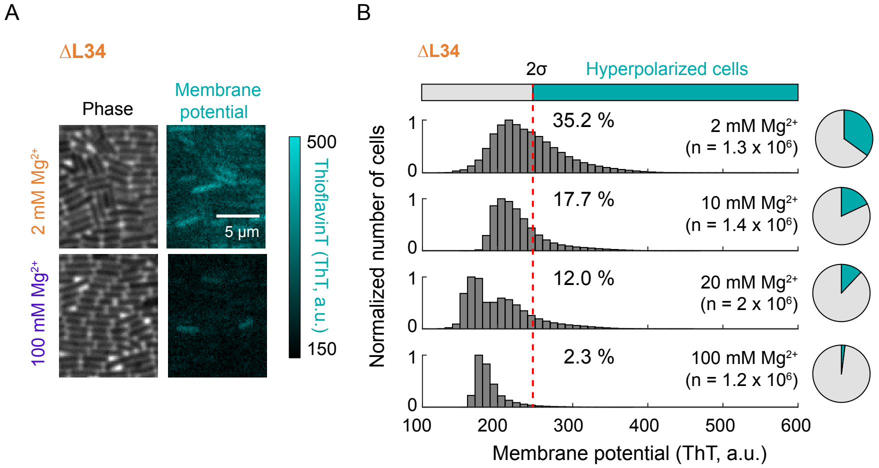

Figure 4.19: Increase of magnesium content decreases the hyperpolarized fraction of the ΔL34 mutant. A) Snapshots in phase (left) and fluorescence (right), for the ΔL34 mutant in the presence of 2 mM magnesium concentration (top) or 100 mM (bottom). The color bar on the right indicates the membrane potential (ThT, a.u.) signal. B) Membrane potential distributions for ΔL34 mutant in presence of different magnesium concentrations (2 mM, 10 mM, 20 mM and 100 mM, from top to bottom). The red dashed line indicates 2 standard deviations from the mode of the wild-type distribution (same in Fig. 4.4). Pie charts represent the percentage of hyperpolarized cell fraction (in cyan) for each magnesium concentration.

To verify that the recovery of the membrane potential behavior caused by magnesium also improves the ribosomal state of the ΔL34 mutant strain, we tracked single cells for increasing concentrations of magnesium. We find indeed that increasing magnesium recovered the growth defect in the mutant, consistent with the literature (Akanuma et al., 2014) (Fig. 4.20A).

Together, these results indicate that hyperpolarization events in bacterial cells induced by ribosome destabilization can be counteracted by magnesium-mediated stabilization of the ribosome complex. This relationship suggests that the destabilization of the ribosomal structure in the ΔL34 mutant strain can be recovered by an increase in the magnesium cell content (Figs. 4.20A,B).

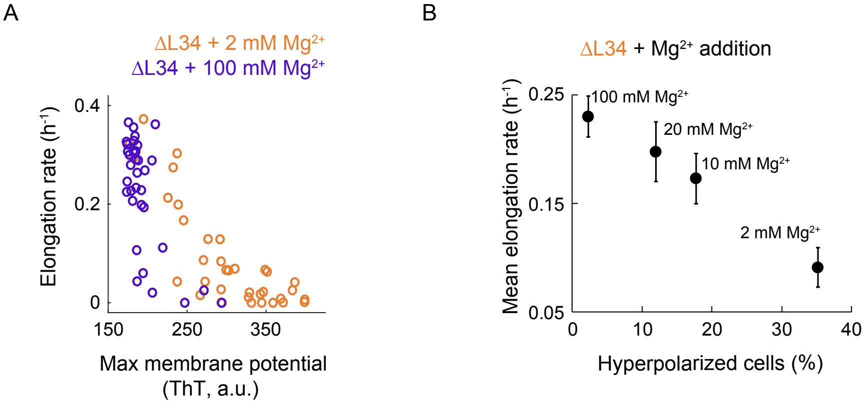

Figure 4.20: Increase of magnesium content rescues the phenotype of the ΔL34 mutant. A) Elongation rate (h^{-1}) as a function of the maximum membrane potential (ThT, a.u.) for ΔL34 in presence of 2 mM of magnesium (orange, $n = 50$), or 100 mM (purple, $n = 50$). B) Mean elongation rate decreases as a function of the percentage hyperpolarized cells increases, in relation to the concentration of magnesium in the media for ΔL34 mutant (100mM, $n = 40$; 20mM, $n = 30$; 10mM, $n = 19$; 2mM, $n = 29$). Confidence interval for both axes is indicated with bars. Note that the CI for the x-axis is smaller than the symbol used in this plot.

4.8 Ion flux modulation determines bacterial survival

Finally, if we plot the data for the hyperpolarized cell percentage and the mean elongation rate for the different strains and perturbations studied in this Chapter, we observe that the different conditions reveal an overall negative correlation between these two observables (Fig. 4.21A). This result indicates a relationship between ribosomal stability (and activity), measured by the mean elongation rate, and the membrane potential dynamics. We also observe that the increase in the magnesium content can modulate the position of the condition along this phase space towards lower hyperpolarized cell fraction and higher elongation rates, as we observed with the ΔL34 strain mutant. Therefore, magnesium ion concentration stabilizes the ribosomal structure, which can be observed by the membrane potential dynamics. Separately, we also studied the cell survival, defined as the number of generations that remain alive after ten hours of observation. We can differentiate two groups (Fig. 4.21A): One group with lower survival, that corresponds to high membrane potential and another group with higher survival and low membrane potential.

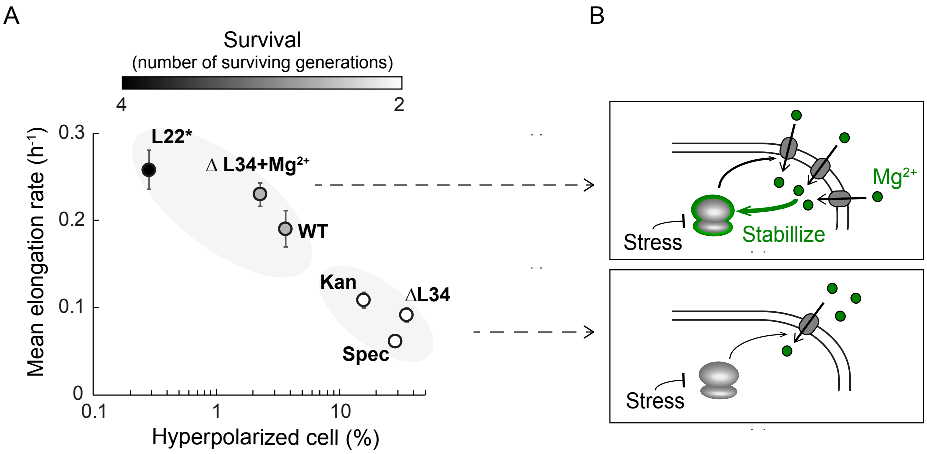

Figure 4.21: Hyperpolarized cell fraction is correlated with mean growth rate and survival for all ribosomal perturbations tested. A) Summary of the mean elongation rate as a function of hyperpolarized cell percentage (in logarithmic scale) for all the conditions used in this study: wild-type (WT), wild-type in the presence of spectinomycin (Spec), wild-type in the presence of kanamycin (Kan), L34 deletion strain (ΔL34), L34 deletion strain in the presence of 100 mM magnesium (ΔL34+Mg^{2+}), and L22 loop duplication strain (L22*). Error bars represent standard error for the y-axis and 95% CI for the x-axis. Notice that the x-axis error bars are smaller than the symbols used in this plot. Greyscale shadowing (see top bar) indicates the mean number of surviving generations during an observation period of 10 hours. B) Cartoon representing the proposed bacterial mechanism to cope with ribosomal stress. Ion flux modulation, in particular magnesium content, determines tolerance to ribosomal stress (surviving cell: top, dying cell: bottom).

4.9 Discussion

In this Chapter, we have shown a new perspective on the heterogeneous antibiotic response of bacteria that emphasizes the importance of ion flux regulation in bacterial survival. By monitoring membrane potential dynamics and the ribosomal state of individual cells over time, we show that higher magnesium flux promotes growth and survival of bacteria that are exposed to ribosomal stress (Fig. 4.21B). It has been known that magnesium ions stabilize the structure and function of the ribosome complex, which is comprised of numerous negatively charged rRNA subunits (Nierhaus, 2014) (Fig. 4.2A). We now show that the ribosome-stabilizing function of magnesium plays an important role in promoting tolerance of bacterial cells against ribosome-targeting antibiotics. Consequently, modulation of ion flux becomes a key determinant of bacterial stress tolerance.

Our study also provides a new perspective on the heterogeneous antibiotic response of bacteria that emphasizes the importance of ion flux regulation in bacterial survival. As it was mentioned, with advances in single-cell measurements, various differences among genetically identical bacterial cells have been identified, such as metabolic states, ability to take up extracellular DNA and formation of spores (Süel et al., 2007; Kuchina et al., 2011). Here we show that bacteria also differ in their ion flux modulation and that this difference is an important determinant of cellular survival. However, it still remains unclear how the phenotypic heterogeneity may arise. One possibility would be due to noise in the number of the ion transporters, which would lead to bistability in magnesium content of cells.

Altogether, these results reveal an intriguing interaction between ribosomes and the membrane potential, suggesting that these ancient and fundamental processes that operate in all living cells have a profound connection. Cellular utilization of electrochemical gradients across membranes and the utilization of ribosome machines for protein synthesis are two of the most important features of all living organisms. Our data indicate a bi-directional functional link between ion flux and ribosome function. Ribosomes are necessary to synthesize membrane proteins that govern flux of ions across the membrane, as it is energetically unfavorable for charged molecules to diffuse across the lipid bilayer of a cell. In turn, we now show that flux of ions, specifically magnesium, has a direct impact on ribosome function. The functional interplay between ribosomes and the membrane potential thus offers a new perspective on the link between fundamental cellular processes that are essential for life.

4.10 Appendix

4.10.1 Experimental methods

Strains

The *B. subtilis* strains used in this Chapter are listed in Table 4.10.1. The wild-type strain was a gift from Wade Winkler (University of Maryland). The ribosomal protein L22 loop duplication was obtained as a spontaneous Erm^{R} mutant. The spontaneous Erm mutant has a seven amino acid duplication (94SQINKRT100; Fig. 4.22A), which is the same as described earlier by Chiba et al.. The strain was confirmed by the whole genome sequencing. The L34 deletion (*rpmH::cat*) was generated using the chromosomal integration vector, pER449 (a generous gift from Wade Winkler, University of Maryland) (Fig. 4.22B). The pER450-based integration vector to replace *rpmH* gene with chloramphenicol resistance gene was constructed by Gibson assembly of four PCR products. The 5' arm and 3' arm fragments were PCR amplified using the following partial overlapping primers: ccatgattacgccaagcTCGCCTTGCAGTGAGTGGGC and gtagcgtctctagacacgagcgACCTCCCTCGAGGAATAGCTGTTAAAG for 5' arm; ccagatcctctacaagctttcacttcGGCCACTGAATAATGTCAGTGG and gcttaactatgcggcatcagaTCACACTCGAGCATCCAGCC for 3' arm, and integrated as recombination arms with pER450 (Cm^R) vector PCR amplified using the following primers: ctcactgcaaggcgAGCTTGGCGTAATCATGGTCATAGC and ggatgctcgagtgtgaTCTGATGCCGCATAGTTAAGCCAGC for the vector backbone; tgaaagcttGTAGAGGATCTGGAGCTGTAATATAAAAAC and cgctcgtgtctagagaCGCTACGCTCAAATCCTTTAAAAAAACAC for the *cat* gene (overlapping bases in lower case; this region facilitates fusion in Gibson assembly). *cydA::erm* and *cccA::erm* strains are a generous gift from Heidi Arjes in K.C. Huang's lab.

Table 4.1: Table of strains used in this study.

Strain	Genotype	Source
WT	*B. subtilis NCBI 3610*	Wade Winkler, Univ. of Maryland
L22 loop duplication	*rplV94*	This study
ΔL34	*rpmH::cat*	This study

Growth and imaging conditions

B. subtilis strains of interest were streaked on a fresh LB agar plate (with 5 μg/mL chloramphenicol or 5 μg/mL erythromycin when appropriate) a day before the experiment and incubated at 37°C overnight. A single colony of the desired strain was used for inoculation of 3 mL LB medium and grown at 37°C with shaking. The saturated culture was washed with MSgg media (5 mM potassium phosphate (pH 7.0), 100 mM 3-(N-morpholino)propanesulfonic acid (pH 7.0), 2 mM $MgCl_2$, 700 μM $CaCl_2$, 50 μM $MnCl_2$, 100 μM $FeCl_3$, 1 μM $ZnCl_2$, 2 μM thiamine, 0.5% glycerol, 0.5% glutamate), and then immediately loaded into a commercial Y04D microfluidic plate (EMD Millipore) and connected to media flow controlling CellAsic Onix2 device. Cells in the microfluidic chamber were grown

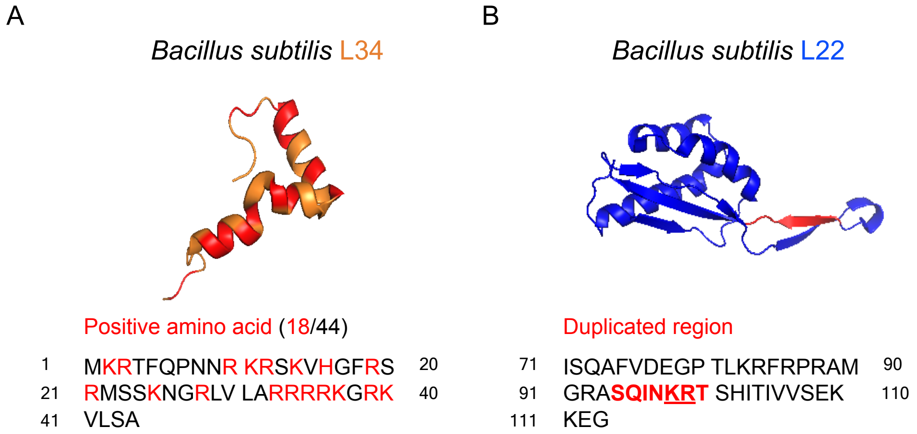

Figure 4.22: Structure of the ribosomal proteins L34 and L22. A) 3D structure and amino acid sequence of *B. subtilis* L34. Positively charged amino acids are colored in red. The structure was obtained from Protein Data Bank (PDB, ID: 3j92) and is represented using Pymol. B) 3D structure and amino acid sequence of *B. subtilis* L22. Duplicated amino acids are colored in red and positive amino acids are underlined. The structure was obtained from Protein Data Bank (PDB, ID: 3j92) and is represented using Pymol.

in MSgg media at 37°C for 120 minutes, and then the temperature was kept at 30°C for the rest of the experiment. Membrane potential dynamics was measured using the fluorescent cationic dye Thioflavin-T (ThT, Acros organics, CAS: 2390-54-7) added to the MSgg media two hours before the imaging. When required, 2 mg/L of spectinomycin or 0.5 mg/L of kanamycin was added three hours into the imaging. For the L34 deletion mutant (ΔL34), MSgg media was supplemented with final concentration of 20 mM $MgCl_2$ before imaging, to ensure growth. When appropriate, $MgCl_2$ concentration was changed two hours before the imaging and kept at the desired concentration (2 mM if not stated otherwise).

Growth condition for proteomics sample preparation is described later in sample preparation of Section 4.10.3.

Time-lapse microscopy

Growth and membrane potential dynamics of *B. subtilis* cells were monitored with time-lapse fluorescent microscopy at 30°C using Olympus IX-81 inverted microscope with motorized stage (ASI). Images were taken with ORCA-Flash 4.0 V2 camera (Hamamatsu) and a Lambda XL light source

(Sutter instruments). Single layers of cells were imaged every 5 minutes under 40x objective lens. Before imaging, exposure time was defined based on a calibration using fluorescent beads, in order to ensure the similar light exposure between different experiments.

4.10.2 Modeling the influence of ion flux on membrane potential dynamics

In order to establish a link between the cation flux through the bacterial membrane and the dynamics of the membrane potential, we consider the following minimal two-dimensional dynamical system:

$$\frac{dV}{dt} = -g_L(V - V_L) - g_C(V - V_C) + \alpha_{in}\, C_e - \alpha_{out}\, C \tag{4.11}$$

$$\frac{dC}{dt} = F(-g_c(V - V_C) + \alpha_{in}\, C_e - \alpha_{out}\, C) \tag{4.12}$$

where $V(t)$ is the membrane potential, and $C(t)$ is the intracellular concentration of the cation. We consider that the potential across the membrane can change due to three flux processes affecting the cation: passive flow through a channel (g_C term in the V equation above), active import (α_{in} term), and active export (α_{out} term). The leak term g_L represents the rest of factors influencing the dynamics of the membrane potential. The dynamics of the cation $C(t)$ is also affected by the three transport terms described above, as shown in its corresponding differential equation. The coefficient F is used to relate the current to ion concentrations. Note that the extracellular cation concentration C_e is assumed constant. The Nernst potential of the cation is given by:

$$V_C = V_0\ log\ \frac{C_e}{C} \tag{4.13}$$

When the steady state condition of the cation concentration ($\frac{dC}{dt} = 0$) is used in the corresponding condition of the membrane potential ($\frac{dV}{dt} = 0$), we immediately conclude that the steady-state value of the latter variable is simply $V = V_L$, irrespective of the parameters controlling the ion flux dynamics. We can thus expect that ion flux modulation will affect only the *transient* behavior of the system but not its stationary state, which is the main characteristic of a perfectly adapting system. In agreement with this expectation, we observe that the system responds to a drop in the activity of the channel by producing a hyperpolarization pulse as shown in Fig. 4.6B of the main text. This decrease in activity is modeled by an exponential decay in the parameter g_c at a given time ($t = 4$ hours in Fig. 4.6B), from an initial value g_{C1} to a final value g_{C2}, with decay constant δ_c:

$$\frac{dg_c}{dt} = -\delta_C (g_C - g_{C2}) \tag{4.14}$$

The values of the model parameters are given in table 4.2.

Table 4.2: Parameter values for the model of membrane potential and ion flux modulation.

Parameter	Description	Value
g_L	Leak conductance	0.0025 1/s
V_L	Rest potential	-90 mV
g_{C1}	Initial cation channel conductance	0.0125 1/s
g_{C2}	Final cation channel conductance	0.003125 1/s
δ_C	Cation channel decay rate	0.025 1/s
V_0	Cation Nernst potential when $C = C_e$	1 mV
C_e	Extracellular cation concentration	2 mM
α_{in}	Import rate	0.075 1/s
α_{out}	Export rate	0.075 1/s
F	Conductance coefficient	0.0067 mM/mV
β_T	ThT input rate	0.01 mM/s
δ_{hyp}	ThT export rate under hyperpolarization	0.00025 1/s
δ_{dep}	ThT export rate under depolarization	0.005 1/s
V_S	Steepness of the ThT response function	0.1 mV

Experimentally, membrane potential is monitored through the fluorescent dye ThT. We model the dynamics of ThT in the following way:

$$\frac{dT}{dt} = \beta_T - (\delta_{hyp} + \delta_{def}\ f(V))\ T, \tag{4.15}$$

where $T(t)$ represents the concentration of ThT inside the cell. We assume that the ability of the cell to retain the positive dye molecule depends on the membrane potential, in such a way that when the cell hyperpolarizes, it becomes able to retain enough ThT to produce a measurable fluorescence signal. This is modeled by means of the sigmoidal function:

$$f(V) = \frac{1}{2}\left(1 + \tanh\left(\frac{V - V_L}{V_s}\right)\right), \tag{4.16}$$

which ranges from 0 (when V is sufficiently larger than V_L, i.e., when the cell is sufficiently hyperpolarized) to 1 (when the cell is sufficiently depolarized). The steepness of the sigmoidal is controlled by the parameter V_s.

4.10.3 Proteomic labeling and Mass spectrometry

Sample preparation

Cells were grown in 3 mL LB at 37°C with shaking for 3.5 hours. The saturated culture was washed with MSgg media, diluted 100 times, and further incubated in MSgg at 30°C with shaking for 16 hours. 6 mL of cultures were then pelleted at 4000 rpm for 4 minutes. Pellets were resuspended in 6 mL as followed: WT with MSgg media, WT with MSgg media supplemented with 2 mg/L spectinomycin, WT with MSgg media supplemented with 100 mg/L spectinomycin, WT with MSgg media supplemented with 0.5 mg/L kanamycin, ΔL34 with MSgg media, ΔyhdP with MSgg media, and L22* with MSgg media. Resuspended cultures were further incubated at 30°C with shaking for 4 hours before measuring OD600. Then we washed the rest of the cultures three times with 2 mL of Tris-HCl buffer (pH 7.0). Next, the samples were pelleted to the volume of about 100 μl.

iTRAQ labeling of peptide

Cell pellets were suspended in 200 μL cold extraction buffer (6 M guanidine hydrochloride (GdnHCl)/100 mM Hepes/10 mM Tris(2- carboxyethyl)phosphine (TCEP), pH 7). 100 μL 0.5 mm ZrO_2 beads were added. Cells were lysed by shaking in a Bullet Blender tissue homogenizer (Next Advance, Inc.) at speed 8 for 3 minutes. Proteins were denatured by heating at 94ºC for 5 minutes. Samples were diluted 6 times to 1 M GdnHCl with 50 mM Hepes. Proteins were first digested with Lys-C (Wako Chemicals, 125-05061) at 37ºC for 15 minutes. Protein solution was further diluted 2 times to 0.5 M GdnHCl with 50 mM Hepes and digested with trypsin (Roche, 03 708 969 001) for 4 hours. Digested peptides are purified on a Waters Sep-Pak C18 cartridges, eluted with 60% acetonitrile. TMT-10 labeling is performed in 50% acetonitrile/150 mM Tris, pH7. TMT labeling efficiency is checked by LC-MS/MS to be greater than 99%. Labeled peptides from different samples are polled together for 2D-nanoLC-MS/MS analysis. An Agilent 1100 HPLC system is used to deliver a flow rate of 600 nL/min to a custom 3-phase capillary chromatography column through a splitter. Column phases are a 30 cm long reverse phase (RP1, 5 μm Zorbax SB-C18, Agilent), 8 cm long strong cation exchange (SCX, 3 μm PolySulfoethyl, PolyLC), and 40 cm long reverse phase 2 (RP2, 3.5 μm BEH C18, Waters), with the electrospray tip of the fused silica tubing pulled to a sharp tip (inner diameter <1 μm). Peptide mixtures are loaded onto RP1, and the 3 sections are joined and mounted on a custom electrospray adapter for on-line nested elutions. Peptides are eluted from RP1 section to SCX section using a 0 to 80% acetonitrile gradient for 60 minutes, and then are fractionated by the SCX column section using a series of 15 step salt gradients of ammonium acetate over 20 minutes, followed by high-resolution reverse phase separation on the RP2 section of the column using an acetonitrile gradient of 0 to 80% for 150 minutes.

Data acquisition

Spectra are acquired on a Q-exactive-HF mass spectrometer (Thermo Electron Corporation, San Jose, CA) operated in positive ion mode with a source temperature of 325°C and spray voltage of 2 kV. Automated data-dependent acquisition was employed of the top 20 ions with isolation windows of 1.0 Da and collision energy of 30. The mass resolution is set at 60000 for MS and 30000 for MS/MS scans, respectively. Dynamic exclusion is used to improve the duty cycle.

4.10.4 Quantification and statistical analysis

Population analysis: segmentation and determination of hyperpolarized cell fraction

Trainable Weka segmentation plugin from FIJI (ImageJ) was used to segment cells from each phase contrast image. Custom-written macro was used to automatically compile the mask and segmentation data from a time-lapse movie. Non-segmented groups of cells, spores, and background noise were eliminated through size filtering. A mask created for each time point was used to extract the mean ThT intensity for each segmented cell (see Fig. 2.5 in the Introduction). Histograms were generated by compiling ThT intensities from two to four independent time-lapse movies. The fraction of hyperpolarized cells was determined by using a threshold of two standard deviations from the mode of the WT without any antibiotics (Fig. 4.23).

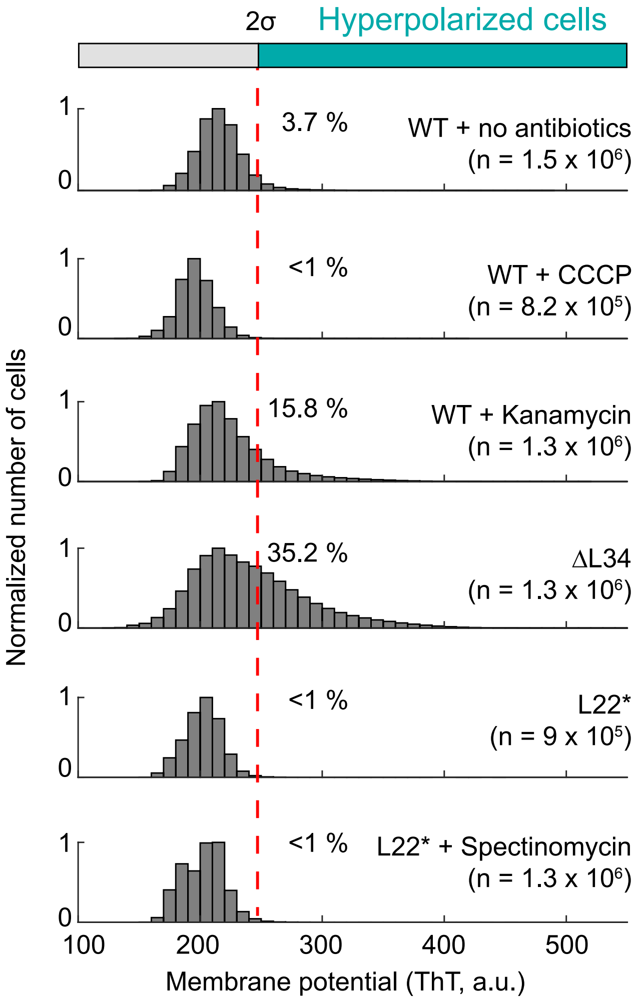

Figure 4.23: Membrane potential distribution for all the conditions. Distribution of ThT intensities in a population of cells under listed conditions. 'WT,' 'ion removal' and spectinomycin data are a duplicate of Fig. 4.4. The dashed red line represents two standard deviations from the mode, which is used as a cutoff to determine the fraction of hyperpolarized cells. 'n' represents the number of analyzed cells. Segmented cells from three or four independent experiments are used for each condition, except CCCP addition (two experiments).

Determination of transient-hyperpolarizations

Single-cells were tracked by custom software developed in MATLAB (MathWorks) using time-lapse phase images from two to three independent experiments for each condition. Obtained ROIs were applied to the corresponding CFP images, and ThT signal of the cell was measured as a function of time (from 30 minutes before any perturbation to the 10 hours into the perturbation unless the cell died before 10 hours). This trace was used to determine whether the cell experienced a transient hyperpolarization. A basal line for each trace was defined as a linear vector extrapolated from the mean of the first 30 minutes to the mean of the last 30 minutes of each trace. Then, ThT amplitude was calculated as the difference in the intensities between the maximum ThT signal and the basal line. If the amplitude is greater than at least two standard deviations of the WT basal line values, the cell was determined to have a transient hyperpolarization.

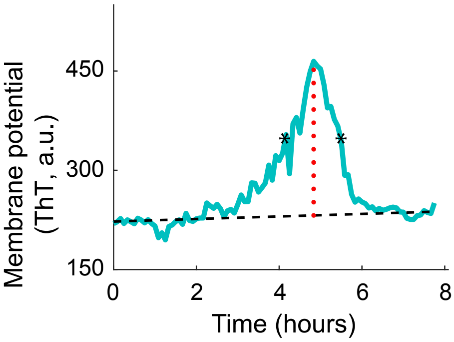

Figure 4.24: An example of the determination of a transient hyperpolarization. Time traces of membrane potential signal over time (ThT, a.u.). Horizontal black dashed line represents the baseline, the vertical red pointed line shows the amplitude between the maximum membrane potential to the baseline, and the two asterisks mark the half-amplitude of the peak. This transient hyperpolarization has a maximum of 464.58 a.u., and an amplitude of 232.74 a.u.

Quantification of elongation rate and maximal membrane potential

For each lineage's time trace of cell length, an exponential line was fitted between consecutive divisions (for each generation). The function $f(x) = ae^{bx}$ was used for the fitting, where b is the elongation rate of a cell. The 'elongation rate' (Figs. 4.9A, 4.13A, 4.15C, D, and 4.19C) is a 'mean elongation rate' of a single lineage. On the other hand, 'mean elongation rate' (Figs. 4.19D and 4.21A) is the population mean elongation rate under a certain condition. The maximum membrane potential was determined as the maximum value of ThT signal from the corresponding time trace.

Analysis of proteomic data

The raw data were extracted and searched using Spectrum Mill vB.06 (Agilent Technologies). MS/MS spectra with a sequence tag length of 1 or less are considered to be poor spectra and were discarded. The remaining MS/MS spectra are searched against UniProt *Bacillus subtilis* (strain 168) proteome (4271 protein sequences). A 1:1 concatenated forward-reverse database was constructed to calculate the false discovery rate (FDR). Common contaminant protein sequences were included in the database. There are 8568 total protein sequences in the database. Search parameters are set to Spectrum Mill's default settings with the enzyme parameter limited to full tryptic peptides with a maximum miscleavage of 1. Cutoff scores were dynamically assigned to each dataset to obtain the false discovery rates (FDR) of 0.1% for peptides, and 1% for proteins. Proteins that share common peptides were grouped using principles of parsimony to address protein database redundancy. Total TMT-10 reporter intensities were used for relative protein quantitation. Peptides shared among different protein groups were removed before quantitation. Isotope impurities of TMT-10 reagents were corrected using correction factors provided by the manufacturer (Thermo). Median normalization was performed to normalize the protein TMT-10 reporter intensities in which the log ratios between different TMT-10 tags are adjusted globally such that the median log ratio is zero.

In order to determine proteins enriched in L22*, we first selected proteins being expressed over 1.5 fold in the L22* strain compared to WT. Next, we selected proteins being expressed less than 1.1 fold in other conditions compared to WT. These proteins are listed in Table 4.3. Protein function assignment is based on *Bacillus subtilis* databases as followed: Subtiwiki, BsubCyc, UniProt. Membrane proteins with unknown function were classified as putative transporters.

Peak identification during excess ion addition

The addition of excess ions in the media globally decreases ThT signal. For the analysis of single-cell traces with excess ions experiments

(Figs. 4.18A,B), each ThT time trace was corrected to eliminate global decrease. The basal line for ThT signal was obtained from the segmentation results of each movie and determined as described earlier. The difference between the basal line before/after addition of excess ions and the basal line during the addition of excess ions was then added to ThT signal during ion addition. This corrected time trace was used to determine the transient hyperpolarization as described earlier. For each condition, 5 to 8 cells with the brightest ThT signal were selected for each hour of the experiment and tracked during the duration of the experiment. We identified the timing of the ThT maxima for each time trace as a single-cell hyperpolarization event, and plotted it in Fig. 4.18A. Single-cell hyperpolarization events during the addition of excess ions is presented as a percent of all hyperpolarization events with a 95% CI in Fig. 4.18B.

Table 4.3: Transporters up-regulated in the L22* mutant strain. The values represent the fold change protein expression, normalized in reference to wild-type values.

Protein	Description	WT	Spec	ΔyhdP	ΔL34	L22*
YodF	Uncharacterized symporter, similar to amino acid permease	1	0.8313	0.6878	0.8726	1.9419
MgtE	Magnesium transporter MgtE	1	0.9378	0.5745	0.9871	1.8671
YybJ	Uncharacterized ABC transporter ATP-binding protein	1	0.9051	1.0353	0.9169	1.7698
YoaB	2-oxoglutarate permease (proton symporter)	1	0.7713	0.7259	0.8677	1.6777
YhdP	Magnesium efflux pump	1	0.9317	0.2654	1.0875	1.5658
YbeC	Probable amino acid-proton symporter	1	1.0562	0.7222	0.9654	1.5553
NtdC	Glucose-6-phosphate 3-dehydrogenase	1	0.6768	0.5104	0.6734	6.2505
NtdA	3-oxo-glucose-6-phosphate:glutamate aminotransferase	1	0.6941	0.5471	0.6609	5.0243
NtdB	Kanosamine-6-phosphate phosphatase	1	0.7048	0.5708	0.6247	4.9011

YqjL	General stress protein, putative hydrolase involved in oxidative stress resistance	1	0.9244	1.0904	0.9953	2.3061
YdiP	Similar to DNA-3-methyladenine glycosidase II	1	0.9414	0.9326	0.8742	1.9005
EpsN	UDP-2,6-dideoxy 2-acetamido 4-keto glucose aminotransferase	1	0.6624	0.8253	0.7060	1.7488
BioD	ATP-dependent dethiobiotin synthetase	1	0.8705	0.9979	0.9372	1.7110
YokE	SPBc2 prophage-derived uncharacterized protein	1	1.0743	1.0866	1.0552	1.6777
MtnK	Methylthioribose kinase	1	0.6853	0.9639	0.9603	1.6505
PxpC	5-oxoprolinase subunit C	1	1.0464	0.9760	0.8720	1.6486
YvyE	IMPACT family member	1	1.0190	0.9679	1.0736	1.5678
KipR	HTH-type transcriptional regulator KipR	1	0.9142	0.8505	0.7104	1.5561
RapG	Response regulator aspartate phosphatase G	1	0.9898	0.9689	1.0543	1.5378
MtnA	Methylthioribose-1-phosphate isomerase	1	0.9512	1.0260	0.9004	1.5105

Chapter 5

Bacterial proliferation in mixed-species populations under antibiotic stress

As mentioned in the Introduction, successful bacterial proliferation requires accurate coordination of the processes underlying cell wall synthesis, since the correct assembly of the components of the cell wall are crucial for cell viability. This explains why the processes underlying to treat bacterial infections, namely beta-lactam antibiotics (which include penicillin and penicillin derivatives) target the processes underlying bacterial cell wall formation. However, while it is recognized that interaction between different bacterial species present in infections can modify the outcome of their response to antibiotics, clinical research has been focused on isolated cultures, ignoring the possible repercussion of the interplay between the different species.

In this Chapter, we will study the dynamics of bacterial proliferation under the action of membrane-targeting antibiotics, and the effects of the interaction between species with differing sensitivity to the drug. For simplicity, we have selected a reduced community formed by two well-known species that can be found in the human microbiome, namely *Escherichia coli* and *Bacillus subtilis*, in the presence of the β-lactam antibiotic ampicillin. We have chosen these two bacterial species because *E. coli* is sensitive to this drug, *B. subtilis* is tolerant. Our goal is to investigate whether these two bacterial species, with opposing response to ampicillin, maintain their distinct responses when coexisting together, or whether molecular interactions between the two species modify their response to the membrane-targeting antibiotic. With the intention of interpreting the different experimental observations, we present a model developed by Dr. Jordi Garcia Ojalvo to establish a theoretical framework that explains the observed behavior of the mono-cultures and co-cultures.

5.1 Stress responses in bacterial mixed-species communities

Bacteria live in their natural habitat in the form of complex communities that contain different bacterial species (Cordero et al., 2012), and other kinds of microorganisms. A clear example is the microbiome of the human body, which has been estimated to contain over 1000 different bacterial species in the gut only (Qin, 2010). Within these communities, bacteria establish different kinds of interactions, ranging from cooperativity to competition. Within these communities, individuals from different species signal each other (Bassler, 2002; Keller and Surette, 2006), compete for nutrients (Ghoul and Mitri, 2016), and produce substances that benefit other species in the community (West et al., 2007; Celiker and Gore, 2013). A particularly relevant situation in which interaction among bacterial strains has been seen to be important is in their response to antibiotics (Frost et al., 2018). In these conditions, mixed-species communities have been seen to exhibit, for instance, spreading of antibiotic resistance (Gerardin et al., 2016; Beardmore et al., 2018) and cross-protection against multiple antibacterial agents (Yurtsev et al., 2016). But while it is recognized that the reaction of mixed-species communities to antibiotics cannot be directly inferred from dose-response studies in isolated species (Beardmore et al., 2018), the ways in which interactions between the species modulate those responses are still poorly understood (Fig. 5.1).

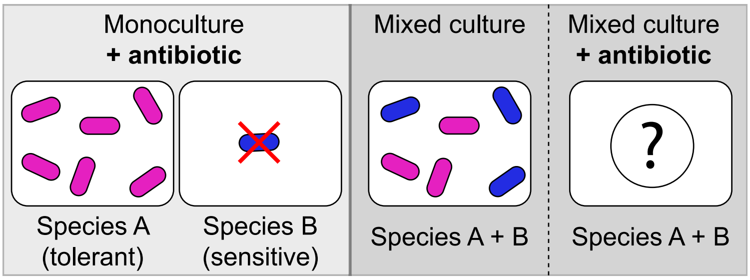

Figure 5.1: Antibiotic response for mono-cultures and mixed-cultures. Cartoon illustrating the question of whether we can extrapolate the antibiotic response of single-species mono-cultures to that of mixed-species co-cultures.

5.2 Beta-lactam action

As we mentioned in the Introduction 1.4, penicillin-binding proteins (PBPs) are membrane proteins responsible for the formation of the bacterial cell wall. The biosynthesis of this wall, which mainly consists of a matrix of peptidoglycans, is achieved by two enzymatic processes: transglycosylation of the glycan chains and transpeptidation between the different chains. β-lactam antibiotics, such as ampicillin, penicillin, and carbenicillin, target the final transpeptidation, which creates an imbalance between production and hydrolization of the cell wall, disrupting the cell shape and eventually causing lysis and death. Specifically, this antibiotic diffuses into the cell wall and competitively inhibit the crosslinking of the peptidoglycans, by binding to PBPs through the β-lactam ring and forming a covalent bond (acylation) with the active site of the target protein (Drawz and Bonomo, 2010).

Studies in single bacterial species have revealed, especially in recent years, a great deal of information of how β-lactams interfere with the microbial physiology (Novák et al., 2000; Miller et al., 2004; Kohanski et al., 2007; Tan et al., 2012; Foti et al., 2012; Dwyer et al., 2014; Belenky et al., 2015). These insights have provided, in turn, information of how bacteria evade the inhibitory effect of this drugs, either by genetic means through the development of antibiotic resistance (Toprak et al., 2011; Palmer and Kishony, 2013), or phenotypically through modulation of the cellular metabolic rate exhibited, for example, by persister cells (Balaban et al., 2004; Lee et al., 2018; Vulin et al., 2018). A distinct survival response at the phenotypic level involves what is known as *antibiotic tolerance*, which allows populations to regrow after a certain lag time, once the treatment has subsided (Fridman et al., 2014; Srimani et al., 2017). In this Chapter, we use this phenotypic characteristic, in particular, the dependence of the duration of lag time on the antibiotic concentration, as a marker whose behavior varies qualitatively between different bacterial species with distinct sensitivities to the administered drug. With this purpose, we selected *Bacillus subtilis* and *Escherichia coli*, which have opposing responses to the β-lactam antibiotic ampicillin: *Bacillus subtilis* is known to present tolerance to this antibiotic, *Escherichia coli* is sensitive to it.

We began by examining systematically the behavior of a population of *B. subtilis* NCIB 3610 cells in 96-well plates containing increasing concentrations of five different types of antibiotics. The results are shown in Fig. 5.2, which plots the cell density of the different liquid cultures, as monitored by the absorbance (optical density, OD) of the culture at 600 nm.

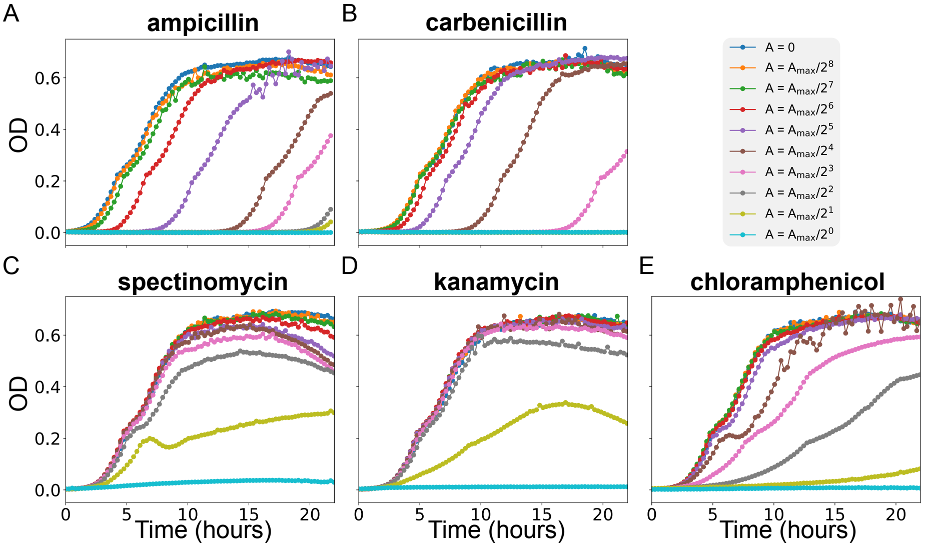

Figure 5.2: *B. subtilis* antibiotic response. Response of *B. subtilis* strain NCIB 3610 to five different antibiotics as a function of the antibiotic concentration. The maximum concentrations for the different cases are: (A) ampicillin, $A_{\text{max}} = 25$ μg/ml, (B) carbenicillin, $A_{\text{max}} = 25$ μg/ml, (C) spectinomycin, $A_{\text{max}} = 50$ μg/ml, (D) kanamycin, $A_{\text{max}} = 3$ μg/ml, and (E) chloramphenicol, $A_{\text{max}} = 5$ μg/ml.

A maximal concentration A_{max} is selected in each case such that no growth is observed in our observation period (22 hours in this case). We further consider eight serial halving dilutions, together with the baseline antibiotic-free case as a reference. The different antibiotics considered here include two compounds of the β-lactam family (ampicillin and carbenicillin, Figs. 5.2A,B), which attack bacteria by interfering with membrane formation, while the other three (two aminoglycosides, spectinomycin, and kanamycin, Figs. 5.2C,D, plus chloramphenicol, Fig. 5.2E) affect protein synthesis by targeting the ribosome function. The effects of the five antibiotics cluster according to their type. The aminoglycosides (Figs. 5.2C,D) display a somewhat abrupt response that kicks-in only when the antibiotic concentration is large enough. Chloramphenicol scales the growth curve approximately uniformly along time, with the overall growth rate diminishing gradually as the antibiotic concentration increases. In contrast, β-lactams induce a delayed response that scales exclusively in time as the antibiotic concentration changes, with consistent growth rate (even through the diauxic shift occurring at OD ~ 0.2, which is also observed for the other antibiotics). This lag response is consistent with bacterial tolerance (Levin et al., 2017) and provides us with a quantitative phenotype that we use extensively in what follows.

To study how general is the delayed growth response elicited by ampicillin on *B. subtilis*, we also studied the effect of that antibiotic in the laboratory strain PY79 (Fig. 5.3A). Note that we now focus only on the growth turn-on, and that the slope of the growth curve seems larger than in Fig. 5.2 due to the increased range of the x-axis with respect to the last plot. As in the case of 3610, the result shown in Fig. 5.3A indicates that PY79 also has a strong tolerance even for large antibiotic concentrations of ampicillin. In the rest of this Chapter, we will work with the PY79 strain.

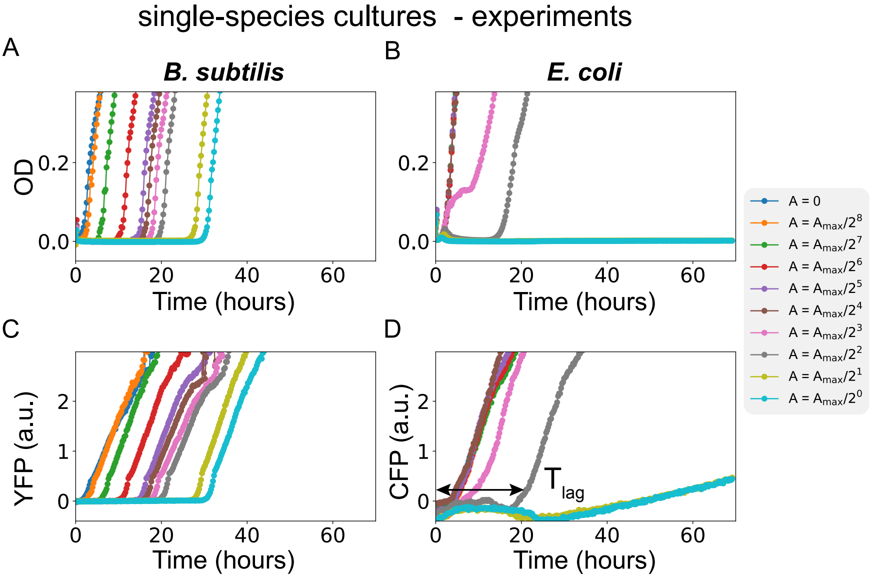

Figure 5.3: Single-species antibiotic response. A) OD as a function of time (hours) in presence of increasing concentrations of ampicillin for the *B. subtilis* strain PY79 during 70 hours of observation. B) OD as a function of time (hours) in presence of increasing concentrations of ampicillin for *E. coli* strain MG1655. The maximum antibiotic concentration in panels (A) and (B) is $A_{\max} = 50\ \mu$g/ml and the other values correspond to a two-fold dilution, except the last one that corresponds to $A_{\max} = 0\ \mu$g/ml. C) Corresponding YFP signal (a.u.) for panel (A). D) Corresponding CFP signal (a.u.) for panel (B).

The behavior of *B. subtilis* contrasts markedly with the response of *E. coli* to the same antibiotic. As shown in Fig. 5.3B, the response of the gram-negative species is abrupt and devoid of any delayed growth response. Given the strong qualitative difference between the responses of the two species to the same antibiotic, we decided to use this response as a marker to study the influence of cross-species interaction to antibiotics challenge in a mixed-species community. In order to distinguish the two bacterial species in the upcoming co-culture experiments, we tagged them with different fluorescent proteins, with *B. subtilis* expressing YFP, and *E. coli* CFP.

Panels C and D from Fig. 5.3 show the corresponding signal from the two fluorescence reporters in each case, evidencing a correspondence with the OD measurements shown in panels A and B. We then used the fluorescence signals to calculate the lag time T_{lag}, defined as the time that the population takes to start growing after antibiotic addition (see double-headed arrow in Fig. 5.3D). We calculated this quantitatively by fitting the fluorescence signal between 1.0 and 1.5 arbitrary units to a line, and determining the intercept of that line with the horizontal axis. The corresponding lag times as a function of antibiotic concentration are plotted in Figs. 5.4A,B for the two bacterial species, and show the progressive response of *B. subtilis* to ampicillin, which again contrasts with the abrupt response of *E. coli*. The response of the latter reveals to be very sensitive to high concentrations of antibiotic, with no growth observed within our 70-hour observation window in those cases.

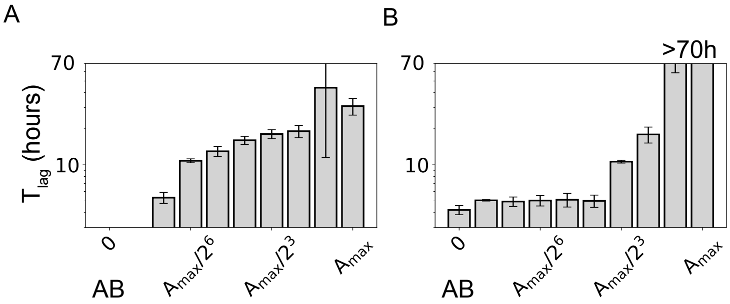

Figure 5.4: Quantification of the lag time. A) Lag time T_{lag} for the different concentration of antibiotic plotted for Fig. 5.3C and D, respectively. B) Lag time T_{lag} plotted for Fig. 5.3B. Error bars represent standard deviation over four replicates, two biological replicates with two technical replicates each.

5.3 Chemical kinetics of the response in monocultures

As mentioned in the Introduction1.4, the β-lactam antibiotic ampicillin interferes with bacterial growth by binding and inactivating membrane precursor proteins, specifically penicillin-binding proteins (PBPs), which are involved in cell wall production. In that way, the drug causes an imbalance in the metabolism of the cell wall, which results, in turn, in cell lysis (Luo and Helmann, 2012).

The chemical processes underlying PBP inhibition can be described by the following reaction scheme (Zapun et al., 2008):

$$\mathrm{P} + \mathrm{A} \xrightleftharpoons[k_2]{k_1} \mathrm{P{\cdot}A} \xrightarrow{\gamma} \mathrm{P} + \mathrm{I}\,, \tag{5.3.1}$$

where P stands for free PBP, and A for free ampicillin. The processes of binding and unbinding of the complex have rates k_1 and k_2, respectively. The symbol I represents the inactivated form of the compound that results from the hydrolyzation of the covalent complex P·A formed by the antibiotic and PBP. This hydrolyzation process is slow, occurring at a rate (γ) lower than bacterial division (Zapun et al., 2008). Notice that the binding between P and A is considered to be much stronger than the unbinding (Lu et al., 2001).

The kinetics of the reactions described in the reaction scheme 5.3.1 can be described by the following pair of ordinary differential equations:

$$\frac{dP}{dt} = (k_2 + \gamma)(P_t - P) - k_1 P A\,, \tag{5.3.2}$$

$$\frac{dA}{dt} = k_2(P_t - P) - k_1 P A\,, \tag{5.3.3}$$

where total amount of PBP in the cell is assumed to be conserved ($P_t = P + [P{\cdot}A]$). The behavior of this system for parameter values corresponding to the case of *B. subtilis* is given in Fig. 5.5.

The figure shows a typical trajectory of the system (black line) in the phase space defined by free PBP (P) and free antibiotic (AB, A), for an initial condition $P = P_t$ and an initial AB concentration $A = A_t = 70$ μM (empty circle). Starting from that initial state, the AB quickly eliminates almost all free PBP (portion of the trajectory labeled as 1 in Fig. 5.5), until the trajectory hits the P-nullcline (green line):

$$\frac{dP}{dt} = 0 \implies A_p = \frac{k_2 + \gamma}{k_1} \frac{P_t - P}{P}\,, \tag{5.3.4}$$

which is slightly above the A-nullcline (dashed magenta line in Fig. 5.5A):

$$\frac{dA}{dt} = 0 \implies A_p = \frac{k_2}{k_1} \frac{P_t - P}{P}\,. \tag{5.3.5}$$

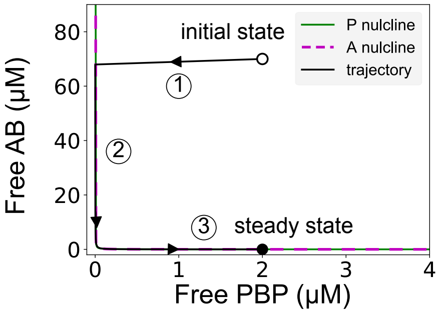

Figure 5.5: Dynamics of the PBP-ampicillin system (5.3.2)-(5.3.3). Sample trajectory (black line) in the phase space defined by the two variables P and A. The two nullclines of the system are shown in solid green and dashed magenta lines. Three portions of the trajectory are marked with numbers. The model parameters are: $k_1 = 0.15$ $(\mu\text{M}\cdot\text{s})^{-1}$, $k_2 = 0.0015$ s^{-1}, $P_t = 2\,\mu$M, and $\gamma = 5 \cdot 10^{-4}$ s^{-1}.

When the trajectory hits the P-nullcline, A starts decreasing, but it does so very slowly, as can be seen by substituting Eq. (5.3.4) into Eq. (5.3.3), which leads to:

$$\frac{dA}{dt} = -\gamma(P_t - P) \approx -\gamma P_t\,, \tag{5.3.6}$$

given that P is much smaller than P_t at this point. The corresponding time traces for P and A are shown in panels A and B of Fig. 5.6, respectively. Panel B, in particular, shows the linear decrease of A in time in portion 2 of the trajectory. In that part of the trajectory, the non-exponential (slow) decay of A allows us to assume that the total amount of concentration available to P is approximately constant in the timescale of P, whose dynamics still contains an exponential (fast) decay term:

$$A_t = A + [P{\cdot}A] = A + P_t - P \approx \text{constant} \implies A = A_t - P_t + P\,. \tag{5.3.7}$$

Substituting Eq. (5.3.7) into Eq. (5.3.2), and calculating the steady state of that equation leads to the stationary value of the free PBP as a function of the total AB concentration A_t:

$$P_{\text{st}} = \frac{1}{2k_1}\Bigg(-(k_2 + \gamma + k_1(A_t - P_t)) \\ + \sqrt{(k_2 + \gamma + k_1(A_t - P_t))^2 + 4k_1(k_2 + \gamma)}\Bigg)\,. \tag{5.3.8}$$

In the limit of quasi-irreversible binding between A and P, given by $k_2 \ll k_1 P_t$, the amount of free PBP depends on total antibiotic concentration

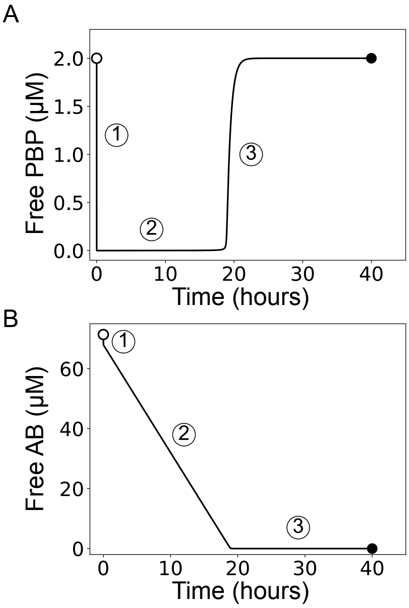

Figure 5.6: Dynamics of the free PBP and free AB. A) and B) display the time traces of PBP (P) and free antibiotic (A), respectively, corresponding to the trajectory shown in Fig. 5.5 (same parameters). Notice that the numbers in the trajectories correspond to the three phases indicated in Fig. 5.5.

in a threshold-linear manner, as shown in Fig. 5.6A. This behavior results from the fact that the antibiotic acts as a *titrating molecule* that leaves no free PBP as long as $A_t > P_t$, whereas once A_t decreases below P_t PBP builds up linearly. Around $A_t \sim P_t$, this molecular titration leads to an *ultrasensitive response* (Buchler and Louis, 2008).

The threshold-linear response of free PBP with respect to the instantaneous total AB concentration can explain the delayed growth behavior observed experimentally. First, we consider that growth occurs when free PBP is larger than a certain threshold (shown by the horizontal dashed line in Fig. 5.7). Next, we take into account that the total concentration of available antibiotic decays slowly (linearly) in part 2 of the system trajectory (as shown in Fig. 5.6B). Under these two conditions, we can envisage that starting from a certain antibiotic level larger than P_t, the population will initially not grow (PBP is below threshold), but as AB decreases (horizontal left-ward arrows in Fig. 5.6B) according to Eq. (5.3.6), eventually (and suddenly) free PBP will go above the growth threshold, and the population will start proliferating. The time needed for the threshold to be crossed naturally depends on the initial AB concentration. Furthermore, the difference between the two bacterial species can be accounted for by considering different amounts of total PBP, P_t (compare the black and blue lines in Fig. 5.7). Additionally, we can account for the higher sensitivity of *E. coli* by assuming that the decay rate γ is smaller in that species than in *B. subtilis*.

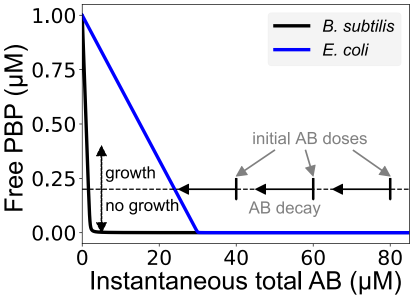

Figure 5.7: Dynamics of the PBP-ampicillin system for *B. subtilis* and *E. coli*. Amount of free PBP as a function of total antibiotic concentration A_t, for *B. subtilis* (black line) and *E. coli* (blue line), given that A varies slowly (which happens in portions 2 and 3 of the trajectory shown in Fig. 5.5). The model parameters for *B. subtilis* correspond to the ones used in the previous figures. For *E. coli*, the modified parameters are $P_t = 30\,\mu$M and $\gamma = 6 \cdot 10^{-6}$ s^{-1}.

Our expectations regarding the behavior of the dynamical system (5.3.2)-(5.3.3) are confirmed in Fig. 5.8. The figure compares the growth dynamics of the two bacterial species, resulting from assuming a simple logistic growth in the two cases, with a growth rate that depends on the amount of free PBP:

$$\frac{d\rho}{dt} = \left(\mu_0 + \mu \frac{P^n}{k_p^n + P^n}\right) \rho(1-\rho)\,. \tag{5.3.9}$$

Here, the cell density ρ is normalized by the carrying capacity of the medium, and the growth rate depends on the free PBP in a switch-like manner, with threshold k_p (corresponding to the horizontal dashed line in Fig. 5.7) and effective cooperativity n. The coefficient μ_0 represents the basal growth rate in the total absence of PBP, which is considered negative (net death) since PBP is necessary for cellular proliferation.

In Fig. 5.8, the dynamics of the cell density $\rho(t)$ for both bacterial species are shown in panels A and B, as resulting from the parameter choices given in the caption of Fig. 5.5. The corresponding dynamics of free antibiotic are plotted in panels C and D, which show that AB decays much faster in *B. subtilis* than in *E. coli*.

Finally, we compute the lag time (T_{lag}) by following a method similar to that used in the experiments, applying it directly to ρ: the values of $\rho(t)$ between 0.4 and 0.5 were fitted to a line, and the intercept of that line with the horizontal axis was identified as T_{lag}. The result is shown in Fig. 5.9A and B for the two bacterial species, and confirm the gradual tolerant response of *B. subtilis*, and the abrupt increase in sensitivity of *E. coli*, for increasing AB levels.

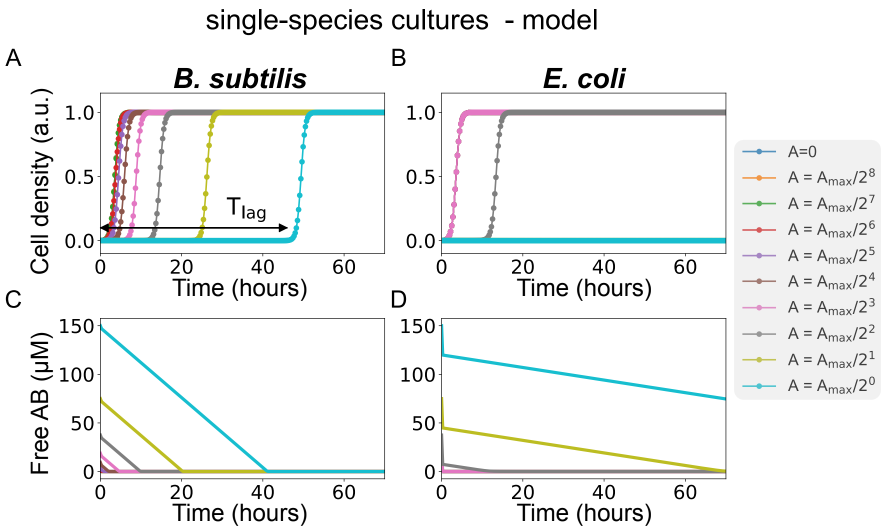

Figure 5.8: Growth dynamics of the molecular titration model of species in isolation. A and B) Dynamics of the cell density resulting from the logistic equation (5.3.9) for *B. subtilis* (left), and *E. coli* (right). C and D) Corresponding temporal behavior of the free antibiotic. Parameters are those of Fig. 5.5, plus $k_p = 0.2\ \mu$M, $n = 2$, $\mu = 6 \cdot 10^{-4}$ s, and $\mu_0 = -\mu/10$. The maximum antibiotic concentration is $A_{\max} = 150\ \mu$M.

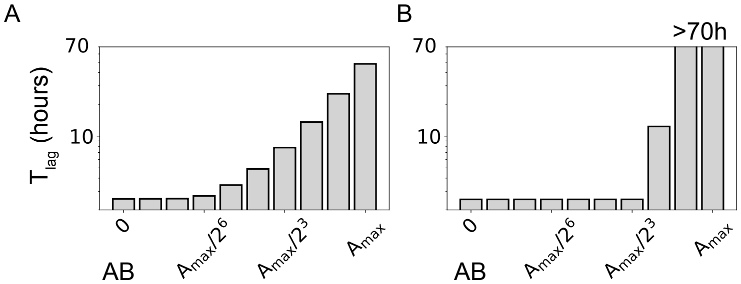

Figure 5.9: Lag time from the molecular titration model. A and B) Lag time to grow as a function of the initial antibiotic concentration for *B. subtilis* (left), and *E. coli* (right), corresponding to Fig. 5.8A and B, respectively (same parameters).

5.4 Modeling the response of a mixed-species community to increasing antibiotic dosage

In the simplest scenario, the way in which *B. subtilis* and *E. coli* would interact when cultured together is by sharing the available antibiotic. Using the principle of parsimony, we assume that the antibiotic diffuses between the bacteria and the extracellular medium, at equal rates for the two species, and the diffusion instantaneously equilibrates between the two spatial locations. This is represented mathematically by:

$$\frac{dA_s}{dt} = k_2(P_t - P_s) - k_1 P A_s - k_a(A_s - A_c)\,, \tag{5.4.1}$$

$$\frac{dA_c}{dt} = k_2(P_t - P_c) - k_1 P A_c - k_a(A_c - A_s)\,, \tag{5.4.2}$$

where the subindices s and c denote that the variables correspond to the *B. subtilis* and *E. coli* populations, respectively. K_a corresponds to the effective diffusion between the bacteria and the medium.

Adding to these equations the corresponding ones for the concentrations of PBP and the densities of the two bacterial species leads to a model of the mixed-species community, whose dynamics is depicted in Fig. 5.10.

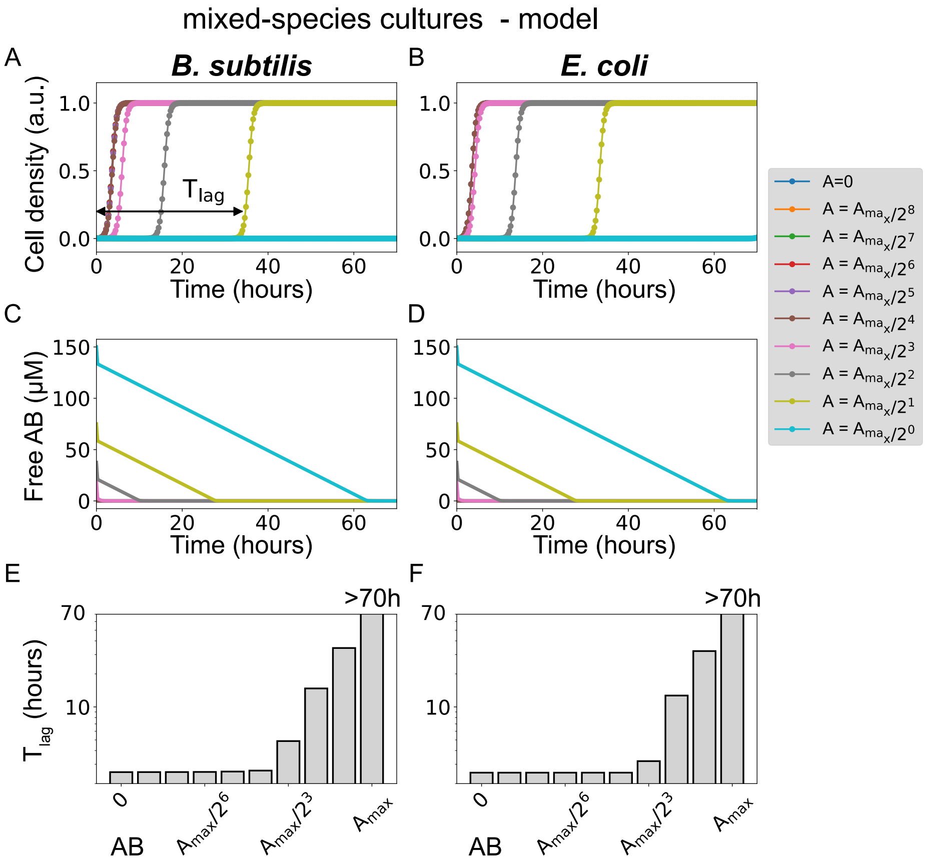

Figure 5.10: Growth dynamics of the molecular titration model in the case of a mixed-species community. A and B) Dynamics of the cell density for *B. subtilis* (left), and *E. coli* (right). C and D) Corresponding temporal behavior of the free antibiotic. E and F) Lag time as a function of the initial antibiotic concentration. Parameters are those of Fig. 5.8, plus $k_a = 0.2$ s^{-1}. The maximum antibiotic concentration is $A_{\max} = 300\ \mu$M.

The figure shows that the coupling between the two species occurs via sharing of the free AB in the system, which now decays at an intermediate rate with respect of the situation exhibited by the two species in isolation (compare with Fig. 5.8). As a result, the two species have an AB dependence of the T_{lag}, that is intermediate between the two extreme behaviors exhibited in isolation and shown in Fig. 5.9.

Figure 5.11 compares the two situations by plotting the difference in lag times, $\Delta T_{\text{lag}} = T_{\text{lag}}(\text{mixed}) - T_{\text{lag}}(\text{single})$, as a function of the AB level.

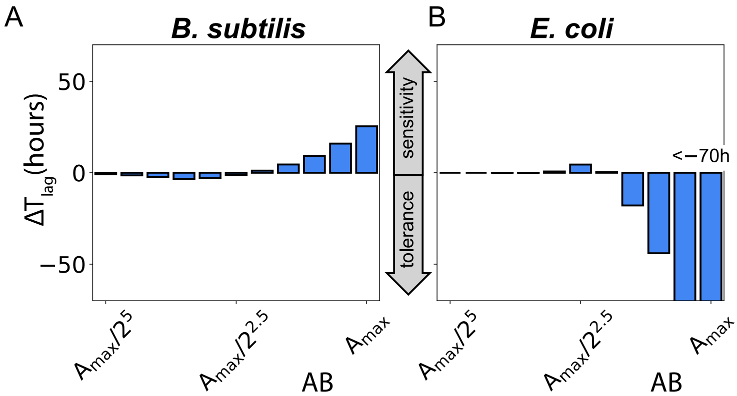

Figure 5.11: Predicted sensitivity swap in co-culture. Lag time difference ($\Delta T_{\rm lag}$) between the mixed-species and the single-species conditions for *B. subtilis* (left), and *E. coli* (right). Same parameters as in Fig. 5.10.

$\Delta T_{\rm lag}$ is defined such that a positive value indicates a delay in population growth in the presence of the other species, and thus an increase in the sensitivity of the corresponding species to the antibiotic. In contrast, a negative value of $\Delta T_{\rm lag}$ corresponds to an advance in the growth, and thus an increase of the tolerance of that species (see wide vertical arrows between the two panels of the figure). The figure shows clearly that, according to the model, *B. subtilis* should become more sensitive to high levels of antibiotic when co-cultured with *E. coli*. Conversely, *E. coli* should become more tolerant to high levels of antibiotics when co-cultured with *B. subtilis*. This contrasts with previous studies that report mutual cooperation between different species (Yurtsev et al., 2016) in the presence of antibiotics, or mutual competition (Ghoul and Mitri, 2016). Here, the effect of cross-species interaction is asymmetric for the two species.

5.5 Antibiotic sensitivity swap in mixed-culture conditions

We now test the model's expectation that the interaction between *B. subtilis* and *E. coli* in a mixed-species community leads to an exchange in the tolerance of the two species to increasing amounts of antibiotic. To that end, we co-cultured the two species and measured their growth by monitoring the emission from their respective fluorescence markers. As shown in Fig. 5.12A, in the presence of *E. coli*, *B. subtilis* cells experience a substantial increase in sensitivity, which jumps abruptly as the AB levels increase (already for the smallest AB levels that we tested). This contrasts

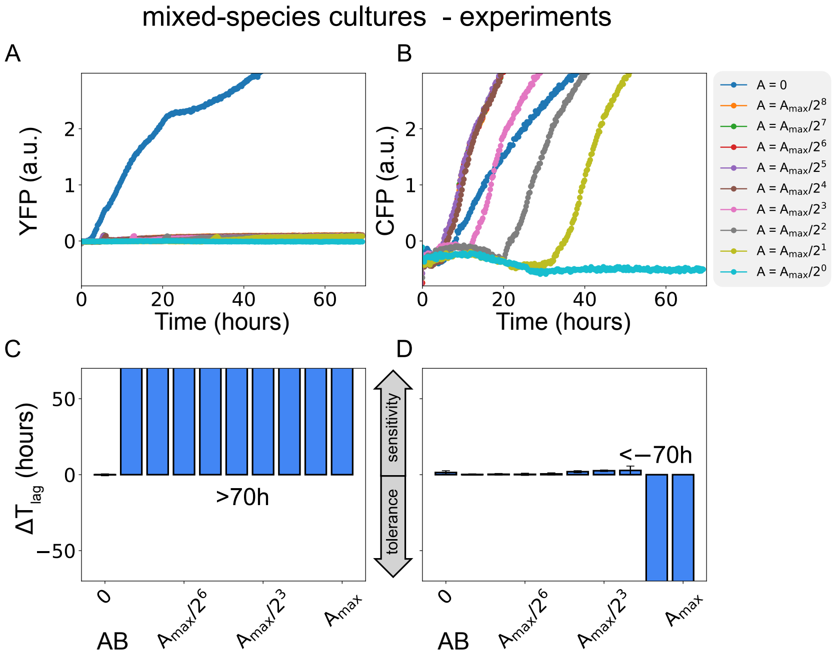

Figure 5.12: Experimental observation for the co-cultures. A and B) show the emission of the fluorescence markers reporting on the two species, YFP for *B. subtilis* (panel A) and CFP for *E. coli* (panel B). C and D) show the corresponding lag time differences (ΔT_{lag}) as a function of the initial antibiotic concentration, for a maximum value $A_{\mathrm{max}} = 100\ \mu$g/ml.

with the delayed growth response displayed by *B. subtilis* in isolation, with a lag time that increases gradually with the antibiotic level (Fig. 5.3A). In turn, *E. coli* populations behave now, in the presence of *B. subtilis* cells, in a more tolerant manner to high concentrations of antibiotic, and exhibit in some cases a gradual increase in lag time (Fig. 5.12B). Once more, this behavior contrasts with the sensitive response of *E. coli* to ampicillin in isolation (Fig. 5.3B).

We quantify this sensitivity swap in Figs. 5.12C,D, where the lag time differences (ΔT_{lag}) between the mixed- and single-species experiments are plotted for the two species. Bars labeled "> 70 h" and "< -70 h" denote cases in which one or several of the experimental replicates do not show growth within the 70-hour observation period in the mixed and single cases, and do show growth in the opposite situations.

The population measurements discussed above were confirmed by microscopy, as shown in Fig. 5.13.

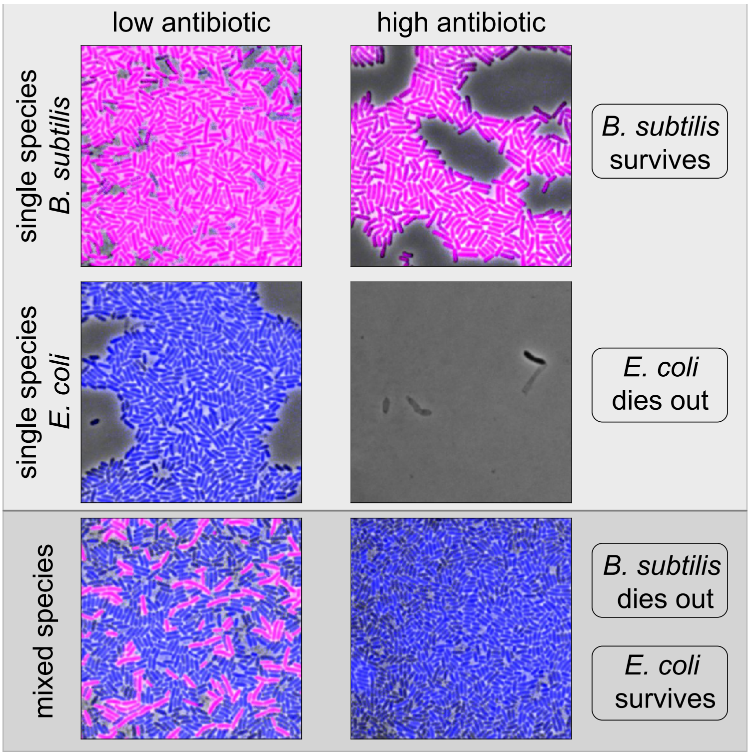

Figure 5.13: Snapshots for the antibiotic response of mono-cultures and mixed-cultures. Combined phase and fluorescence microscopy images taken 48 hours after the beginning of the experiment, for antibiotic concentrations of 0.39 μg/ml (left column) and 25 μg/ml (right column). The upper row corresponds to an isolated *B. subtilis* culture (magenta color corresponds to YFP signal), the middle row to an isolated *E. coli* culture (blue color corresponds to CFP signal), and the bottom row to a mixed co-culture. Notice that for a correct comparison in the mixed-species culture, we would need to consider the case of 50 μg/ml of ampicillin, to compensate the doubling in the concentration of bacteria in the media.

As it can be seen in the figure, while *B. subtilis* in isolation is tolerant to high AB concentrations after 48 hours of culture (top row), *E. coli* is sensitive after that same time to the same concentration of antibiotic. In contrast, in the mixed-culture it is *E. coli*, and not *B. subtilis*, the bacterial species that survives the antibiotic treatment. Then, the presence of antibiotic in the media creates a new configuration of the community, where the sensitive species displaces the tolerant, and this phenomenon can be simply explained by titration and sharing of the antibiotic.

5.6 Discussion

The results discussed in this Chapter show that the sensitivity trends to ampicillin in co-cultures of *B. subtilis* and *E. coli* cells are reversed with respect to the situation observed when the bacteria are cultured in isolation. This behavior can be understood in terms of a minimal mathematical model of the binding of the β-lactam antibiotic to PBP, and the posterior active inactivation of the antibiotic. The model is generic and only requires changes in two parameter values to describe the observations in the two mono-cultures, specifically the gradual increase in time lag to growth of *B. subtilis* with respect to the antibiotic level, characteristic of a tolerant response, and the sudden jump in sensitivity exhibited by *E. coli* when the antibiotic concentration surpasses a threshold value. This threshold behavior results from an ultrasensitive response caused by the quasi-irreversible binding of the antibiotic to PBP, which occurs in *E. coli* but not appreciably in *B. subtilis*, where the critical antibiotic concentration is vanishingly small. The gradual dependence of the lag time in *B. subtilis* on the antibiotic levels, as well as the sensitive response of *E. coli* to large amounts of antibiotic, is reproduced by assuming that the inactivation of the antibiotic by PBP occurs at a much smaller rate in the latter than in the former.

Our minimal model makes the unexpected prediction that the sensitivity patterns described swap in co-culture. This swap is explained by the sharing of antibiotic among the two species. *B. subtilis* degrades the antibiotic that would inhibit the growth of *E. coli*. In turn, *E. coli* acts as a buffer that delays the degradation of the antibiotic and thus enables an increased inhibition of the growth of *B. subtilis* at lag times for which the antibiotic would have already been lost if *B. subtilis* were by itself. Experiments confirm the expectations coming from the model, showing, in fact, a more dramatic sensitivity swap than the one anticipated by the model. This can be ascribed to the simplicity of our assumptions, which include a symmetric response to the antibiotic by the two bacterial species, at the levels of both PBP binding (where we assume equal rates k_1 and k_2) and antibiotic uptake (where we consider equal diffusion coefficients). We also assume simple diffusion between the intracellular and extracellular media, although the results should be robust to changes in the way in which the antibiotic is imported and exported in both cell types. Moreover, the model does not consider other possible interactions between the species, such as competence for nutrients and space, which could influence the frequencies of the species, as can be observed in the lowest antibiotic concentration (Fig. 5.13). Obtaining a better quantitative fit to the model this thus would require extra assumptions, for example regarding the molecular mechanisms through which ampicillin interacts with the two bacterial species considered here, assumptions that in most cases cannot be corroborated with our current knowledge. For those reasons, we decided to keep our model as simple and parsimonious as possible.

Altogether, the results shown in this Chapter indicate that the population level responses of isolated bacterial species to antibiotics may not be directly transferred to situations in which these species coexist with others in mixed communities. Given the ubiquity of multi-species bacterial consortia, it might be advisable to revise our approaches to the characterization of how antibiotics affect bacterial physiology and how bacterial cells evade those effects.

5.7 Appendix

5.7.1 Experimental methods

Bacterial strains and cultures

The *B. subtilis* strains used in this Chapter are listed in Table 5.1. PY79 strain expresses YFP from the inducible promoter $P_{\text{hyperspank}}$. The high-copy number plasmid pSB1C3, containing the promoter BBa_K880005 (Galdzicki et al., 2011) controlling the expression of CFP, was transformed into the *E. coli* MG1655 strain.

Table 5.1: Strains used in this study.

Strain	Genotype	Source
E. coli CFP	*E. coli* K-12 MG1655	This study
B. subtilis Wild-type	*B. subtilis* NCBI 3610	Gürol Süel, UCSD
B. subtilis YFP	*B. subtilis* PY79	Süel et al. (2007)

For overnight liquid cultures, cells were grown at 37°C in Luria Broth (LB, Miller's modification) in an incubator with shaking. Appropriate antibiotics for selection were added to the following final concentrations: 10 μg/ml spectinomycin and 10 μg/ml chloramphenicol. The next day, the cultures were diluted to a final OD_{600} of 0.1 with the corresponding antibiotics, and cells grown at 37°C with shaking. After 2hours, temperature was switched to 30°C and cells continue growing for 2 hours more. The saturated culture was diluted to OD_{600} of 0.1 and, if required, IPTG was added with final concentration of 1 mM. Cells were grown 2 hours at 30°C.

5.7.2 Plate reader measurements

For the plate reader measurements we used 96-well black microwell plates with clear lid (Nunc, Denmark). A serial two-fold dilution of selected antibiotic was prepared, starting by the corresponding maximum concentration (100 μg/ml or 25 μg/ml ampicillin, 25 μg/ml carbenicillin, 50 μg/ml kanamycin, and 50 μg/ml spectinomycin) in a final volume of 150 μl per well. One well per condition was used as a control without antibiotics, and another well was used as a blank. IPTG was added to a final concentration of 1 mM, if needed. Finally, an inoculum of bacteria was added to a final OD_{600} of 0.01.

The measurements were acquired on a microtiter plate reader Tecan Infinite M200 pro (Tecan Group Ltd., Switzerland). The temperature was set at 30°C with linear shaking. The absorbance wavelength for OD was set at 600 nm. Measurements were made every 15 minutes.

Each condition had two biological replicates (taken in two experiments in different days) with two technical replicates each, for a total of four replicates.

5.7.3 Microscopy

The samples were obtained by taking 2.5 μl of the liquid culture and spotting them onto low melt agarose pads, after 48 hours of the initiation of the experiment. The agarose pads were placed afterwards into coverslip-bottom Willco dish for imaging. The snapshots were acquired with a fluorescent microscope with a 100x objective.

Part III

Conclusions

Chapter 6

Final conclusions and future perspectives

In recent years, thanks to the introduction of new microscopy techniques and molecular approaches, large progress has been made towards understanding the processes governing bacterial cell proliferation. However, the majority of these studies have been performed under constant conditions, and our knowledge about the dynamical aspects of the regulation still remains limited. In this Thesis we have focused on the main facets of bacterial growth, namely cell cycle, biomass production, and membrane stability, to study some examples of how dynamics, at different levels, can affect to these principal processes.

6.1 Co-entrainment between the cell cycle and an oscillatory gene-based circuit

We have first studied at the single-cell level the interaction between the bacterial cell cycle and a robust synthetic oscillator in *E. coli*, as a proxy of a natural oscillatory process. Our results have shown that the cell cycle can partially entrain oscillations of the synthetic circuit, but only in the situation where the synthetic oscillator couples back into the cell cycle (via the RIDA system), is when the two periodic processes become significantly co-entrained. A minimal computational model, constrained by the experimental observations regarding the statistical properties of the oscillators, allows us to confirm the effect of a stronger co-entrainment through back-coupling.

For this study we have used a synthetic oscillator that is contained into two plasmids, independent of the regulation of chromosomal replication. But, cells have their natural oscillators integrated into their chromosome. Then, the lack of control upon the number of copies of the synthetic circuit makes it difficult to directly infer the effect of entrainment from the cell cycle to other natural oscillators. For future work, it would be interesting to study the effect of the chromosome replication in an integrated synthetic oscillator, as well as the entrainment that the latter could produce back to the cell cycle. Separately, the period of the cell cycle can be modified by external factors, such as temperature and nutrients. It would thus be interesting to study the effect of modifications of the cell cycle period on the co-entraiment.

Although this study is focused on the interaction between the bacterial cell cycle and a synthetic oscillator, the idea that the periodic doubling of genes due to the chromosomal replication must affect other oscillators inside the cell should apply to all organisms. In fact, after the publication of our results, other publications have shown new examples demonstrating the gating of the circadian rhythm by the cell cycle (Paijmans et al., 2016; Liu et al., 2017a). Finally, our results can be relevant for synthetic biology, providing new insights about the design of gene-based circuits and synchronization between cellular processes, especially with the bacterial cell cycle.

6.2 Magnesium content determines the tolerance of bacteria to ribosomal stress

In Chapter 4, we have seen an intriguing connection between ion flux in bacterial cells and their antibiotic tolerance upon ribosomal stress. By measuring membrane potential dynamics, growth rate, and survival of *Bacillus subtilis* cells, we found two groups of cells: (i) growth defective cells that exhibit a transient decrease in membrane potential (hyperpolarization), followed by cell death, and (ii) growing cells that lack hyperpolarization events and tolerate the stress. This cell-to-cell heterogeneity in the tolerance arises from an imbalance in ion flux. Specifically, by combining proteomic analysis and genetic perturbations that alter ribosome structure, we uncovered that growing bacteria tolerate aminoglycosides (ribosome-targeting antibiotics) through stabilization of the ribosomes by magnesium ions.

Our results show that the membrane potential of bacteria appears to be a reliable marker for their sensitivity to ribosomal stress. Specifically, membrane potential measurements can determine whether a given bacterial population has a low or high tolerance to aminoglycosides. New methods to test the bacterial response to antibiotics could thus be developed that do not require measurements of survival or killing efficiency. In other words, the bacterial membrane potential measurement could quickly identify the stress sensitivity of a bacterial population from a single snapshot.

Uncovering ion-flux based differences in bacterial survival under antibiotic response also suggests ways to increase the effectiveness of known antibiotics, especially aminoglycosides that target the ribosomal complex. Specifically, combining antibiotics with drugs that target bacterial membrane proteins that are responsible for magnesium ion influx, such as MgtE, could enhance the killing efficiency of these antibiotics. Since ion flux is critical to all cells, one of the main challenges will be to design drugs that specifically target bacterial ion transporters, in an effort to reduce unwanted side-effects to host cells. However, there are multiple unique properties of bacterial cell walls and membranes, such as their composition and content of membrane proteins, lipids, and polysaccharides (Sharma et al., 2012; Kwon et al., 2017), suggesting possible alternative ways to achieve such specific targeting of bacterial ion transporters.

Finally, the alarmone ppGpp, which has been linked to stress, such as amino acid starvation and persistence during antibiotic treatment, is a key regulator of the ribosome biogenesis and degradation. For future studies, it would be interesting to investigate whether this molecule could affect the relationship between ribosomes and magnesium content, since its activity has been already linked to this ion (Sajish et al., 2007; Zhang et al., 2018).

6.3 Antibiotic tolerance swap in bacterial co-culture

In Chapter 5, we have studied the response of the two bacterial species, namely *Bacillus subtilis* and *Escherichia coli*, to the β-lactam antibiotic ampicillin, both in isolation and when cultured together in mixed communities. First, we have seen that the effect of increasing ampicillin concentrations on the two species in isolation is markedly different from each other. Specifically, *B. subtilis* exhibits a delayed tolerance, characterized by exponential growth after a time lag that increases gradually with the antibiotic concentration. In contrast, *E. coli* displays an abrupt jump in sensitivity as the antibiotic concentration increases. We have reproduced these two behaviors with a minimal mathematical model of the interaction between the antibiotic and its molecular target within both cell types, the penicillin-binding proteins (PBPs). Importantly, the model anticipates that when the two species coexist, their sensitivity swaps for large ampicillin concentrations, with *B. subtilis* becoming more sensitive and *E. coli* more tolerant. The effect is corroborated experimentally, indicating that our extensive knowledge of how single bacterial species respond to antibiotics might not be directly applicable to more natural mixed microbial ecosystems.

Research studies of mixed-species bacterial communities are scarce. However, our results suggest that it might not be warranted to fully extrapolate the conclusions obtained from single-species dose-response studies to the case of mixed-species bacterial populations, arguing instead for a community-specific analysis in each case. Future goals could therefore be the study of more diverse cultures with different bacterial species, to explore mechanisms that bacteria can use to survive antibiotic treatments.

To conclude this Thesis we would like to highlight the importance of continuing to perform basic research on the dynamical regulation of bacterial proliferation, not only for the control of infections but also to understand how the different bacterial species are maintained in time in their natural habitats (such as in the microbiome) and how they interact. We expect that our work will inspire new studies for a better understanding of how to improve our health and control the proliferation of pathogens.

Chapter 7

Annex

7.1 Cloning protocols

7.1.1 Gibson assembly reaction mix

Gibson assembly is the method that we have used in most of our clonings. To prepare the Gibson assembly reaction mix, first we need to prepare the 5x ISO buffer, by following the recipe in Table 7.1

Table 7.1: 5x ISO buffer components.

3 ml	1 M Tris-HCl pH 7.5
150 μl	2 M $MgCl_2$
60 μl	100 mM dGTP
60 μl	100 mM dATP
60 μl	100 mM dTTP
60 μl	100 mM dCTP
300 μl	1 M DTT
1.5 g	PEG-8000
300 μl	100 mM NAD

Add water up to 6 ml.

Then, we can prepare the reaction mix for the Gibson assembly by following the recipe in Table 7.2

Table 7.2: Gibson assembly reaction mix components.

320 μl	5X ISO buffer
0.64 μl	10 U/μl T5 exonuclease
20 μl	2 U/μl Phusion polymerase
160 μl	40 U/μl Taq ligase

Add water up to 1.2 ml (699.36 μl)
Aliquot 15 μl and store at -20 °C.

7.2 Transformation of competent cells

Transformation is the natural process by which competent bacteria can introduce DNA from the environment to increase genetic diversity to cope with stress. In molecular biology, this process has been adapted for introducing plasmids into bacteria, to store them or to express, for example, a protein of our interest. Different methods increase the number of competent cells, and the most common methods for transforming bacteria are the chemical and electrical transformations. Genetically modified bacteria, such as DH5α or DH10b, are designed to transform the vectors and keep them without modifications easily. In the following sections, we are going to see in detail the protocols that we have used for these two kinds of transformation methods.

It is interesting to know that there is the possibility to use commercial competent cells. If so, it is recommended to follow the protocol by the manufacturer.

7.2.1 Chemical transformation in *Escherichia coli*

The chemical transformation method consists of a treatment with a dilution of $CaCl_2$ and a brief incubation at high temperature, known as heat shock.

Protocol:

Day 1
Prepare an overnight culture by placing a sample of bacteria from the glycerol stock in 10ml LB medium with antibiotics, at 37°C with shaking.

Day 2

It is necessary to prepare: Chilled $CaCl_2$ 50 mM, pre-warmed SOC medium, a water bath at 42°C, a bucket with ice and LB plates with the antibiotic for selection.
Prepare one 50 ml tube with a 1:10 dilution of the liquid culture with LB. For example, add 1 ml of ON culture and 9 ml of LB with antibiotics, if they are needed. Let the culture grow for $\sim$3 hours at 37°C, to the exponential growth phase. To prepare competent cells, start by placing the tubes on ice for 20 min. From this moment, it is critical to keep the culture always on ice until the end of the procedure. Prepare as many Eppendorf tubes as samples to transform (at least three tubes)[1] with 1.4 ml of the cold liquid culture. Centrifuge the cells for 1 min at 13000 rpm and discard the supernatant. Add 500 μl ice-cold $CaCl_2$ 50 mM and incubate on ice for 30 min. Repeat the centrifugation and discard the supernatant. Add 100 μl ice-cold $CaCl_2$ and dissolve the pellet by very gentle pipetting. Cells that can be stored at -80°C for future transformations, or they can be used for the transformation protocol. Note: If we use a stored batch of competent bacteria, it is necessary to melt them by placing the tubes into ice for around 5 min.

To transform the desired DNA into the competent bacteria, add between 0.1-0.5 μg of DNA (4-6 μl) in each Eppendorf tube, mix briefly by tapping the tube, and incubate on ice for 30 min. Remember also to prepare the positive and the negative control tubes. For the heat-shock, transfer the tubes into a 42°C water bath for exactly 90 sec and immediately incubate the cells on ice for 2 min. After, remove the tubes from the ice and add 1 ml pre-warmed SOC medium. Incubate the tubes at 37°C with shaking for 1 hour to let the cells express the selective resistance. Finally, centrifuge the cells at 13000 rpm for 2 min, remove the supernatant and resuspend the pellet in the remaining liquid. Plate $\sim$50 μl on an LB agar plate with the antibiotic for selection and incubate at 37°C overnight.

Day 3

Pick single colonies from the plates and grow them in 10 ml LB, conditioned with the antibiotic for selection, at 37°C with shaking. If the plasmid transformed plasmid comes from Gibson assembly or ligation, it is necessary to check the colonies by colony PCR before growing the cells.

---

[1] It is recommended to have one tube as a positive control by transforming a known plasmid, for example, PUC19 vector, and a negative control, where we can add water instead of the plasmid. The positive control informs us about the success of the protocol and the negative control checks for possible contamination during the process.

The positive colonies will be stored and they will be used to extract the plasmid for sequencing.

Day 4
Store cells by preparing a glycerol stock. Add in one tube, 1 ml of the overnight culture and 1 ml of a 40% dilution of glycerol and store them at -80°C. If necessary, extract the plasmid and send for sequencing to validate the cloning.

This protocol has been adapted from prof. Gürol Süel's lab.

7.2.2 Electroporation in *Escherichia coli*

Electroporation is a method that uses an electrical pulse to create temporary pores in the cell membrane through which cells can incorporate external DNA. This technique has higher efficiency than other methods of transformation and can be applied to different kinds of cells, from bacteria to mammal cells. We now provide a protocol to produce competent cells and the process for electroporation.

Protocol:

Day 1
Prepare an overnight culture by placing a sample of bacteria from the glycerol stock (DH5α or DH10b, or other specific strains) in 10 ml LB medium with antibiotics, if required, at 37°C with shaking.

Day 2
It is necessary to prepare: Chilled $ddHl_2O$, electroporation cuvettes (1 mm gap) at -4°C, pre-warmed SOC medium, a bucket with ice and LB plates with the antibiotic for the selection.

Prepare as many Eppendorf tubes as samples to transform (at least three, considering the positive and negative controls), add 1.4 ml LB, with antibiotics if necessary, and inoculate 30 μl of the overnight culture. Let the culture grow for $\sim$3 hours at 37°C with shaking. To prepare the cells for electroporation, incubate the tubes on ice for 30 min. From this moment on, it is critical to keep the cells on ice during the whole procedure. Centrifuge the tubes for 30 sec at 11000 rpm and discard the supernatant. Resuspend the pellet with 1 ml of chilled $ddHl_2O$, by gently pipetting up and down. Repeat the centrifugation, discard the supernatant and resuspend the cells again with 1 ml $ddHl_2O$. Centrifuge one last time, remove the supernatant and resuspend the cells in the remaining liquid ($\sim$50 μl). In this step, cells are already prepared for electroporation. For this transformation method, it is recommended to prepare fresh competent cells each time.

To electroporate the DNA, add 1 μl of the vector to the cell suspension and mix briefly, keeping the tube on ice. Transfer the each liquid culture at the bottom of chilled electroporation cuvettes. Before the electroporation, dry the exterior of the cuvettes to ensure that there is no arching during the process. Electroporate the cells at 1350 mV, 10 μF, 600 Ω, and immediately resuspend them in 1 ml SOC medium without antibiotics. Transfer all the samples to different Eppendorf tubes and incubate at 37°C for 1 hour with shaking. Plate $\sim$100 μl on an LB agar plate with the antibiotic for selection and incubate at 37°C overnight. Because of the efficiency of this protocol, consider preparing an extra plate with a dilution of the sample to avoid overgrowth.

Day 3
Pick single colonies from the plates and grow them in 10 ml LB, conditioned with the antibiotic for selection, at 37°C with shaking. If the plasmid that we have transformed comes from Gibson assembly or ligation, it is necessary to check the colonies by colony PCR before growing them. The ones that are positive will be the colonies that we will store and extract the plasmid for sequencing.

Day 4
Store cells by preparing a glycerol stock. Add in one tube, 1 ml of the overnight culture and 1 ml of a 40% dilution of glycerol and store them at -80°C. If it is necessary, extract the plasmid and send for sequencing to validate the cloning.

This protocol is based on Gene Bridges - Quick and Easy E. coli Gene Deletion Kit. By Red/ET Recombination, version 2.4 (May 2014)

7.2.3 Transformation in *Bacillus subtilis*

For *Bacillus subtilis*, we can use the same protocol for plasmid transformation and chromosomal integration. The difference comes from the plasmid that we use in the cloning. For example, plasmids pDG148 and pHP13 can be maintained inside the bacteria to overexpress a particular protein, and plasmids pER449 and JDE131 are used to integrate constructs into the chromosome (we will see in more detail the integration in *B. subtilis* in Section 7.3).

For the transformation protocol in *Bacillus subtilis*, we prepare the transformation medium by following the next recipe (see Table 7.3):

Table 7.3: Transformation media and preparation for 250 ml.

25 g/l	$K_2HPO_4.3H_2O$	6.25 g
6 g/l	K_2HPO_4	1.5 g
1 g/l	trisodium citrate	0.25 g
0.2 g/l	$MgSO_4.7H_2O$	50 mg
2 g/l	Na_2SO_4 (pH 7.0)	0.5 g
50 μM	$FeCl_3$	125 μl of 100mM $FeCl_3$
2 μM	$MnSO_4$	5 μl of 100mM $MnSO_4$
0.4%	glucose	1 g
0.2%	glutamate	0.5 g

Filter sterilize

Transformation protocol:

Day 1
Streak a LB plate with the strain to transform, and incubate overnight at 37°C.

Day 2
Prepare as many tubes as different strains to transform and inoculate 5 ml of transformation media with several independent colonies. The amount of colonies varies depending on the size of the colonies. Vortex briefly the liquid to homogenize the culture and incubate for ~3 hours at 37°C, to an OD_{600} = ~0.8. If the OD_{600} is higher than 1.5, then, dilute the cells back to OD_{600} = 0.25, and let them grow to the desired concentration. After, prepare as many tubes as we need to transform (minimum three tubes, considering the positive and negative controls for each strain) and place 1 ml of the liquid culture. Add to each tube ~8 μl (0.5-4 *u*g) of plasmid and incubate the culture at 37°C with shaking for 40 min. After, add 1 ml of LB medium and incubate for an additional 45 min. Centrifuge

the culture 1 min at 11000 rpm, discard the liquid, resuspend the pellet in the remaining liquid, and plate ∼100 μl in a plate with the antibiotic for selection.

Day 3
Pick single colonies from the plates and grow them in 10 ml LB, conditioned with the antibiotic for selection, at 37°C with shaking. If the transformation is to generate a chromosomal integration, we should check the colonies by colony PCR before growing them. The ones that are positive will be the colonies that we will store.

Day 4
Store cells by preparing a glycerol stock. Add in one tube, 1 ml of the overnight culture and 1 ml of a 40% dilution of glycerol and store them at -80°C.

This protocol has been adapted from Prof. Gürol Süel's lab.

7.3 Chromosomal integration and knockout

Chromosomal integration is a strategy to overcome the overexpression of genes included in plasmids and generate a more stable expression of the integrated construct, without the possibility of cell dilution. Below, we describe the chromosomal integration protocols for *Escherichia coli* and *Bacillus subtilis*. Notice that this protocol can be used for the integration of constructs or the deletion of genes located in the chromosome.

7.3.1 Chromosomal integration in *Escherichia coli*

For the chromosomal integration in *E. coli*, we use the Red/ET recombination method developed by Datsenko and Wanner (2000). This method is based on the phage-derived proteins Redα/Redβ from the λ phage, and we can use it for ectopic integration of a construct, as well as for deletion of chromosomal genes.

The plasmid pKD46 encodes all the components to mediate the Red/ET recombination, knwon as the λ-Red genes (α, β, γ). These genes are placed under an arabinose-inducible promoter ($\mathrm{P_{BAD}}$), so, during the protocol we need to induce this promoter to express the recombination genes. This plasmid also contains a temperature-sensitive replication origin (this kind of vector is known as a *suicidal vector*). Hence, we need to grow the cells at 30°C if we do not want to lose the plasmid.

The Red/ET recombination starts by the Recα protein; an exonuclease that generates a double-stranded DNA break in the linearized cassette and it hydrolizes the 5'-extreme, generating a single 3'-stranded arm. Later, the Recβ proteins, single-strand binding proteins, cover the single-strand chain and help the cassette to find the complementary region of the genome, where the recombination occurs. This sequence will be used as a template for the next round of genome replication. In parallel, the Redγ protein inhibits the recBCD nuclease activity of *E.coli*, that eliminates linearized DNA.

The protocol starts with the assembly of all the pieces of the cassette that we want to introduce in the genome. For integrations, the cassette consists in the construct that we want to insert, and expresses, for example, an inducible promoter that controls a fluorescent protein, an antibiotic resistance gene as a marker, and two FRT-sites which flank both extremes of the cassette. In the case of deletions, we only need the cassette with the resistance gene and the FRT-sites (Fig. 7.1). To obtain the resistance and the FRT-sites, we can use as a template the plasmid pKD3 (FRT-Amp-FRT), pKD4 (FRT-Kan-FRT) or pKD13 (FRT-Kan-FRT). Apart from these pieces, the cassette should also have two arms with homology to the adjacent regions where we want to insert it. The optimal length for these homology arms is 50 nucleotides, and they can be introduced by PCR. It is recommended to clone this construct into a vector for future integrations.

Protocol for the integration of the cassette into *E. coli*'s chromosome:

Day 1

Overnight culture of the strain that we want to manipulate. Start an overnight culture with the desired strain in LB medium, conditioned with antibiotics if it is needed, at 37°C with shaking.

Day 2

Transformation of the plasmid pKD46 into the strain that we want to mod-

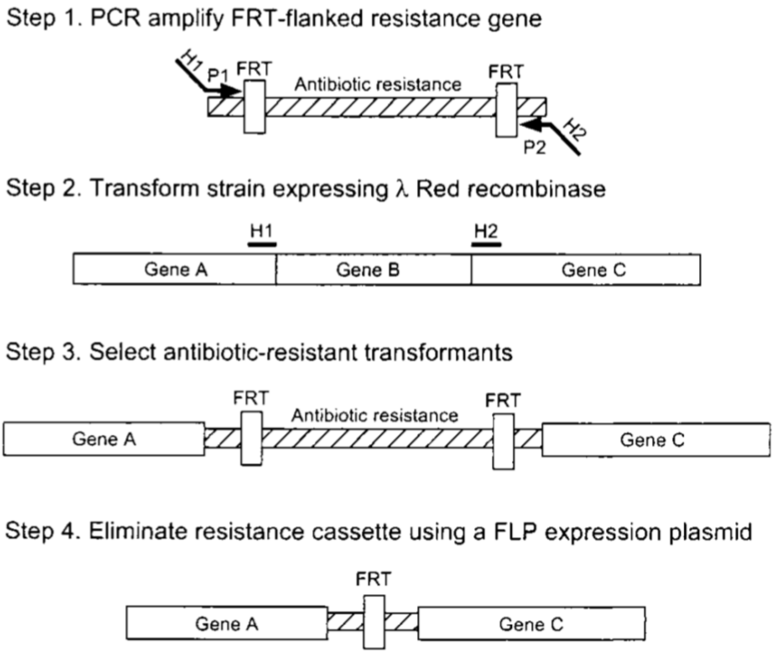

Figure 7.1: Diagram of the different phases for chromosome integration in *E. coli*. This example illustrates the disruption strategy by the substitution of Gene B for an antibiotic resistance gene. The last step corresponds to the elimination of the antibiotic gene, leaving a scar in the genome, a FRT region. H1 and H2 mark the homology regions in the primers, as well as in the genome. P1 and P2 refer to priming sites. Figure adapted from Datsenko and Wanner (2000)

ify. Transform pKD46 plasmid into the desired strain by chemical transformation or electroporation. To express the resistance gene after the heat shock or the electroporation, let the cells grow at 30°C for 70 min, and streak them in LB agar plates with 100 μ/ml ampicillin (pKD46 has the ampicillin resistance gene). Let the plates grow overnight at 30°C.

Day 3

Pick independent colonies and place them in LB medium with 100 μ/ml ampicillin. Let them grow overnight at 30°C with shaking.

Day 4

1. Store cells at -80°C.

2. *Induce the recombination proteins.* Use the rest of the culture to continue the chromosomal integration/deletion. Prepare as many tubes as samples to transform and let one tube as a negative control. Inoculate 30 μl of the overnight culture to each tube and add 1.4 ml of LB medium. Incubate the tubes at 30°C for $\sim$2 hours with shaking, to reach an $\mathrm{OD}_{600} \sim 0.3$. At that moment, add L-arabinose to a final concentration of 0.3-0.4% (50 μl of 10%) in al tubes, except for the negative control. Incubate at 37°C with shaking, for 45 min-1 hour. It is important to incubate cells at 37°C to express the recombination proteins (in this step it is not necessary to replicate the plasmid, just to express the proteins).

3. *Transform the linearized cassette.* Prepare cells for electroporation and add 200-400 ng of the linear cassette with homology arms in all tubes. Electroporate and incubate at 37°C with shaking, for 3 hours. In this period of time, the recombination occurs. Streak the cells in LB agar plates with the antibiotic of selection for the integration. Remember that pKD46 is a suicide vector, so it will be eliminated at 37°C. In this step, the selection is for the cells that have incorporated the cassette; hence, the plates should not have ampicillin, just the antibiotic that the cassette has. Incubate the plates at 37°C overnight.

Day 5

Streak the colonies in new plates, and let them grow overnight at 37°C. This step will eliminate possible contaminations and will help to eliminate the pKD46 vector.

Day 6

1. *Colony PCR.* Pick independent colonies from the streaks and perform a colony PCR to identify the colonies that have incorporated the cassette in the desired region.

2. Place the positive colonies in LB medium with the antibiotic of selection and let them grow overnight at 37°C with shaking.

3. To further confirm the elimination of the pKD46 vector, streak a

sample for each positive colony in a LB plate with ampicillin and let the plate at 37°C overnight.

Day 7

1. Store cells at -80°C.
2. Check the plates to see if pKD46 plasmid has been eliminated. If the plasmid of all colonies is still inside the cells, it will be necessary to regrow the cells at 37°C. If the plasmid remains, cells can be grown at 43°C.

Optional step
It is possible to eliminate the antibiotic resistance marker from the genome by transforming pCP20 vector. This plasmid has the FLP gene from yeast, which expresses a flipase controlled by thermal induction at 43°C (Δ*stm3071::cm*). It also has a temperature-sensitive replication origin, so it is important to growing cells at 30°C. Once the pCP20 has been transformed into the desired strain, incubate the cells at 30°C for 70 min with shaking, to express the antibiotic resistance. Streak the cells in a LB plate with ampicillin (100 μg/ml) or chloramphenicol (10 μg/ml), and let the plate growing overnight at 30°C. After selecting the colonies, grow them at 43°C to activate the expression of the flipase and eliminate the plasmid. This protein recombines the two FRT sites, producing the excision of the cassette. Finally, test the colonies for the elimination of the cassette. This procedure leaves a scar in the genome that consists in one FRT site.

This protocol has been adapted from Gene Bridges - Quick and Easy E. coli Gene Deletion Kit. By Red/ET Recombination, version 2.4 (May 2014)

7.3.2 Chromosomal integration in *Bacillus subtilis*

For chromosomal integration in *Bacillus subtilis*, we need to use shuttle vectors. These plasmids have conditional replication; they can be replicated in *E. coli* but not in *B. subtilis*. Hence, after the integration in the desired organisms, the plasmids will be lost by dilution. Some examples of chromosomal integration vectors are pER449 and JDE131.

The mechanism of integration of these plasmids is by double homologous recombination. This method can be used to eliminate a gene from the chromosome or to integrate a construct, for example, a promoter-fusion of a natural promoter and a fluorescent reporter. The cassette used for deletion of genes contains an antibiotic resistance gene and flanking homology regions of the sequences contiguous to the gene that we want to eliminate, with an optimal length of ∼700 bp for each arm. For the chromosomal integration of a construct, we can add the desired sequence inside the cassette, and this will be placed on the selected chromosomal site. The common sites for expression of an integrated construct are *sacA*, *amyE*, *pyrD*, *lacA* and *gltA*. For the details on plasmid transformation, see Section ref.transfbacillus.

7.4 Data acquisition

7.4.1 Time-lapse fluorescence microscopy

In this Thesis, we have used time-lapse fluorescence microscopy to track single cells for the study different dynamical processes, like the cell cycle and the membrane potential dynamics. In this Section, we describe a detailed protocol for the imaging of microcolonies in agarose pads and microfluidic devices.

Imaging in agarose pads

Agarose pads are used to fixed bacteria in a surface for the imaging process. The bacteria are trapped between a thin layer of agarose and a coverslip, but the matrix of agarose is gentle with the cells, it permits the exchange of nutrients and gases, and it gives enough space for the bacterial growth in the horizontal axis. Moreover, we can add nutrients in these pads, as well as other chemicals, such as inductors or antibiotics. Thus, this technique allows us to perform quantitative analysis of single cells over time.

Despite the advantages of this technique, we need to consider the limitations that it presents when we decide to work with it. The pads contain a limited amount of nutrients that are consumed over time due to the growth of bacteria. Thus, the composition of the agarose pads is not constant. Also, the matrix of agarose is flexible, and after several hours, cells accumulate, forming clumps. These structures are very compact, and it is not possible to differentiate single cells. Then, the duration of the analysis with this technique is limited to a reduced number of generations in the lineage.

In Chapters 3 and 5, we selected this technique due to the simplicity of the preparation of the pads. For Chapter 3, we did not need a long period of analysis, neither to change the conditions during the experiments. For Chapter 5, we used agarose pads to take snap-shots of the culture that was growing in the plate reader experiment.

Protocol:

Day 1

Prepare an ON culture, as it follows: 10 ml LB + antibiotics, at 37°C on the incubator, with 225 rpm of shaking.

Day 2

1. Prepare a new tube with 5 ml LB and a final $OD_{600} = 0.02$ with antibiotics and inductors:
   5 ml LB + antibiotics + 140 μl Arabinose (stock 25% - final concentration 0.07%) + 50 μl IPTG (stock 200 mM - final concentration 2 mM) + x μl from ON (Final $OD_{600} = 0.02$)
   Let the tub in the incubator 2 hours at 37°C, with 225 rpm, until OD_{600} $\sim$0.1-0.2
2. Prepare fresh medium for the pads. See the media recipe in Table 7.5. Example for 75 ml:
   15 ml A Salts (5x) + 60 ml autoclaved dH_2O + 75 μl $MgSO_4.7H_2O$ (1 M) + 187.5 $\sim$188 μl Glycerol (80%) + 750 μl CasaAa (10%)
3. Prepare at least 2 agarose pads; one is the ‘imaging pad’ (size: cover-slip 30x60 mm), and the other one is the ‘growing pad’ (size: cover-slip 20x20 mm). The number of growing pads is the same as strains to study. To prepare the pads, microwave 15 ml MMA (it should be fresh) with 0.225 g low-melting agarose (1.5% final concentration). Once the liquid is cold, but not solid, add the inductors (arabinose + IPTG). Pour 5 ml of the liquid in a glass cover-slip for the ‘imaging pad’ and 2 ml for the ‘growing pad,’ cover with another cover-slip of the same size, and let them dry. Once the pads are solid, move them into the stove at 37°C and incubate them for at least 1 hour.
4. Measure the OD_{600} of the culture and dilute it 1:5 in a media with inductors. For example: 200 μl bacteria + 800 μl MMA + inductors.
5. Separate ‘growing pads’ in different petri dishes and add 50 μl of the diluted culture (each strain in a different ‘growing pad’). Let the pads in the stove at 37°C for 2 hours.

6. Prepare as many 50 ml falcon tubes as ‘growing pads’ with 7.5-10 ml pre-warmed MMA (without inductors), and add the ‘growing pad’ into it. Vortex during 1-2 min.
7. Cut the imaging pad in small squares (size 1x1 cm) and add 2.25 μl from the falcon. Let one pad for fluorescent beads.
8. Prepare one square for the fluorescence calibration of the microscope by adding 0.1 μl beads (0.5 μm) on the pad and 2.25 μl ddH_2O
9. Let the pads dry in the stove at 37°C for 15 min.
10. Put the pad in the dryer for 15 min.
11. Place the different pads, flipped, in a Willco dish and annotate the positions in the notebook.
12. Set the Willco in the microscope and let it equilibrate for 1 hour.

Parameters for the microscope:
- Constant temperature in a control chamber at 37°C
- Steps in range: Two passes (range) - 70 μm, coarse step - 1.2 μm, fine step - 0.4 μm, Criterion - bright-field
- Bright-field bulb voltage = 5.5 V
- Camera set exposer: phase 40 ms, YFP needs to be calibrated at 3000 a.u.
- The fluorescence lamp was turned on 1 hour before the experiments

Table 7.4: Salts A 5x components.

0.5 g	Ammonium sulfate - $_2SO_4$
2.25 g	Potassium dihydrogen phosphate - KH_2PO_4
5.25 g	Potassium phosphate dibasic - K_2HPO_4
0.25 g	Sodium citrate dihydrate - $C_6H_6Na_2O_7.2H_2O$
100 ml	autoclaved water

Sterilize by filtration and store at 20°C.

Imaging in microfluidic devices

Microfluidic devices contain microchambers, which are injected with liquids and gasses with external pumps. These chips are constructed using different materials, but the most common is the polymer PDMS (Poly-DimethylSiloxane). Cells are trapped between the PDMS layer and the glass, forming a monolayer of cells which can be segmented and tracked.

Table 7.5: Minimal medium A components.

8 ml	A Salts 5x
32 ml	ddH_2O
40 μl	$MgSO_4.7H_2O$ (1 M)
100 μl	Glycerol (80%)
400 μl	CasaAa (10%)

This media cannot be stored for future experiments.

These chips are customizable, but due to the small size of the bacteria (e.g., *E. coli* has 1-3 μm of width) the fabrication of such devices requires expertise and can be expensive to produce.

There are two main advantages of this technique compared to the agarose pads, First, thanks to the flow of media from external pumps, it is possible to maintain a constant environment by flowing new medium into the microfluidic chambers. By using the same principle, it is also possible to change the medium and create a completely different environment if needed. Secondly, once the chamber is full of bacteria, the flow of medium washes the excess of cells, allowing us to film for more extended periods of time.

In Chapter 4, we needed to analyze bacteria for several hours and change the media for the addition of antibiotics, as well as the membrane potential dye. For this reason, for that specific study, we used microfluidic devices.

Protocol:

Day 1

Streak cells onto LB agar plate with the antibiotic of selection and incubate overnight at 37°C
Note: Be sure to have all the stocks (Table 7.6) prepared for the next day.

Day 2

1. Pick single colonies from the plate and inoculate into 3 ml of LB medium in a 50 ml falcon tube, and grow the cells at 37°C for 2 hours 45 min. The final OD_{600} should be lower than 1.2.
2. While cells are growing, prepare 30 ml of MSgg media following the recipe in Table 7.8. 5 ml will be separated for 'pure medium' and

10 ml for ‘centrifuge medium.’ Save the remaining 15 ml of MSgg medium.

3. Centrifuge at 4000 rpm for 4 min the ‘centrifuge medium.’
4. Prepare the Cellasic plate. First, check the plate for possible obturation of the channels by running the liquid that the chip contains. After checking, remove all the media and fill wells with ‘centrifuge medium’ (1 ml/row).
5. Prime the Cellasic plate opening wells from 1-6, at 2 psi for 20 min at 37°C.
6. After 2 hours 45 min of incubation, measure the OD. Take 1 ml of the cell culture and centrifuge at 4800 rpm for 1 min.
7. Remove the supernatant and resuspend the pellet vigorously in 1 ml of ‘centrifuge medium.’
8. Immediately, put the cells into well 8 and load cells in the microfluidic device by opening wells 1-6 and 8, 4 psi, 10 sec.
9. After loading, remove the cells from well 8 and carefully wash it with 1 ml of ‘centrifuge medium’.
10. Remove all the media from wells 1-6 and refill with ‘pure medium’. In this step, we have finished preparing the Cellasic plate.
11. Set the protocol of the plate to let the cell grow overnight at 37°C with a constant media flow.

Day 3

1. Prepare the media for the experiment with the remaining 15 ml. For example, add a final concentration of 10 μM ThT.
2. Once the cells have grown enough, take out the Cellasic plate, remove the media from wells 1-6 and set the plate with the required media for the experiment.
3. Set up the protocol for the plate. For example, for the experiments with *Bacillus subtilis* set the temperature at 30°C and add constant media conditioned with ThT and spectinomycin (2 μg/ml).

This protocol has been adapted from prof. Gürol Süel’s lab.

Table 7.6: Recipes for the different stock solutions.

Stock solutions:	
1.03 g for 10 ml	0.7 M $CaCl_2.2H_2O$
2.03 g for 5 ml	2 M $MgCl_2.6H_2O$
0.27 g for 10 ml	0.1 M $FeCl_3.6H_2O$
0.1 g for 10 ml	0.05 M $MnCl_2.4H_2O$
0.136 g for 10 ml	0.1 M $ZnCl_2$
0.169 for 10 ml	0.1 M Thiamine HCl
2.72 g or 1.275 g for 50 ml	0.5 M K_2HPO_4 or KH_2PO_4

Table 7.7: Recipe for the MSgg salts.

MSgg salts / ion mix:	
1000 μl	50% Glycerol
1000 μl	50% Glutamate monosodium salt
100 μl	0.7 M $CaCl_2.2H_2O$
100 μl	2 M $MgCl_2.6H_2O$
100 μl	0.1 M $FeCl_3.6H_2O$
100 μl	0.05 M $MnCl_2.4H_2O$
1 μl	0.1 M $ZnCl_2$
2 μl	0.1 M Thiamine HCl
Total volume	2403 μl

Table 7.8: Preparation of the MSgg medium.

MSgg solution for 100 ml:	
1000 μl	0.5 M Potassium phosphate buffer (pH 7.0)
10000 μl	1 M MOPS (pH 7.0) w/ NaOH
2403 μl	MSgg salts
Up to 100 ml (86597 ml) of ddH_2O	

7.5 Plate-based assay

We now describe the protocol used in this Thesis to prepare the 96-well microplate (Nunc, Denmark) for measurements in the plate reader (Tecan Infinite M200 Pro).

Day 1

Prepare an ON culture by adding 10 ml LB + antibiotics, at 37°C on the incubator, with 225 rpm of shaking.

Day 2

1. Dilute the ON culture at final $OD_{600} = 0.1$ + antibiotics in 5 ml LB, and let cells grow at 37°C for 2 hours, with 225 rpm of shaking.
2. Switch to 30°C and let them grow for 2 hours.
3. Dilute the culture at final $OD_{600} = 0.1$ in 5 ml LB, and add 25 μl IPTG (stock 200 mM - final concentration 1 mM). After, let them grow 2 hours more.
4. Prepare the 96-well plate with the desired conditions (see Fig. 7.2).

For the experiments in Chapter 5, a serial dilution of the antibiotic was prepared, starting at 100 μg/ml of ampicillin.

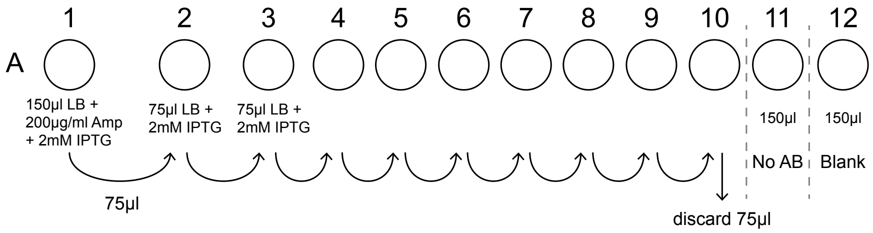

Figure 7.2: Scheme of an antibiotic serial dilution for the microplate preparation. A 96-well plate was prepared for each experiment with serial dilutions of ampicillin. Just one row out of eight (A) is represented in the scheme. The final total volume for each well was 150 μl. The first well contained 150 μl with 200 μg/ml of ampicillin (final concentration) and 2 mM IPTG, the rest contained 75 μl of LB with 2 mM IPTG and without antibiotics, except well 12 that contained 150 μl of LB with 2 mM IPTG and without antibiotics. We began the serial dilution taking 75 μl of LB from well one and passed it to the next well. We mixed up and down to make the liquid homogeneous and changed the tip. In this way, we were diluting the antibiotic to a half concentration, without varying the amount of IPTG. We repeated this operation until well 10 and discarded 75 μl from this well. For the final step, we needed to add 75 μl of plain LB with the double of the desired concentration of bacteria, from well 1 to 11. For these experiments we used a final $OD_{600} = 0.01$, then the LB was prepared with a final $OD_{600} = 0.02$. When we added LB with bacteria, but no antibiotics or IPTG, we were diluting everything to half reaching the desired final concentrations.

Contributions

Original research articles

Mutual regulation causes co-entrainment between a synthetic oscillator and the bacterial cell cycle
Dies, M., Galera-Laporta, L., Garcia-Ojalvo, J.
Integrative Biology (2016), 8, 533. http://dx.doi.org/10.1039/C5IB00262A.

Membrane potential dynamics reveal ion flux modulation as a determinant of bacterial survival
Lee, D. D.*, Galera-Laporta, L.*, Bialecka-Fornal, M.*, Moon, E. C., Shen Z., Briggs S. P., Garcia-Ojalvo, J. and Süel, G. M.
*Equal contribution.
Cell, under review (2018)

Antibiotic sensitivity swap in bacterial mixed-species communities
Galera-Laporta, L., Garcia-Ojalvo, J.
(to be submitted)

References

Akanuma, G., Kobayashi, A., Suzuki, S., Kawamura, F., Shiwa, Y., Watanabe, S., Yoshikawa, H., Hanai, R., and Ishizuka, M. (2014). Defect in the formation of 70S ribosomes caused by lack of ribosomal protein l34 can be suppressed by magnesium. *Journal of Bacteriology*, 196(22):3820–3830.

Akanuma, G., Nanamiya, H., Natori, Y., Yano, K., Suzuki, S., Omata, S., Ishizuka, M., Sekine, Y., and Kawamura, F. (2012). Inactivation of ribosomal protein genes in *Bacillus subtilis* reveals importance of each ribosomal protein for cell proliferation and cell differentiation. *Journal of Bacteriology*, 194(22):6282–6291.

Allan, E. J., Hoischen, C., and Gumpert, J. (2009). Bacterial L-Forms. *Advances in Applied Microbiology*, 68(9):1–39.

Amato, S., Orman, M., and Brynildsen, M. (2013). Metabolic Control of Persister Formation in Escherichia coli. *Molecular Cell*, 50(4):475–487.

Baker, T. A. and Sauer, R. T. (2012). ClpXP, an ATP-powered unfolding and protein-degradation machine. *Biochimica et Biophysica Acta - Molecular Cell Research*, 1823(1):15–28.

Balaban, N. Q., Merrin, J., Chait, R., Kowalik, L., and Leibler, S. (2004). Bacterial persistence as a phenotypic switch. *Science (New York, N.Y.)*, 305(5690):1622–5.

Balázsi, G., van Oudenaarden, A., and Collins, J. J. (2011). Cellular decision making and biological noise: From microbes to mammals. *Cell*, 144(6):910–925.

Ban, N., Nissen, P., Hansen, J., Moore, P. B., and Steitz, T. A. (2000). The complete atomic structure of the large ribosomal subunit at 2.4 Åresolution. *Science (New York, N.Y.)*, 289(5481):905–20.

Banks, E. D., Taylor, N. M., Gulley, J., Lubbers, B. R., Giarrizzo, J. G., Bullen, H. A., Hoehler, T. M., and Barton, H. A. (2010). Bacterial calcium carbonate precipitation in cave environments: A function of calcium homeostasis. *Geomicrobiology Journal*, 27(5):444–454.

Bassler, B. L. (2002). Small Talk: Cell-to-Cell Communication in Bacteria. *Cell*, 109(4):421–424.

Bates, D. and Kleckner, N. (2005). Chromosome and replisome dynamics in E. coli: Loss of sister cohesion triggers global chromosome movement and mediates chromosome segregation. *Cell*, 121(6):899–911.

Beardmore, R. E., Cook, E., Nilsson, S., Smith, A. R., Tillmann, A., Esquivel, B. D., Haynes, K., Gow, N. A. R., Brown, A. J. P., White, T. C., and Gudelj, I. (2018). Drug-mediated metabolic tipping between antibiotic resistant states in a mixed-species community. *Nature Ecology & Evolution*, 2(8):1312–1320.

Belenky, P., Ye, J. D., Porter, C. B. M., Cohen, N. R., Lobritz, M. A., Ferrante, T., Jain, S., Korry, B. J., Schwarz, E. G., Walker, G. C., and Collins, J. J. (2015). Bactericidal antibiotics induce toxic metabolic perturbations that lead to cellular damage. *Cell Reports*, 13(5):968–980.

Bigger, J. (2009). Treatment of *Staphylococcal* infections with penicillin by intermittent sterilisation. *The Lancet*, 244(6320):497–500.

Blango, M. G. and Mulvey, M. A. (2009). Bacterial landlines: contact-dependent signaling in bacterial populations. *Current Opinion in Microbiology*, 12(2):177–181.

Blow, J. J. and Gillespie, P. J. (2008). Replication licensing and cancer - A fatal entanglement? *Nature Reviews Cancer*, 8(10):799–806.

Bosdriesz, E., Molenaar, D., Teusink, B., and Bruggeman, F. J. (2015). How fast-growing bacteria robustly tune their ribosome concentration to approximate growth-rate maximization. *FEBS Journal*, 282(10):2029–2044.

Boylan, S. A., Redfield, A. R., Brody, M. S., and Price, C. W. (1993). Stress-induced activation of the sigma B transcription factor of Bacillus subtilis. *Journal of Bacteriology*, 175(24):7931–7937.

Brendler, e. a. (1999). Binding of SeqA protein to DNA requires interaction between two or more complexes bound to separate hemimethylated GATC sequences. *The EMBO Journal*, 18(8):2304–2310.

Brendler, T., Abeles, A., and Austin1, S. (1995). A protein that binds to the P1 origin core and the oriC 13mer region in a methylation-specific fashion is the product of the host seqA gene. *The EMBO Journal*, 14(16):4083–4089.

Brown, L., Wolf, J. M., Prados-Rosales, R., and Casadevall, A. (2015). Through the wall: extracellular vesicles in Gram-positive bacteria, mycobacteria and fungi. *Nature Reviews Microbiology*, 13(10):620–630.

Bruni, G. N., Weekley, R. A., Dodd, B. J. T., and Kralj, J. M. (2017). Voltage-gated calcium flux mediates *Escherichia coli* mechanosensation. *Proceedings of the National Academy of Sciences of the United States of America*, 114(35):9445–9450.

Buchanan, R. E. (1928). Growth phases; composition and biophysical chemistry of bacteria and their environment; and energetics. *Physiology and Biochemistry of Bacteria.*, 26(4):327.

Buchler, N. E. and Louis, M. (2008). Molecular titration and ultrasensitivity in regulatory networks. *Journal of Molecular Biology*, 384(5):1106–1119.

Burg, K., Collins, A. R. S., and Johnson, R. T. (1977). Effects of ultraviolet light on synchronized Chinese hamster ovary cells; potentiation by hydroxyurea. *J.Cell.Sci.*, 28:29–48.

Burton, R. E., Siddiqui, S. M., Kim, Y. I., Baker, T. A., and Sauer, R. T. (2001). Effects of protein stability and structure on substrate processing by the ClpXP unfolding and degradation machine. *EMBO Journal*, 20(12):3092–3100.

Camara, J. E., Breier, A. M., Brendler, T., Austin, S., Cozzarelli, N. R., and Crooke, E. (2005). Hda inactivation of DnaA is the predominant mechanism preventing hyperinitiation of Escherichia coli DNA replication. *EMBO reports*, 6(8):736–41.

Carter, A. P., Clemons, W. M., Brodersen, D. E., Morgan-Warren, R. J., Wimberly, B. T., and Ramakrishnan, V. (2000). Functional insights from the structure of the 30S ribosomal subunit and its interactions with antibiotics. *Nature*, 407(6802):340–8.

Celiker, H. and Gore, J. (2013). Cellular cooperation: insights from microbes. *Trends in Cell Biology*, 23(1):9–15.

Chen, A. H., Lubkowicz, D., Yeong, V., Chang, R. L., and Silver, P. A. (2015). Transplantability of a circadian clock to a noncircadian organism. *Science Advances*, 1(5):1–6.

Chen, S. S., Sperling, E., Silverman, J. M., Davis, J. H., and Williamson, J. R. (2012). Measuring the dynamics of *E. coli* ribosome biogenesis using pulse-labeling and quantitative mass spectrometry. *Molecular bioSystems*, 8(12):3325–34.

Chiba, S., Lamsa, A., and Pogliano, K. (2009). A ribosome-nascent chain sensor of membrane protein biogenesis in Bacillus subtilis. *EMBO Journal*, 28(22):3461–3475.

Cohen, S. E. and Golden, S. S. (2015). Circadian rhythms in *Cyanobacteria. Microbiology and Molecular Biology Reviews*, 79(4):373–385.

Collier, J. and Shapiro, L. (2009). Feedback control of DnaA-mediated replication initiation by replisome-associated HdaA protein in Caulobacter. *Journal of Bacteriology*, 191(18):5706–5716.

Cooper, S. and Helmstetter, C. E. (1968). Chromosome replication and the division of *Escherichia coli* b/r. *J Mol Biol.*, 3(31):519–40.

Cordero, O. X., Wildschutte, H., Kirkup, B., Proehl, S., Ngo, L., Hussain, F., Le Roux, F., Mincer, T., and Polz, M. F. (2012). Ecological Populations of Bacteria Act as Socially Cohesive Units of Antibiotic Production and Resistance. *Science*, 337(6099):1228.

Corrigan, R. M., Bellows, L. E., Wood, A., and Gründling, A. (2016). ppGpp negatively impacts ribosome assembly affecting growth and antimicrobial tolerance in Gram-positive bacteria. *Proceedings of the National Academy of Sciences*, 113(12):E1710–E1719.

Dai, X., Zhu, M., Warren, M., Balakrishnan, R., Patsalo, V., Okano, H., Williamson, J. R., Fredrick, K., Wang, Y.-p., and Hwa, T. (2016). Reduction of translating ribosomes enables *Escherichia coli* to maintain elongation rates during slow growth. *Nature Microbiology*, 16231(December).

Dalebroux, Z. D. and Swanson, M. S. (2012). ppGpp : magic beyond RNA polymerase. *Nature Publishing Group*, 10(3):203–212.

Datsenko, K. A. and Wanner, B. L. (2000). One-step inactivation of chromosomal genes in Escherichia coli K-12 using PCR products. *Proceedings of the National Academy of Sciences of the United States of America*, 97(12):6640–5.

Davis, B. D. (1987). Mechanism of Bactericidal Action of Aminoglycosides. *Microbiological reviews.*, 51(3):341–350.

Dekel, E. and Alon, U. (2005). Optimality and evolutionary tuning of the expression level of a protein. *Nature*, 436(7050):588–592.

Dekens, M. P., Santoriello, C., Vallone, D., Grassi, G., Whitmore, D., and Foulkes, N. S. (2003). Light Regulates the Cell Cycle in Zebrafish. *Current Biology*, 13(23):2051–2057.

Donachie, W. D. (1968). Relationship between Cell Size and Time of Initiation of DNA Replication. *Nature*, 219(5158):1077–1079.

Donachie, W. D. and Blakely, G. W. (2003). Coupling the initiation of chromosome replication to cell size in Escherichia coli. *Current Opinion in Microbiology*, 6(2):146–150.

Dörr, T., Lewis, K., and Vulić, M. (2009). SOS response induces persistence to fluoroquinolones in Escherichia coli. *PLoS Genetics*, 5(12).

Dost, B., Bandeira, N., Li, X., Shen, Z., Briggs, S. P., and Bafna, V. (2012). Accurate mass spectrometry based protein quantification via shared peptides. *Journal of computational biology : a journal of computational molecular cell biology*, 19(4):337–48.

Drawz, S. M. and Bonomo, R. A. (2010). Three decades of β-lactamase inhibitors. *Clinical Microbiology Reviews*, 23(1):160–201.

Duderstadt, K. E., Chuang, K., and Berger, J. M. (2011). DNA stretching by bacterial initiators promotes replication origin opening. *Nature*, 478(7368):209–213.

Dunlap, J. C. and Loros, J. J. (2017). Making Time: Conservation of Biological Clocks from Fungi to Animals. *American Society of Microbiology*, 4(11):515–534.

Dwyer, D. J., Belenky, P. A., Yang, J. H., MacDonald, I. C., Martell, J. D., Takahashi, N., Chan, C. T. Y., Lobritz, M. A., Braff, D., Schwarz, E. G., Ye, J. D., Pati, M., Vercruysse, M., Ralifo, P. S., Allison, K. R., Khalil, A. S., Ting, A. Y., Walker, G. C., and Collins, J. J. (2014). Antibiotics induce redox-related physiological alterations as part of their lethality. *Proceedings of the National Academy of Sciences*, 111(20):E2100.

Edmunds, L. N. (1966). Studies on synchronously dividing cultures ofEuglena gracilis Klebs (strain Z). III. Circadian Components Of Cell Division. *Journal of Cellular Physiology*, 67(1):35–43.

Egan, A. J. F., Cleverley, R. M., Peters, K., and Lewis, R. J. (2017). Regulation of bacterial cell wall growth. *The FEBS Journal*, 284:851–867.

Eldar, A. and Elowitz, M. B. (2010). Functional roles for noise in genetic circuits. *Nature*, 467(7312):167–73.

Elledge, S. J. (1996). Cell cycle checkpoints : Preventing an identity crisis. *Science*, 274(December).

Elowitz, M. B., Levine, A. J., Siggia, E. D., and Swain, P. S. (2002). Stochastic gene expression in a single cell. *Science*, 297(5584):1183–1186.

Feillet, C., Krusche, P., Tamanini, F., Janssens, R. C., Downey, M. J., Martin, P., Teboul, M., Saito, S., Lévi, F. A., Bretschneider, T., van der Horst, G. T. J., Delaunay, F., and Rand, D. A. (2014). Phase locking and multiple oscillating attractors for the coupled mammalian clock and cell cycle. *Proceedings of the National Academy of Sciences*, 111(27):9828–9833.

Ferrell, J. E. (2016). Perfect and Near-Perfect Adaptation in Cell Signaling. *Cell Systems*, 2(2):62–67.

Ferrell, J. M. and Chiang, J. Y. (2015). Circadian rhythms in liver metabolism and disease. *Acta Pharmaceutica Sinica B*, 5(2):113–122.

Fisher, R. P. (2012). The CDK Network: Linking Cycles of Cell Division and Gene Expression. *Genes & Cancer*, 3(11-12):731–738.

Foti, J. J., Devadoss, B., Winkler, J. A., Collins, J. J., and Walker, G. C. (2012). Oxidation of the guanine nucleotide pool underlies cell death by bactericidal antibiotics. *Science*, 336(6079):315.

Francis, D. and Barlow, P. (1988). Temperature and the cell cycle. *Symp Soc Exp Biol.*, (42):181–201.

Fridman, O., Goldberg, A., Ronin, I., Shoresh, N., and Balaban, N. Q. (2014). Optimization of lag time underlies antibiotic tolerance in evolved bacterial populations. *Nature*, 513:418.

Frost, I., Smith, W. P. J., Mitri, S., Millan, A. S., Davit, Y., Osborne, J. M., Pitt-Francis, J. M., MacLean, R. C., and Foster, K. R. (2018). Cooperation, competition and antibiotic resistance in bacterial colonies. *The ISME Journal*, 12(6):1582–1593.

Fuller, R. S., Funnell, B. E., and Kornberg, A. (1984). The dnaA protein complex with the E. coli chromosomal replication origin (oriC) and other DNA sites. *Cell*, 38(3):889–900.

Galdzicki, M., Rodriguez, C., Chandran, D., Sauro, H. M., and Gennari, J. H. (2011). Standard biological parts knowledgebase. *PloS one*, 6(2):e17005.

Gangola, P. and Rosen, B. P. (1987). Maintenance of intracellular calcium in *Escherichia coli*. *Journal of Biological Chemistry*, 262(26):12570–12574.

Gefen, O., Fridman, O., Ronin, I., and Balaban, N. Q. (2014). Direct observation of single stationary-phase bacteria reveals a surprisingly long period of constant protein production activity. *Proceedings of the National Academy of Sciences*, 111(1):556–561.

Gefen, O., Gabay, C., Mumcuoglu, M., Engel, G., and Balaban, N. Q. (2008). Single-cell protein induction dynamics reveals a period of vulnerability to antibiotics in persister bacteria. *Proceedings of the National Academy of Sciences of the United States of America*, 105(16):6145–9.

Geiler-Samerotte, K. A., Bauer, C. R., Li, S., Ziv, N., Gresham, D., and Siegal, M. L. (2013). The details in the distributions: why and how to study phenotypic variability. *Current opinion in biotechnology*, 24(4):752–9.

Gerardin, Y., Springer, M., and Kishony, R. (2016). A competitive trade-off limits the selective advantage of increased antibiotic production. *Nature Microbiology*, 1:16175.

Ghoul, M. and Mitri, S. (2016). The ecology and evolution of microbial competition. *Trends in Microbiology*, 24(10):833–845.

Gibson, D. G., Young, L., Chuang, R. Y., Venter, J. C., Hutchison, C. A., and Smith, H. O. (2009). Enzymatic assembly of DNA molecules up to several hundred kilobases. *Nature Methods*, 6(5):343–345.

Gottesfeld, J. M. and Forbes, D. J. (1997). Mitotic repression of the transcriptional machinery. *Trends in Biochemical Sciences*, 22(6):197–202.

Halberg, F. (1959). Physiologic 24-hour periodicity; general and procedural considerations with reference to the adrenal cycle. *Int Z Vitaminforsch Beih.*, 10:225–96.

Harold, F. M. (1977). Ion currents and physiological functions in microorganisms. *Ann. Rev. Microbiol.*, 31(1702):181–203.

Heinrich, K., Leslie, D. J., and Jonas, K. (2015). *Modulation of Bacterial Proliferation as a Survival Strategy*, volume 92. Elsevier Ltd.

Helaine, S. and Kugelberg, E. (2014). Bacterial persisters: Formation, eradication, and experimental systems. *Trends in Microbiology*, 22(7):417–424.

Hill, C., Cotter, P. D., Sleator, R. D., and Gahan, C. G. M. (2002). Bacterial stress response in Listeria monocytogenes: Jumping the hurdles imposed by minimal processing. *International Dairy Journal*, 12(2-3):273–283.

Hill, N. S., Kadoya, R., Chattoraj, D. K., and Levin, P. A. (2012). Cell size and the initiation of DNA replication in bacteria. *PLoS Genetics*, 8(3):14–16.

Hodgkin, A. L. and Huxley, A. F. (1952). A quantitative description of membrane current and its application to conduction and excitation in nerve. *Bulletin of mathematical biology*, 52(1-2):25–71; discussion 5–23.

Hohle, T. H. and O'Brian, M. R. (2014). Magnesium-dependent processes are targets of bacterial manganese toxicity. *Molecular Microbiology*, 93(4):736–747.

Huang, T. C. and Chow, T. J. (1990). Characterization of the rhythmic nitrogen-fixing activity of *Synechococcus* sp. RF-1 at the transcription level. *Current Microbiology*, 20(1):23–26.

Humphries, J., Xiong, L., Liu, J., Prindle, A., Yuan, F., Arjes, H. A., Tsimring, L., and Süel, G. M. (2017). Species-independent attraction to biofilms through electrical signaling. *Cell*, 168(1-2):200–209.e12.

Huygens, C. (1669). Instructions concerning the use of pendulum-watches for finding the longitude at sea. *Phil. Trans. R. Soc. Lond*, (4):937.

Ishiura, M. (1998). Expression of a gene cluster *kaiABC* as a circadian feedback process in Cyanobacteria. *Science*, 281(5382):1519–1523.

Jõers, A. and Tenson, T. (2016). Growth resumption from stationary phase reveals memory in *Escherichia coli* cultures. *Scientific Reports*, 6(March):1–11.

Johnson, C. H. (2010). Circadian clocks and cell division: What's the pacemaker? *Cell Cycle*, 9(19):3864–3873.

Kaasik, K. and Lee, C. C. (2004). Reciprocal regulation of haem biosynthesis and the circadian clock in mammals. *Nature*, 430(6998):467–471.

Kaguni, J. M. (2006). DnaA: Controlling the Initiation of Bacterial DNA Replication and More. *Annual Review of Microbiology*, 60(1):351–371.

Katayama, T., Kubota, T., Kurokawa, K., Crooke, E., and Sekimizu, K. (1998). The initiator function of DnaA protein is negatively regulated by the sliding clamp of the E. coli Chromosomal replicase. *Cell*, 94(1):61–71.

Katayama, T., Ozaki, S., Keyamura, K., and Fujimitsu, K. (2010). Regulation of the replication cycle: Conserved and diverse regulatory systems for DnaA and oriC. *Nature Reviews Microbiology*, 8(3):163–170.

Kato, J.-i. (2001). Hda, a novel DnaA-related protein, regulates the replication cycle in Escherichia coli. *The EMBO Journal*, 20(15):4253–4262.

Keller, L. and Surette, M. G. (2006). Communication in bacteria: an ecological and evolutionary perspective. *Nature Reviews Microbiology*, 4:249.

Kim, Y. I., Burton, R. E., Burton, B. M., Sauer, R. T., and Baker, T. A. (2000). Dynamics of substrate denaturation and translocation by the ClpXP degradation machine. *Molecular Cell*, 5(4):639–648.

Klein, D. J. (2004). The contribution of metal ions to the structural stability of the large ribosomal subunit. *RNA*, 10(9):1366–1379.

Klumpp, S. and Hwa, T. (2014). ScienceDirect Bacterial growth: global effects on gene expression , growth feedback and proteome partition. *Current Opinion in Biotechnology*, 28:96–102.

Klumpp, S., Scott, M., Pedersen, S., and Hwa, T. (2013). Molecular crowding limits translation and cell growth. *Proceedings of the National Academy of Sciences*, 110(42):16754–16759.

Kohanski, M. A., Dwyer, D. J., Hayete, B., Lawrence, C. A., and Collins, J. J. (2007). A common mechanism of cellular death induced by bactericidal antibiotics. *Cell*, 130(5):797–810.

Konopka, R. J. and Benzer, S. (1971). Clock mutants of *Drosophila melanogaster*. *Proceedings of the National Academy of Sciences of the United States of America*, 68(9):2112–6.

Kruse, K. and Jülicher, F. (2005). Oscillations in cell biology. *Current Opinion in Cell Biology*, 17(1):20–26.

Kuchina, A., Espinar, L., Cagatay, T., Balbin, A. O., Zhang, F., Alvarado, A., Garcia-Ojalvo, J., and Süel, G. M. (2011). Temporal competition between differentiation programs determines cell fate choice. *Molecular systems biology*, 7(557):557.

Kwon, E. J., Skalak, M., Bertucci, A., Braun, G., Ricci, F., Ruoslahti, E., Sailor, M. J., and Bhatia, S. N. (2017). Porous Silicon Nanoparticle Delivery of Tandem Peptide Anti-Infectives for the Treatment of *Pseudomonas aeruginosa* Lung Infections. *Advanced materials (Deerfield Beach, Fla.)*, 29(35):1–9.

Lago, M., Monteil, V., Douche, T., Guglielmini, J., Criscuolo, A., Maufrais, C., Matondo, M., and Norel, F. (2017). Proteome remodelling by the stress sigma factor RpoS/σ^S in *Salmonella*: Identification of small proteins and evidence for post-transcriptional regulation. *Scientific Reports*, 7(1):1–15.

Lane-claypon, J. E. (1901). Multiplication of bacteria and the influence of temparature and some other conditions. *Journal of Hygiene*, 9(2):239–248.

Lange, R. and Hengge-Aronis, R. (1991). Identification of a central regulator of stationary phase gene expression in *Escherichia coli*. *Molec. Microbiol.*, 5(1):49–59.

Larkin, J. W., Zhai, X., Kikuchi, K., Redford, S. E., Prindle, A., Liu, J., Greenfield, S., Walczak, A. M., Garcia-Ojalvo, J., Mugler, A., and Süel, G. M. (2018). Signal Percolation within a Bacterial Community. *Cell systems*, 7(2):137–145.e3.

Lee, A. J., Wang, S., Meredith, H. R., Zhuang, B., Dai, Z., and You, L. (2018). Robust, linear correlations between growth rates and β-lactam-mediated lysis rates. *Proceedings of the National Academy of Sciences*, 115(16):4069.

Leung, V. and Lévesque, C. M. (2012). A stress-inducible quorum-sensing peptide mediates the formation of persister cells with noninherited multidrug tolerance. *Journal of Bacteriology*, 194(9):2265–2274.

Levin, B. R., McCall, I. C., Perrot, V., Weiss, H., Ovesepian, A., and Baquero, F. (2017). A numbers game: Ribosome densities, bacterial growth, and antibiotic-mediated stasis and death. *mBio*, 8(1):1–13.

Levin-Reisman, I., Ronin, I., Gefen, O., Braniss, I., Shoresh, N., and Balaban, N. Q. (2017). Antibiotic tolerance facilitates the evolution of resistance. *Science (New York, N.Y.)*, 355(6327):826–830.

Lewis, K. (2007). Persister cells, dormancy and infectious disease. *Nature Reviews Microbiology*, 5(1):48–56.

Lewis, K. (2010). Persister Cells. *Annual Review of Microbiology*, 64(1):357–372.

Lewis, M., Chang, G., Horton, N. C., Kercher, M. A., Pace, H. C., Schumacher, M. A., Brennan, R. G., and Lu, P. (1996). Crystal structure of the lactose operon repressor and its complexes with DNA and inducer. *Science*, 271(5253):1247–1254.

Liu, J., Martinez-Corral, R., Prindle, A., Lee, D.-Y. D., Larkin, J., Gabalda-Sagarra, M., Garcia-Ojalvo, J., and Süel, G. M. (2017a). Coupling between distant biofilms and emergence of nutrient time-sharing. *Science*, 356(6338):638–642.

Liu, J., Prindle, A., Humphries, J., Gabalda-Sagarra, M., Asally, M., Lee, D.-y. D., Ly, S., Garcia-Ojalvo, J., and Süel, G. M. (2015). Metabolic codependence gives rise to collective oscillations within biofilms. *Nature*, 523(7562):550–4.

Liu, S., Wu, N., Zhang, S., Yuan, Y., Zhang, W., and Zhang, Y. (2017b). Variable persister gene interactions with (p)ppgpp for persister formation in *Escherichia coli*. *Frontiers in Microbiology*, 8(1795):1–14.

Lobell, R. B. and Schleif, R. F. (1990). DNA looping and unlooping by AraC protein. *Science*, 250(4980):528–532.

Løbner-Olesen, A., Skarstad, K., Hansen, F. G., von Meyenburg, K., and Boye, E. (1989). The DnaA protein determines the initiation mass of Escherichia coli K-12. *Cell*, 57(5):881–889.

Lobritz, M. A., Belenky, P., Porter, C. B. M., Gutierrez, A., Yang, J. H., Schwarz, E. G., Dwyer, D. J., Khalil, A. S., and Collins, J. J. (2015). Antibiotic efficacy is linked to bacterial cellular respiration. *Proceedings of the National Academy of Sciences*, 112(27):8173–8180.

Locke, J. C., Young, J. W., Fontes, M., Jiménez, M. J. H., and Elowitz, M. B. (2011). Stochastic pulse regulation in bacterial stress response. *Science*, 334(6054):366–369.

Lu, M., Campbell, J. L., Boye, E., and Kleckner, N. (1994). SeqA: A negative modulator of replication initiation in E. coli. *Cell*, 77(3):413–426.

Lu, W.-P., Kincaid, E., Sun, Y., and Bauer, M. D. (2001). Kinetics of β-Lactam Interactions with Penicillin-susceptible and -resistant Penicillin-binding Protein 2x Proteins from Streptococcus pneumoniae. *Journal of Biological Chemistry*, 276(34):31494–31501.

Luo, Y. and Helmann, J. D. (2012). Analysis of the role of Bacillus subtilis σM in β-lactam resistance reveals an essential role for c-di-AMP in peptidoglycan homeostasis. *Molecular Microbiology*, 83(3):623–639.

Madar, D., Dekel, E., Bren, A., Zimmer, A., Porat, Z., and Alon, U. (2013). Promoter activity dynamics in the lag phase of *Escherichia coli*. *BMC Systems Biology*, 7(1):136.

Maisonneuve, E. and Gerdes, K. (2014). Molecular mechanisms underlying bacterial persisters. *Cell*, 157(3):539–548.

Marczynski, G. T. (1999). Chromosome Methylation and Measurement of Faithful , Once and Only Once per Cell Cycle Chromosome Replication in Caulobacter crescentus Chromosome Methylation and Measurement of Faithful , Once and Only Once per Cell Cycle Chromosome Replication in Caulob. *Journal of Bacteriology*, 181(7):1984–1993.

Marczynski, G. T., Rolain, T., and Taylor, J. A. (2015). Redefining bacterial origins of replication as centralized information processors. *Frontiers in Microbiology*, 6(JUN):1–10.

Martinez-Corral, R., Liu, J., Süel, G. M., and Garcia-Ojalvo, J. (2018). Bistable emergence of oscillations in growing *Bacillus subtilis* biofilms. *Proceedings of the National Academy of Sciences of the United States of America*, 115(36):E8333–E8340.

Matsuo, T. (2003). Control Mechanism of the Circadian Clock for Timing of Cell Division in Vivo. *Science*, 302(5643):255–259.

Megaw, J. and Gilmore, B. F. (2017). Archaeal persisters: Persister cell formation as a stress response in haloferax volcanii. *Frontiers in Microbiology*, 8(AUG):1–10.

Mellor, J. (2016). The molecular basis of metabolic cycles and their relationship to circadian rhythms. *Nature Structural and Molecular Biology*, 23(12):1035–1044.

Melnikov, S., Ben-Shem, A., Garreau De Loubresse, N., Jenner, L., Yusupova, G., and Yusupov, M. (2012). One core, two shells: Bacterial and eukaryotic ribosomes. *Nature Structural and Molecular Biology*, 19(6):560–567.

Miller, C., Thomsen, L. E., Gaggero, C., Mosseri, R., Ingmer, H., and Cohen, S. N. (2004). SOS response induction by β-lactams and bacterial defense against antibiotic lethality. *Science*, 305(5690):1629.

Milo, R., Jorgensen, P., Moran, U., Weber, G., and Springer, M. (2010). BioNumbers–the database of key numbers in molecular and cell biology. *Nucleic acids research*, 38(Database issue):D750–3.

Mitsui, A., Kumazawa, S., Takahashi, A., Ikemoto, H., Cao, S., and Arai,

T. (1986). Strategy by which nitrogen-fixing unicellular cyanobacteria grow photoautotrophically. *Nature*, 323(6090):720–722.

Mohawk, J. A., Green, C. B., and Takahashi, J. S. (2012). Central and Peripheral Circadian Clocks in Mammals. *Annual Review of Neuroscience*, 35(1):445–462.

Mori, T., Binder, B., and Johnson, C. H. (1996). Circadian gating of cell division in cyanobacteria growing with average doubling times of less than 24 hours. *Proceedings of the National Academy of Sciences of the United States of America*, 93(19):10183–10188.

Moyed, H. S. and Bertrand, K. P. (1983). *hipA*, a newly recognized gene of *Escherichia coli* K-12 that affects frequency of persistence after inhibition of murein synthesis. *Journal of Bacteriology*, 155(2):768–75.

Nagoshi, E., Saini, C., Bauer, C., Laroche, T., Naef, F., and Schibler, U. (2004). Circadian gene expression in individual fibroblasts: Cell-autonomous and self-sustained oscillators pass time to daughter cells. *Cell*, 119(5):693–705.

Nakajima, M. (2005). Reconstitution of Circadian Oscillation of Cyanobacterial KaiC Phosphorylation in Vitro. *Science*, 308(5720):414–415.

Nierhaus, K. H. (2014). Mg, K and the ribosome. *Journal of Bacteriology*, 196(22):3817–3819.

Novák, B. and Tyson, J. J. (2008). Design principles of biochemical oscillators. *Nature Reviews Molecular Cell Biology*, 9(12):981–991.

Novák, R., Charpentier, E., Braun, J. S., and Tuomanen, E. (2000). Signal transduction by a death signal peptide. *Molecular Cell*, 5(1):49–57.

Ogawa, T., Yamada, Y., Kuroda, T., Kishi, T., and Moriya, S. (2002). The datA locus predominantly contributes to the initiator titration mechanism in the control of replication initiation in Escherichia coli. *Molecular Microbiology*, 44(5):1367–1375.

Paijmans, J., Bosman, M., ten Wolde, P. R., and Lubensky, D. K. (2016). Discrete gene replication events drive coupling between the cell cycle and circadian clocks. *Proceedings of the National Academy of Sciences*, 113(15):4063–4068.

Palmer, A. C. and Kishony, R. (2013). Understanding, predicting and manipulating the genotypic evolution of antibiotic resistance. *Nature Reviews Genetics*, 14:243.

Park, J., Dies, M., Lin, Y., Hormoz, S., Smith-Unna, S. E., Quinodoz, S., Hernández-Jiménez, M. J., Garcia-Ojalvo, J., Locke, J. C., and Elowitz, M. B. (2018). Molecular Time Sharing through Dynamic Pulsing in Single Cells. *Cell Systems*, 6(2):216–229.e15.

Petukh, M. and Alexov, E. (2014). Ion binding to biological macromolecules. *Asian journal of physics : an international quarterly research journal.*, 23(5):735–744.

Pikovsky, A., Rosenblum, M., Kurths, J., and Hilborn, R. C. (2002). Synchronization: A Universal Concept in Nonlinear Science. *American Journal of Physics*, 70(6):655–655.

Prasher, D. C., Eckenrode, V. K., Ward, W. W., Prendergast, F. G., and Cormier, M. J. (1992). Primary structure of the *Aequorea victoria* green-fluorescent protein. *Gene*, 111(2):229–233.

Prindle, A., Liu, J., Asally, M., Ly, S., Garcia-Ojalvo, J., and Süel, G. M. (2015). Ion channels enable electrical communication in bacterial communities. *Nature*, 527(7576):59–63.

Prindle, A., Selimkhanov, J., Li, H., Razinkov, I., Tsimring, L. S., and Hasty, J. (2014). Rapid and tunable post-translational coupling of genetic circuits. *Nature*, 508(7496):387–391.

Priyadarshini, R., Popham, D. L., and Young, K. D. (2006). Daughter cell separation by penicillin-binding proteins and peptidoglycan amidases in *Escherichia coli*. *Journal of Bacteriology*, 188(15):5345–5355.

Qin, Junjie, e. a. (2010). A human gut microbial gene catalogue established by metagenomic sequencing. *Nature*, 464(7285):59–65.

Reyes, J. and Lahav, G. (2018). Leveraging and coping with uncertainty in the response of individual cells to therapy. *Current opinion in biotechnology*, 51:109–115.

Romani, A. M. (2011). Cellular magnesium homeostasis. *Archives of Biochemistry and Biophysics*, 512(1):1–23.

Rosenblum, M., Pikovsky, A., and Kurths, J. (1996). Phase Synchronization of Chaotic Oscillators. *Physical Review Letters*, 76(11):1804–1807.

Rué, P. and Garcia-Ojalvo, J. (2011). Gene circuit designs for noisy excitable dynamics. *Mathematical Biosciences*, 231(1):90–97.

Sahar, S. and Sassone-Corsi, P. (2009). Metabolism and cancer: The circadian clock connection. *Nature Reviews Cancer*, 9(12):886–896.

Sajish, M., Tiwari, D., Rananaware, D., Nandicoori, V. K., and Prakash, B. (2007). A charge reversal differentiates (p)ppGpp synthesis by monofunctional and bifunctional Rel proteins. *Journal of Biological Chemistry*, 282(48):34977–34983.

Salter, M. G., Franklin, K. A., and Whitelam, G. C. (2003). Gating of the rapid shade-avoidance response by the circadian clock in plants. *Nature*, 426(6967):680–683.

Saper, C. B., Scammell, T. E., and Lu, J. (2005). Hypothalamic regulation of sleep and circadian rhythms. *Nature*, 437(7063):1257–1263.

Sauvage, E., Kerff, F., Terrak, M., Ayala, J. A., and Charlier, P. (2008). The penicillin-binding proteins: Structure and role in peptidoglycan biosynthesis. *FEMS Microbiology Reviews*, 32(2):234–258.

Schaechter, M., Maaloe, O., and Kjeldgaard, N. O. (1958). Dependency on Medium and Temperature of Cell Size and Chemical Composition during Balanced Growth of Salmonella typhimurium. *J. gen. Microbial.*, (19):592–606.

Schultz, D., Wolynes, P. G., Jacob, E. B., and Onuchic, J. N. (2009). Deciding fate in adverse times: Sporulation and competence in Bacillus subtilis. *Proceedings of the National Academy of Sciences*, 106(50):21027–21034.

Schuwirth, B. S. (2005). Structures of the Bacterial Ribosome at 3.5 ÅResolution. *Science*, 310(5749):827–834.

Scott, M., Gunderson, C. W., Mateescu, E. M., Zhang, Z., and Hwa, T. (2010). Interdependence of Cell Growth and Gene Expression: Origins and Consequences. *Science*, 330(6007):1099–1102.

Sharma, A., Kumar Arya, D., Dua, M., Chhatwal, G. S., and Johri, A. K. (2012). Nano-technology for targeted drug delivery to combat antibiotic resistance. *Expert opinion on drug delivery*, 9(11):1325–32.

Sharma, S., Hoskins, J. R., and Wickner, S. (2005). Binding and degradation of heterodimeric substrates by ClpAP and ClpXP. *The Journal of biological chemistry*, 280(7):5449–55.

Shimomura, O., Johnson, F. H., and Saiga, Y. (1961). Purification and properties ofCypridina luciferase. *Journal of Cellular and Comparative Physiology*, 58(2):113–123.

Skarstad, K., Boye, E., and Steen, H. B. (1986). Timing of initiation of chromosome replication in individual Escherichia coli cells. *The EMBO journal*, 5(7):1711–1717.

Skarstad, K. and Katayama, T. (2013). Regulating DNA replication in bacteria. *Cold Spring Harbor Perspectives in Biology*, 5(4):1–17.

Skarstad, K., Lueder, G., Lurz, R., Speck, C., and Messer, W. (2000). The Escherichia coli SeqA protein binds specifically and co-operatively to two sites in hemimethylated and fully methylated oriC. *Molecular Microbiology*, 36(6):1319–1326.

Slater, S., Wold, S., Lu, M., Boye, E., Skarstad, K., and Kleckner, N. (1995). E. coli SeqA protein binds oriC in two different methyl-modulated reactions appropriate to its roles in DNA replication initiation and origin sequestration. *Cell*, 82(6):927–936.

Sohmen, D., Chiba, S., Shimokawa-Chiba, N., Innis, C. A., Berninghausen, O., Beckmann, R., Ito, K., and Wilson, D. N. (2015). Structure of the *Bacillus subtilis* 70S ribosome reveals the basis for species-specific stalling. *Nature communications*, 6:6941.

Srimani, J. K., Huang, S., Lopatkin, A. J., and You, L. (2017). Drug detoxification dynamics explain the postantibiotic effect. *Molecular Systems Biology*, 13(10).

Stecchini, M. L., Del Torre, M., and Polese, P. (2013). Survival strategies of *Bacillus* spores in food. *Indian Journal of Experimental Biology*, 51(11):905–909.

Stricker, J., Cookson, S., Bennett, M. R., Mather, W. H., Tsimring, L. S., and Hasty, J. (2008). A fast, robust and tunable synthetic gene oscillator. *Nature*, 456(7221):516–519.

Süel, G. M., Garcia-Ojalvo, J., Liberman, L. M., and Elowitz, M. B. (2006). An excitable gene regulatory circuit induces transient cellular differentiation. *Nature*, 440(7083):545–550.

Süel, G. M., Kulkarni, R. P., Dworkin, J., Garcia-Ojalvo, J., and Elowitz, M. B. (2007). Tunability and noise dependence in differentiation dynamics. *Science (New York, N.Y.)*, 315(5819):1716–9.

Sweeney, B. M. and Hastings, J. W. (1958). Rhythmic Cell Division in Populations of Gonyaulax polyedra. *Eukaryotic Microbiology*, 5(3):217–224.

Tan, C., Phillip Smith, R., Srimani, J. K., Riccione, K. A., Prasada, S., Kuehn, M., and You, L. (2012). The inoculum effect and band-pass bacterial response to periodic antibiotic treatment. *Molecular Systems Biology*, 8(1).

Tanenbaum, M. E., Gilbert, L. A., Qi, L. S., Weissman, J. S., and Vale, R. D. (2014). A Protein-Tagging System for Signal Amplification in Gene Expression and Fluorescence Imaging. *Cell*, 159(3):635–646.

Tian, C., Semsey, S., and Mitarai, N. (2017). Synchronized switching of multiple toxin-antitoxin modules by (p)ppGpp fluctuation. *Nucleic acids research*, 45(14):8180–8189.

Toprak, E., Veres, A., Michel, J.-B., Chait, R., Hartl, D. L., and Kishony, R. (2011). Evolutionary paths to antibiotic resistance under dynamically sustained drug selection. *Nature Genetics*, 44:101.

Typas, A., Banzhaf, M., van den Berg van Saparoea, B., Verheul, J., Biboy, J., Nichols, R. J., Zietek, M., Beilharz, K., Kannenberg, K., Von Rechenberg, M., Breukink, E., Den Blaauwen, T., Gross, C. A., and Vollmer, W. (2010). Regulation of peptidoglycan synthesis by outer membrane proteins. *Cell*, 143(7):1097–1109.

Tyson, J. J. and Novák, B. (2008). Temporal organization of the cell cycle. *Current Biology*, 18(17):R759–R768.

Ulrik von Freiesleben, Rasmussen, K. V., and Schaechter, M. (1994). SeqA limits DnaA activity in replication from oriC in Escherichia coli. *Molecular Microbiology*, 14(4):763–772.

VandenBerg, K. E., Ahn, S., and Visick, J. E. (2016). (p)ppGpp-dependent persisters increase the fitness of *Escherichia coli* bacteria deficient in isoaspartyl protein repair. *Applied and Environmental Microbiology*, 82(17):5444–5454.

Veliz-Cuba, A., Gupta, C., Bennett, M. R., Josić, K., and Ott, W. (2016). Effects of cell cycle noise on excitable gene circuits. *Physical Biology*, 13(6).

von Freiesleben, U. (2000). The eclipse period of Escherichia coli. *The EMBO Journal*, 19(22):6240–6248.

Vulin, C., Leimer, N., Huemer, M., Ackermann, M., and Zinkernagel, A. S. (2018). Prolonged lag time results in small colony variants and reflects a sub-population of persisters in vivo. *bioRxiv*.

Wakamoto, Y., Dhar, N., Chait, R., Schneider, K., Signorino-Gelo, F., Leibler, S. S., and McKinney, J. D. (2013). Dynamic Persistence of Antibiotic-Stresssed Mycobacteria. *Science*, 339(January):91–96.

Wakeman, C. A., Goodson, J. R., Zacharia, V. M., and Winkler, W. C. (2014). Assessment of the requirements for magnesium transporters in *Bacillus subtilis*. *Journal of bacteriology*, 196(6):1206–14.

Waldminghaus, T. and Skarstad, K. (2009). Plasmid The *Escherichia coli* SeqA protein. *Plasmid*, 61(3):141–150.

Walker, N., Nghe, P., and Tans, S. J. (2016). Generation and filtering of gene expression noise by the bacterial cell cycle. *BMC Biology*, 14(1):1–10.

Wang, J. D. and Levin, P. A. (2009). Metabolism, cell growth and the bacterial cell cycle. *Nature Reviews Microbiology*, 7(11):822–827.

Weiss, R. L., Kimes, B. W., and Morris, D. R. (1973). Cations and Ribosome Structure. III. Effects on the 30s and 50s Subunits of Replacing Bound Mg2+ by Inorganic Cations. *Biochemistry*, 12(3):450–456.

West, S. A., Diggle, S. P., Buckling, A., Gardner, A., and Griffin, A. S. (2007). The social lives of microbes. *Annual Review of Ecology, Evolution, and Systematics*, 38(1):53–77.

Wold, S., Skarstad, K., Steen, H. B., Stokke, T., and Boye, E. (1994). The initiation mass for DNA replication in Escherichia coli K-12 is dependent on growth rate. *The EMBO journal*, 13(9):2097–2102.

Wood, T. K., Knabel, S. J., and Kwan, B. W. (2013). Bacterial Persister Cell Formation and Dormancy. *Applied and Environmental Microbiology*, 79(23):7116–7121.

Xiao, J. and Goley, E. D. (2016). Redefining the roles of the FtsZ-ring in bacterial cytokinesis. *Current Opinion in Microbiology*, 34:90–96.

Yang, Q., Pando, B. F., Dong, G., Golden, S. S., and van Oudenaarden, A. (2010). Circadian Gating of the Cell Cycle Revealed in Single Cyanobacterial Cells. *Science*, 327(5972):1522–1526.

Yoshikawa, H., O'Sullivan, A., and Sueoka, N. (1964). Sequential replication of the bacillus subtilis chromosome. 3. regulation of initiation. *Proceedings of the National Academy of Sciences of the United States of America*, 52(4):973–80.

Young, R. and Dennis, P. (1975). Balanced Production of 30S and 50S Ribosomal Proteins After a Nutritional Shift-Up. *Journal of Bacteriology*, 124(3):1618–1620.

Yurtsev, E. A., Conwill, A., and Gore, J. (2016). Oscillatory dynamics in a bacterial cross-protection mutualism. *Proceedings of the National Academy of Sciences*, 113(22):6236.

Zapun, A., Contreras-Martel, C., and Vernet, T. (2008). Penicillin-binding proteins and β-lactam resistance. *FEMS Microbiology Reviews*, 32(2):361–385.

Zhang, Y., Zborníková, E., Rejman, D., and Gerdes, K. (2018). Novel (p)ppGpp Binding and Metabolizing Proteins of Escherichia coli. *mBio*, 9(2):e02188–17.